



TECHNISCHE
UNIVERSITÄT
DARMSTADT

Physik

Spectral Functions and Transport Coefficients from the Functional Renormalization Group

Vom Fachbereich Physik
der Technischen Universität Darmstadt

zur Erlangung des Grades
eines Doktors der Naturwissenschaften (Dr. rer. nat.)

genehmigte Dissertation von
Mag. rer. nat. Ralf-Arno Tripolt
aus Graz

Darmstadt 2015
D17

Referent: Priv. Doz. Dr. Lorenz von Smekal
Koreferent: Prof. Dr. Jochen Wambach

Tag der Einreichung: 10.04.2015
Tag der Prüfung: 03.06.2015

Abstract

In this thesis we present a new method to obtain real-time quantities like spectral functions and transport coefficients at finite temperature and density using the Functional Renormalization Group approach. Our non-perturbative method is thermodynamically consistent, symmetry preserving and based on an analytic continuation from imaginary to real time on the level of the flow equations. We demonstrate the applicability of this method by calculating mesonic spectral functions as well as the shear viscosity for the quark-meson model.

In particular, results are presented for the pion and sigma spectral function at finite temperature and chemical potential, with a focus on the regime near the critical endpoint in the phase diagram of the quark-meson model. Moreover, the different time-like and space-like processes, which give rise to a complex structure of the spectral functions, are discussed. Finally, based on the momentum dependence of the spectral functions, we calculate the shear viscosity and the shear viscosity to entropy density ratio using the corresponding Green-Kubo formula.

Zusammenfassung

In dieser Arbeit präsentieren wir eine neue Methode, um Realzeit-Größen wie Spektralfunktionen und Transportkoeffizienten bei endlicher Temperatur und Dichte mit Hilfe der Funktionalen Renormierungsgruppe zu berechnen. Unsere nicht-störungstheoretische Methode ist thermodynamisch konsistent, symmetrieerhaltend und basiert auf einer analytischen Fortsetzung von imaginärer Zeit zu reeller Zeit auf der Ebene der Flussgleichungen. Wir demonstrieren die Anwendbarkeit dieser Methode, indem wir die mesonischen Spektralfunktionen sowie die Scherviskosität für das Quark-Meson-Modell berechnen.

Insbesondere werden Ergebnisse für die Pion- und Sigma-Spektralfunktion bei endlicher Temperatur und chemischem Potential präsentiert, wobei der Fokus auf dem Gebiet um den kritischen Endpunkt im Phasendiagramm des Quark-Meson-Modells liegt. Außerdem werden die verschiedenen zeitartigen und raumartigen Prozesse diskutiert, welche eine komplizierte Struktur der Spektralfunktionen bewirken. Schlussendlich berechnen wir, basierend auf der Impulsabhängigkeit der Spektralfunktionen, die Scherviskosität sowie das Verhältnis der Scherviskosität zur Entropiedichte mit Hilfe der entsprechenden Green-Kubo-Formel.

Contents

1. Introduction	1
I. Theoretical Setup	7
2. The quark-meson model as an effective model for QCD	9
2.1. Aspects of Quantum Chromodynamics	9
2.2. Chiral symmetry	10
2.3. Quark-meson model	13
3. Flow equations for the quark-meson model	17
3.1. Basic ideas of the Functional Renormalization Group	17
3.2. Flow equation for the effective potential of the QM model and thermodynamic observables	20
3.3. Flow equations for the mesonic two-point functions of the QM model and thermodynamic consistency	22
4. Analytic continuation and spectral functions	25
4.1. Basic idea of analytic continuation	25
4.2. Simple one-loop example	26
4.3. Analytic continuation of flow equations	28
4.4. Definition and analytic properties of spectral functions	29
4.5. Interpretation of spectral functions	33
5. Relativistic hydrodynamics and Green-Kubo formula for the shear viscosity	35
5.1. Ideal relativistic hydrodynamics	35
5.2. Viscous relativistic hydrodynamics and the shear viscosity	37
5.3. Green-Kubo relations for transport coefficients	38
5.4. Application of the Green-Kubo formula for the shear viscosity to the quark-meson model	40
6. Numerical implementation	47
6.1. Solving the flow equation for the effective potential	47
6.2. Solving the flow equations for the two-point functions and MPI parallelization	49
6.3. Calculating the shear viscosity	51

II. Results	53
7. Phase diagram and thermodynamics	55
7.1. The phase diagram of the quark-meson model	55
7.2. Quasi-particle masses and entropy density	56
8. Decay channels and two-point functions	59
8.1. Available decay channels and quasi-particle processes	59
8.2. Real and imaginary part of retarded two-point functions	62
9. Spectral functions	65
9.1. Spectral functions at finite temperature and chemical potential	65
9.2. Momentum dependence of spectral functions	69
10. Shear viscosity	73
10.1. Shear viscosity and shear viscosity to entropy density ratio at finite temperature	73
10.2. Shear viscosity near the critical endpoint	79
11. Summary and Outlook	81
A. Notation and Conventions	83
A.1. Natural units and notation	83
A.2. Euclidean space-time	84
A.3. Fourier transform and functional calculus	84
B. Derivation of Flow Equations	87
B.1. Flow equation for the effective action	87
B.2. Flow equation for the effective potential of the quark-meson model	91
C. Threshold Functions	97
D. Derivation of the Green-Kubo Formula for the Shear Viscosity	103
E. Lorentz invariance and parameter dependence of spectral functions	109
E.1. Lorentz invariance	109
E.2. Dependence on the epsilon parameter	110
E.3. Dependence on the UV cutoff and normalization	112
F. 3D plots of the momentum dependence of spectral functions	115
F.1. 3D plots of the pion spectral function at finite T	116
F.2. 3D plots of the sigma spectral function at finite T	118
F.3. 3D plots of the pion spectral function near the CEP	120
F.4. 3D plots of the sigma spectral function near the CEP	121
Bibliography	123

1

Introduction

Approximately fourteen billion years ago [1], only a few microseconds after the Big Bang, the universe was in an extremely hot and dense state. It was filled with elementary particles like quarks and gluons at temperatures of more than several trillion (10^{12}) Kelvin, which is at least 100,000 times hotter than the center of our sun. As the universe expanded, this quark-gluon plasma cooled down until hadrons, including baryons such as protons and neutrons, could form at a temperature of approximately $1.75 \cdot 10^{12}$ K, which corresponds to 150 MeV [2, 3].

The evolution of the early universe can also be represented in terms of the phase diagram of strongly interacting matter, also known as the phase diagram of Quantum Chromodynamics (QCD), cf. Fig. 1.1. Within this phase diagram, which is still largely uncharted, some of the expected equilibrium phases of quarks and gluons are represented in the temperature and net-baryon density plane. We note that the course of the early universe appears at relatively small net-baryon densities, referring to the fact that there was only a small excess of quarks over antiquarks, which resulted in the dominance of matter over antimatter in the present universe.

Apart from the crossover transition from a quark-gluon plasma to a hadron gas, the QCD phase diagram exhibits several other interesting features. For instance, at low temperatures and nuclear density we have ordinary atomic matter, which exists at the phase boundary between vacuum and nuclear matter. The corresponding first-order phase transition line ends in a critical point at a temperature of approximately 15 MeV, as set by the scale of nuclear binding energies. When increasing the net-baryon density further, while keeping the temperature low, we encounter another first-order phase transition towards a phase of extremely compressed quark matter, as for example expected to be present inside neutron stars. At even higher densities one expects more exotic states of quark matter such as the color-flavor-locked (CFL) phase [4]. Another prominent feature of the QCD phase diagram is the critical endpoint that connects the first-order

1. Introduction

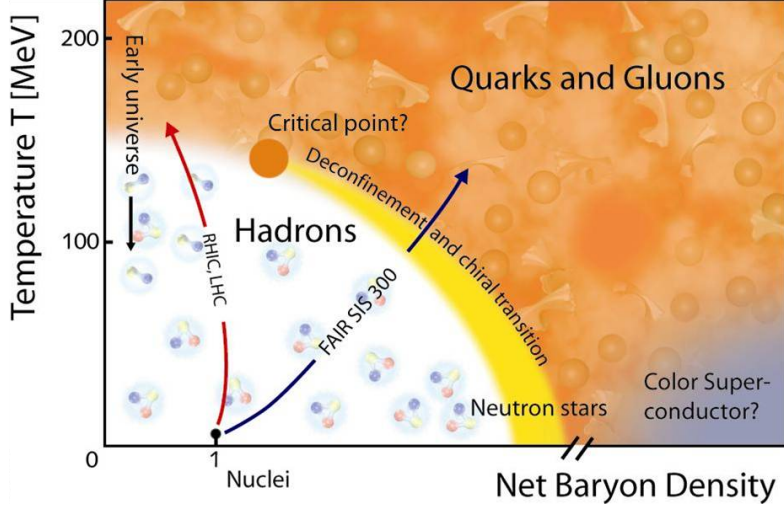


Figure 1.1.: The QCD phase diagram is shown in the plane of temperature and net baryon density. Taken from [5].

line between the nuclear and the quark-matter phases with the crossover regime between the quark-gluon plasma and the hadronic phase. This critical endpoint represents a second-order phase transition, the most common critical phenomenon in condensed matter physics. For example, there is also a critical point in the phase diagram of water, connecting the liquid and vapor phase. Such a critical point is of particular interest to experimental as well as theoretical studies due to the unique physical phenomena it entails, like a diverging correlation length or critical opalescence.

The recreation and investigation of the quark-gluon plasma, mapping out the QCD phase diagram with a particular focus on locating the critical endpoint, and studying the properties of strongly interacting matter are central aims of modern-day laboratory experiments. Such experiments are for example carried out at the Relativistic Heavy Ion Collider (RHIC) at Brookhaven National Laboratory (BNL) and the Large Hadron Collider (LHC) at the European Organization for Nuclear Research (CERN) where protons and/or heavy ions are collided at relativistic energies. In the near future, such experiments will also be performed at the Facility for Antiproton and Ion Research (FAIR) at lower beam energies with the particular aim to study the regime of high baryon densities. The approximate temperature and net-baryon density range covered by these experiments is also indicated in Fig. 1.1.

When investigating transport properties like the shear viscosity of the produced matter, one finds that the quark-gluon plasma resembles an ideal liquid, which corresponds to a strongly interacting system. In fact, the shear viscosity to entropy density ratio, η/s , of the quark-gluon plasma turns out to be smaller than that of any other known substance, with the possible exception of ultra-cold quantum gases [6, 7]. Moreover, it is very close to the smallest possible value of η/s for plasmas described by infinitely strongly interacting gauge theories that have a dual gravitational description [8].

1. Introduction

Providing a new way to calculate real-time quantities like spectral functions and transport coefficients like the shear viscosity is the central aim of this thesis. In general, studying dynamical properties of strongly interacting matter represents a very challenging endeavor, experimentally as well as theoretically. From a theoretical point of view, one would ideally like to perform first-principles QCD calculations at all temperatures and densities. The two corresponding methods, lattice QCD and perturbation theory have their limitations though. Perturbation theory, for example, relies on an expansion in terms of the QCD coupling, which is only small at large temperatures and/or densities. Lattice QCD, on the other hand, is a non-perturbative method based on a discretization of Euclidean space-time on a four-dimensional grid in a finite volume. It is, however, hampered by the sign-problem at finite chemical potentials [9]. Moreover, since it is formulated in Euclidean space-time, which entails an imaginary time variable, the calculation of real-time quantities like transport coefficients or spectral functions is very difficult due to the so-called analytic continuation problem.

This technical difficulty of extending the domain of some quantity from imaginary to real time is common to all Euclidean approaches to quantum field theory. Performing such an analytic continuation is particularly intricate at finite temperature where these continuations are based on information at discrete Matsubara frequencies and hence require additional boundary conditions for uniqueness [10, 11]. Even with the analytic structure completely fixed, the reconstruction of real-time quantities like spectral functions and transport coefficients based on discrete numerical, i.e. noisy, data is an ill-posed inverse problem. Maximum entropy methods (MEM) [12, 13], Padé approximants [14], or very recently also a standard Tikhonov regularization [15] have been proposed to deal with this problem. They all work best at low temperatures when the density of Matsubara modes is sufficiently large, but they all break down when the Euclidean input data is not sufficiently dense and precise. Therefore, any approach that can deal with the analytic continuation problem without running into these difficulties is highly desirable.

Such alternative methods were proposed, for example, in [16, 17] and [18] for the Functional Renormalization Group (FRG). The FRG represents a powerful continuum framework for non-perturbative calculations particularly in quantum field theory and statistical physics, see [19, 20, 21, 22, 23, 24] for reviews. In addition to providing a complementary approach to, e.g., lattice QCD or Dyson-Schwinger Equations (DSEs), the FRG allows for a proper inclusion of quantum fluctuations which makes this framework particularly well suited to describe critical phenomena like phase transitions. Moreover, the FRG also allows to perform calculations at finite chemical potentials without any further complications. Due to these advantages we will use the FRG framework in this thesis in order to develop a new way to deal with the analytic continuation problem.

In principle, the FRG framework can be applied to QCD itself, which is, however, extremely difficult. In practise, one therefore often uses effective models to gain qualitative or even some quantitative insights into the properties of strongly interacting matter. One such model, which we will also use in this thesis, is the two-flavor quark-meson model [25, 26]. It acts as an effective model for QCD at low-energies and includes the two lightest quark flavors as well as the three pions and the sigma meson as fundamental degrees of freedom. Moreover, it incorporates chiral symmetry and its breaking pattern

1. Introduction

and is therefore well suited to study the chiral phase structure of QCD in a qualitative manner at intermediate temperatures and densities. At high temperatures beyond the crossover transition, however, gluons become, along with quarks, the relevant degrees of freedom and the applicability of the quark-meson model breaks down. Gluonic degrees of freedom, as well as aspects of confinement, can, for example, be effectively taken into account by means of the Polyakov quark-meson model [27, 28]. Similarly, at high chemical potentials and low temperatures, baryonic degrees of freedom become important, which are also not included in the quark-meson model. In spite of these limitations, we believe that the quark-meson model serves as an excellent testing ground for developing our new analytic continuation method and to demonstrate its applicability.

In this thesis, we will employ the two-flavor quark-meson model within an FRG study in order to present a new method to obtain real-time quantities like spectral functions and transport coefficients at finite temperature and chemical potential. Our method is based on an analytic continuation from imaginary to real time on the level of the flow equations and enjoys a number of advantages. These include, for example, that it is symmetry preserving, i.e. chiral symmetry and its breaking pattern are realized exactly. Moreover, it is thermodynamically consistent in that the space-like limit of zero external momentum in the two-point functions agrees with the curvature masses as extracted from the effective potential [17, 29]. Furthermore, our method satisfies the physical Baym-Mermin boundary conditions [10] which are implemented essentially as in a simple one-loop calculation [30, 31]. In addition, it can be systematically improved towards full QCD [27, 28] and to calculate quark and gluonic spectral functions as an alternative to analytically continued DSEs [32] or to using MEM on Euclidean FRG [33] or DSE results [34, 35, 36].

In order to demonstrate the applicability and usefulness of our method, we will calculate the mesonic spectral functions of the quark-meson model, in particular near the critical endpoint in the corresponding phase diagram. Moreover, results on the spatial-momentum dependence of the spectral functions will be presented and interpreted in terms of the different time-like and space-like quasi-particle processes that can occur within our framework. Based on the momentum-dependence of the spectral functions, we will also calculate the shear viscosity and the shear viscosity to entropy density ratio, η/s , by means of the corresponding Green-Kubo formula.

This thesis is organized as follows. In Part I we will present our theoretical setup, beginning with a discussion of some basic aspects of QCD and by constructing the Lagrangian of the quark-meson model based on chiral symmetry considerations in Chapter 2. In Chapter 3, we will introduce the Functional Renormalization Group and derive flow equations for the effective potential as well as for the mesonic two-point functions of the quark-meson model. These flow equations are analytically continued to real energies in Chapter 4, where we also discuss basic properties of spectral functions. In Chapter 5, we discuss some basic aspects of ideal and viscous relativistic hydrodynamics in order to introduce the shear viscosity. Moreover, the Green-Kubo formula for the shear viscosity is discussed and applied to the quark-meson model. Details on our numerical implementation are presented in Chapter 6. In Part II, we present our results, beginning with a discussion of the phase diagram of the quark-meson model and some

1. Introduction

thermodynamic quantities in Chapter 7. The different time-like and space-like quasi-particle processes that can occur within our framework are discussed in Chapter 8 where we also present results on the retarded two-point functions. In Chapter 9 we present results on the pion and sigma spectral function at finite temperature and chemical potential as well as on their momentum dependence. Results on the shear viscosity and the shear viscosity to entropy density ratio are presented in Chapter 10. A summary and an outlook are given in Chapter 11. Appendix A summarizes details on the notation and the conventions used in this thesis. A derivation of the Wetterich equation and of the corresponding flow equation for the effective potential of the quark-meson model is provided in Appendix B. In Appendix C, we list explicit expressions for our threshold and loop functions. A derivation of the Green-Kubo formula for the shear viscosity is provided in Appendix D. A possible violation of Lorentz invariance, the parameter dependence of our results and the normalization of the spectral functions are discussed in Appendix E. Finally, in Appendix F, we provide three-dimensional plots to show the momentum dependence of spectral function at various temperatures and chemical potentials.

We conclude this introduction by listing the peer-reviewed publications that have been produced so far in the context of this thesis:

- Ralf-Arno Tripolt, Lorenz von Smekal, Jochen Wambach,
“Flow equations for spectral functions at finite external momenta”,
Phys. Rev. **D 90**, 074031 (2014), arXiv:1408.3512.
- Ralf-Arno Tripolt, Nils Strodthoff, Lorenz von Smekal, Jochen Wambach,
“Spectral Functions from the Functional Renormalization Group at finite temperature and density”,
Nucl. Phys. **A 931**, November 2014, 790-795, arXiv:1407.8387,
Talk presented at Quark Matter 2014 by the author of this thesis.
- Jochen Wambach, Ralf-Arno Tripolt, Nils Strodthoff, Lorenz von Smekal,
“Spectral Functions from the Functional Renormalization Group”,
Nucl. Phys. **A 928**, August 2014, 156-167, arXiv:1404.7312,
Talk presented at “45 years of nuclear theory at Stony Brook - A tribute to Gerald E. Brown” by J. Wambach.
- Ralf-Arno Tripolt, Nils Strodthoff, Lorenz von Smekal, Jochen Wambach,
“Spectral Functions for the Quark-Meson Model Phase Diagram from the Functional Renormalization Group”,
Phys. Rev. **D 89**, 034010 (2014), arXiv:1311.0630.
- Ralf-Arno Tripolt, Nils Strodthoff, Lorenz von Smekal, and Jochen Wambach,
“Finite-Temperature Spectral Functions from the Functional Renormalization Group”,
PoS (LATTICE 2013) 457, arXiv:1311.4304.

Part I.

Theoretical Setup

2

The quark-meson model as an effective model for QCD

In this chapter, we will first discuss some basic aspects of Quantum Chromodynamics in Sec. 2.1 and then focus on chiral symmetry in Sec. 2.2. Along the lines of chiral symmetry and its breaking pattern, the Lagrangian of the quark-meson model will be constructed in Sec. 2.3 which will act as a basis for the subsequent renormalization group study.

2.1 Aspects of Quantum Chromodynamics

Quantum Chromodynamics (QCD) is the commonly accepted theory of the strong interaction. It represents a non-Abelian gauge theory with the fundamental degrees of freedom being quarks and gluons. The observed particles, the hadrons, are then described as particle excitations of this quantum field theory. The most stable and familiar examples of hadrons are protons and neutrons, which are both composed of three (valence) quarks. Such composite particles made up of three quarks are called baryons, while bound states formed by one quark and one antiquark are called mesons.

There are six types or “flavors” of quarks, which are, in the order of increasing mass, labelled up (u), down (d), strange (s), charm (c), bottom (b) and top (t). The up and down quarks have a mass of approximately 3 – 5 MeV, while the strange quark already has a mass of around 100 MeV. Quarks are fermions and carry fractional charges of either $2/3$ or $-1/3$ times the elementary charge. In addition to an electric charge, quarks also carry a so-called “color charge”, which represents a three-valued degree of freedom and is, in analogy to the three primary colors of light, usually labelled red, green and blue. Free particles are then required to have a color charge of zero, which can be realized by either combining all three colors, as in baryons, or by compensating a color by its anti-color, as in the case of mesons.

2. The quark-meson model as an effective model for QCD

This notion of an additional quark degree of freedom, first proposed by O. W. Greenberg in 1964 [37] in order to explain how quarks could coexist inside some hadrons in otherwise identical quantum states, gives rise to the formulation of QCD as a gauge theory with gauge group $SU(N_c)$, where $N_c = 3$ is the number of colors. The requirement of local gauge invariance then leads to the introduction of vector boson fields, the gluons, which mediate the strong interaction. In contrast to Quantum Electrodynamics (QED), where the interaction particle, i.e. the photon, does not carry a charge, the gluons do carry color charge. Since a gluon cannot exist in a color singlet state, there are $N_c^2 - 1 = 8$ gluons which form a color octet.

So far, however, no color-charged particle has been observed in an isolated state. This phenomenon, that all color-charged particles seem to be confined within hadrons, is referred to as color confinement, or simply confinement. Confinement can, for example, be demonstrated by lattice QCD calculations, where one can show that the gluon field forms a flux tube or “string” between a static quark-antiquark pair, cf. [38, 39]. This flux tube exerts a strong attractive force on the quark-antiquark pair which is, for large separations, independent of the distance between the two particles. Eventually, when the quark-antiquark pair is separated far enough, it is energetically favorable to produce new particles using the energy stored in the flux tube. This process is called string breaking or hadronization and leads to the fact that only color-neutral particles are observed. However, the phenomenon of confinement is analytically unproven and far from being completely understood.

Another important feature of QCD is asymptotic freedom, which states that the interaction strength between color-charged particles becomes arbitrarily weak at high energies. This effect was described and published in 1973 by D. Gross and F. Wilczek [40, 41], and independently by D. Politzer [42], who shared the Nobel Prize in 2004. The dependence of the interaction strength on the energy or length scale can be understood as follows. In QED, for example, the vacuum in the vicinity of a charge becomes polarized, i.e. virtual electron-positron pairs will be oriented such that the central charge will effectively decrease with larger distances. In QCD, however, there is not only a screening effect by virtual quark-antiquark pairs but also an anti-screening effect created by virtual gluons. It turns out that, in the case of three colors and six flavors, the anti-screening effect is stronger than the screening effect and hence, the strong interaction becomes weaker at higher energies, see for example [43].

2.2 Chiral symmetry

We now turn to a brief discussion of chiral symmetry, which is a global symmetry of the QCD Lagrangian in the limit of vanishing current quark masses. The gauge invariant QCD Lagrangian is given by

$$\mathcal{L}_{\text{QCD}} = \sum_f \bar{\psi}_{i,f} (i\gamma^\mu D_\mu^{ij} - m_f \delta^{ij}) \psi_{j,f} - \frac{1}{4} F_{\mu\nu}^a F_a^{\mu\nu}, \quad (2.1)$$

2. The quark-meson model as an effective model for QCD

where the covariant derivative is defined as

$$D_\mu^{ij} = \partial_\mu \delta^{ij} - ig t_a^{ij} A_\mu^a, \quad (2.2)$$

and the gluon field strength tensor is given by

$$F_{\mu\nu}^a = \partial_\mu A_\nu^a - \partial_\nu A_\mu^a + gf^{abc} A_\mu^b A_\nu^c. \quad (2.3)$$

The quark and antiquark fields, $\psi_{j,f}$ and $\bar{\psi}_{i,f}$, lie in the fundamental representation of the SU(3) gauge group, with the color and flavor indices given by $i, j \in 1, \dots, N_c$ and $f \in 1, \dots, N_f$. The gluon fields, A_μ^a , are in the adjoint representation of SU(3) with the color index $a \in 1, \dots, 8$. The current masses of the different quark flavors are given by m_f , the quark-gluon coupling is denoted as g and t_a^{ij} are the generators of the SU(3) gauge group with the structure constants f^{abc} , where $a, b, c \in 1, \dots, 8$.

In the limit of vanishing current quark masses, i.e. the ‘‘chiral limit’’, the QCD Lagrangian for the two lightest quark fields can be written as

$$\mathcal{L}_0 = \bar{u}_L i \gamma^\mu D_\mu u_L + \bar{u}_R i \gamma^\mu D_\mu u_R + \bar{d}_L i \gamma^\mu D_\mu d_L + \bar{d}_R i \gamma^\mu D_\mu d_R - \frac{1}{4} F_{\mu\nu}^a A_a^{\mu\nu}, \quad (2.4)$$

where we expressed the quark fields in terms of their left- and right-handed components, which are defined as

$$\psi_{R,L} = \frac{1}{2}(1 \pm \gamma_5)\psi, \quad (2.5)$$

with $\gamma_5 = i\gamma_0\gamma_1\gamma_2\gamma_3$. Since there is basically no difference between the quark fields of different flavors, they can be mixed, independently for the left- and right-handed sector, without changing the physics. This gives rise to an invariance of the QCD Lagrangian for massless quarks, cf. Eq. (2.4), under the chiral group

$$U_L(N_f) \otimes U_R(N_f) = U_V(1) \otimes SU_V(N_f) \otimes SU_A(N_f) \otimes U_A(1), \quad (2.6)$$

where the indices V and A refer to ‘‘vector’’ and ‘‘axial-vector’’ transformations. The $U_V(1)$ symmetry is also realized in full QCD and gives rise to the conservation of baryon number, while the $U_A(1)$ symmetry, although present in the QCD Lagrangian, is destroyed by quantization. This is referred to as the axial anomaly and relates to the large mass of the η' meson, cf. for example [44, 23].

We now turn to transformations with respect to the groups $SU_V(N_f)$ and $SU_A(N_f)$, where we specialize to $N_f = 2$ and use the iso-spinor notation $\psi = (u, d)$. For massless quarks, the Lagrangian (2.4) is then invariant under vector transformations

$$\Lambda_V : \quad \begin{aligned} \psi &\rightarrow \exp(-i\vec{\tau}\vec{\theta}/2)\psi \simeq (1 - i\vec{\tau}\vec{\theta}/2)\psi, \\ \bar{\psi} &\rightarrow \exp(+i\vec{\tau}\vec{\theta}/2)\bar{\psi} \simeq (1 + i\vec{\tau}\vec{\theta}/2)\bar{\psi}, \end{aligned} \quad (2.7)$$

2. The quark-meson model as an effective model for QCD

as well as under axial transformations

$$\Lambda_A : \begin{aligned} \psi &\rightarrow \exp(-i\gamma_5 \vec{\tau} \vec{\theta}/2) \psi \simeq (1 - i\gamma_5 \vec{\tau} \vec{\theta}/2) \psi, \\ \bar{\psi} &\rightarrow \exp(-i\gamma_5 \vec{\tau} \vec{\theta}/2) \bar{\psi} \simeq (1 - i\gamma_5 \vec{\tau} \vec{\theta}/2) \bar{\psi}, \end{aligned} \quad (2.8)$$

where $\vec{\tau}$ is a vector composed of the three Pauli matrices and $\vec{\theta}$ is a small transformation angle. The associated conserved currents are given by

$$V_\mu^a = \bar{\psi} \gamma_\mu \frac{\tau^a}{2} \psi, \quad (2.9)$$

and

$$A_\mu^a = \bar{\psi} \gamma_\mu \gamma_5 \frac{\tau^a}{2} \psi. \quad (2.10)$$

In QCD, the $SU_V(2)$ symmetry is very well realized due to the smallness of the mass difference between the up and down quark, giving rise to the conservation of isospin current in strong interactions. The axial symmetry, $SU_A(2)$, on the other hand, is broken explicitly by the non-vanishing quark masses,

$$\Lambda_A : \quad m\bar{\psi}\psi \rightarrow m\bar{\psi}\psi - im\vec{\theta}\bar{\psi}\vec{\tau}\gamma_5\psi. \quad (2.11)$$

However, since the masses of the up and down quarks are small compared to the QCD energy scale $\Lambda_{\text{QCD}} \simeq 200$ MeV, the axial symmetry may still be considered as an approximate symmetry. This notion is substantiated by the partial conservation of the axial current (PCAC) and the success of the Goldberger-Treiman relation, as discussed in the following. On the other hand, there is evidence that suggests that the axial symmetry is more than only slightly broken. The hadron spectrum, for example, should contain parity partners with small mass splitting. Such parity partners, however, do not seem to exist. The solution to this apparent inconsistency is that the $SU_A(2)$ symmetry is not only explicitly broken but also spontaneously broken by the dynamical formation of a quark condensate. Lattice simulations with dynamical up, down and strange quarks [45] show this quark or chiral condensate to be

$$\frac{1}{2} \langle 0 | \bar{u}u + \bar{d}d | 0 \rangle \simeq -(234(04)(17) \text{ MeV})^3. \quad (2.12)$$

According to the Goldstone theorem, the spontaneous breakdown of a continuous symmetry gives rise to massless excitations, the Nambu-Goldstone bosons. In the case of chiral symmetry, these Nambu-Goldstone bosons are identified to be the pions, which, however, acquire a finite mass due to the explicit breaking of chiral symmetry and are therefore referred to as “pseudo”-Nambu-Goldstone bosons.

We conclude this section by summarizing some important relations connected to chiral symmetry. First, we consider the weak decay of the pion, where the matrix element of the axial current is given by

$$\langle 0 | A_\mu^a(x) | \pi^b(q) \rangle = -if_\pi q_\mu \delta^{ab} e^{-iqx}, \quad (2.13)$$

2. The quark-meson model as an effective model for QCD

with q_μ the pion momentum, $f_\pi = 93$ MeV the pion decay constant, and a, b isospin indices. Taking the divergence of Eq. (2.13) gives

$$\langle 0 | \partial^\mu A_\mu^a(x) | \pi^b(q) \rangle = -f_\pi q^2 \delta^{ab} e^{-iqx} = -f_\pi m_\pi^2 \delta^{ab} e^{-iqx}, \quad (2.14)$$

which is often referred to as the PCAC relation. If chiral symmetry were realized exactly, one would therefore expect a vanishing pion mass.

Another useful equation is given by the Goldberger-Treiman relation. It can be obtained by applying the PCAC relation to the axial current of a nucleon and reads

$$g_{\pi NN} = \frac{g_a m_N}{f_\pi}, \quad (2.15)$$

where m_N is the nucleon mass, g_a is the axial coupling and $g_{\pi NN}$ is the strong-interaction pion-nucleon coupling, cf. [46, 47] for a derivation and a discussion of this result.

Finally, we state the Gell-Mann–Oakes–Renner (GOR) relation [48], which is given by

$$m_\pi^2 f_\pi^2 = -\frac{m_u + m_d}{2} \langle 0 | \bar{u}u + \bar{d}d | 0 \rangle, \quad (2.16)$$

and connects the pion mass and the pion decay constant with the current quark masses and the quark condensate.

The above relations will be used in the following to aid in the construction of the quark-meson Lagrangian and to validate the result obtained from this model for the quark condensate.

2.3 Quark-meson model

We will now use the considerations concerning QCD and chiral symmetry presented in the last section as a guideline to derive the Lagrangian of the quark-meson (QM) model, see also [47, 49]. The quark-meson model represents a low-energy effective model of QCD and incorporates in particular the chiral aspects of strongly interacting matter. For two flavors, the elementary degrees of freedom are given by the two lightest quarks, i.e. the up and down quark, as well as the three pions and the sigma meson. The QM model has been successfully applied in the past, see for example [25, 26], and will be subjected to a FRG study in the following.

In order to construct a Lorentz invariant Lagrangian that respects chiral symmetry, we will first study the transformation properties of the following combinations of quark fields, which carry the quantum numbers of the sigma meson and of the pions,

$$\begin{aligned} \sigma &\equiv \bar{\psi}\psi, \\ \vec{\pi} &\equiv i\bar{\psi}\vec{\tau}\gamma_5\psi. \end{aligned} \quad (2.17)$$

The sigma-like state is therefore invariant under vector transformations Λ_V , as defined

2. The quark-meson model as an effective model for QCD

by Eq. (2.7),

$$\Lambda_V : \quad \sigma \rightarrow \sigma, \quad (2.18)$$

while the pion-like state transforms as an iso-vector,

$$\begin{aligned} \Lambda_V : \quad i\bar{\psi}\tau_i\gamma_5\psi &\rightarrow i\bar{\psi}\tau_i\gamma_5\psi + \theta_j \left(\bar{\psi}\tau_i\gamma_5\frac{\tau_j}{2}\psi - \bar{\psi}\frac{\tau_j}{2}\tau_i\gamma_5\psi \right) \\ &= i\bar{\psi}\tau_i\gamma_5\psi + i\theta_j\epsilon_{ijk}\bar{\psi}\gamma_5\tau_k\psi, \end{aligned} \quad (2.19)$$

where we used $[\tau_i, \tau_j] = 2i\epsilon_{ijk}\tau_k$. This corresponds to a rotation in isospin space of the form

$$\Lambda_V : \quad \vec{\pi} \rightarrow \vec{\pi} + \vec{\theta} \times \vec{\pi}. \quad (2.20)$$

Similarly, one finds that the sigma and pion states are rotated into each other under axial transformations Λ_A , cf. Eq. (2.8),

$$\begin{aligned} \Lambda_A : \quad \sigma &\rightarrow \sigma - \vec{\theta}\vec{\pi}, \\ \vec{\pi} &\rightarrow \vec{\pi} + \vec{\theta}\sigma. \end{aligned} \quad (2.21)$$

In order to construct a chirally invariant Lagrangian, we now have to find suitable combinations of the sigma and pion fields that respect chiral symmetry. Such a combination is, for example, given by $\vec{\pi}^2 + \sigma^2$ which remains unchanged under vector as well as axial-vector transformations,

$$\Lambda_{V,A} : \quad \vec{\pi}^2 + \sigma^2 \rightarrow \vec{\pi}^2 + \sigma^2. \quad (2.22)$$

The kinetic part of the quark-meson Lagrangian can therefore be written as

$$\mathcal{L}_{\text{kin}} = i\bar{\psi}\gamma_\mu\partial^\mu\psi + \frac{1}{2}\partial_\mu\sigma\partial^\mu\sigma + \frac{1}{2}\partial_\mu\vec{\pi}\partial^\mu\vec{\pi}, \quad (2.23)$$

where the first term represents the kinetic term of massless quarks, which was discussed to be invariant under chiral transformations in Sec. 2.2, while the two other terms represent the kinetic terms of the mesons, which have the same chirally invariant structure as given by (2.22).

The interaction between quarks and mesons can be expressed as

$$\mathcal{L}_{\text{int}} = -h \left((i\bar{\psi}\gamma^5\vec{\tau}\psi)\vec{\pi} + \bar{\psi}\psi\sigma \right), \quad (2.24)$$

where h is the Yukawa coupling. This term is also invariant with respect to chiral transformations since the pions are coupled to a pseudo-scalar combination of quark fields and the sigma meson is coupled to a scalar combination. We note that the interaction term $h\bar{\psi}\psi\sigma$ corresponds to a quark mass term with $m_q = h\sigma$ and indeed generates a finite constituent quark mass in the case of a non-vanishing expectation value of the sigma field. In the vacuum, we require the expectation value of the sigma field to agree with the pion decay constant, i.e. $\langle\sigma\rangle = f_\pi$. This follows from applying the Goldberger-Treiman relation, Eq. (2.15), to quarks, where we use $g_a = 1$ and $g_{\pi NN} = h$.

2. The quark-meson model as an effective model for QCD

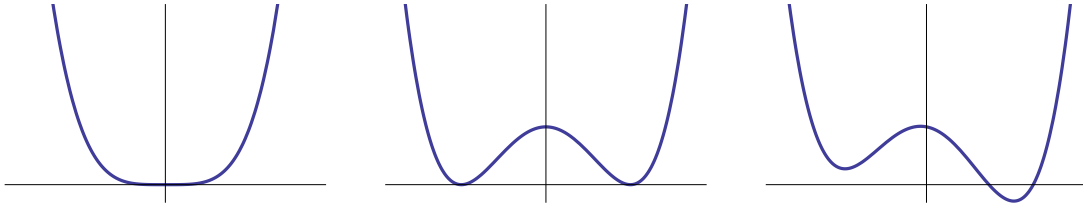


Figure 2.1.: The qualitative shape of the mesonic potential $U(\sigma, \vec{\pi})$ is shown in σ direction, for the case of a vanishing expectation value of the sigma field (left), for a spontaneously broken potential with $\langle \sigma \rangle \neq 0$ (center), and an explicitly broken potential including a term $c\sigma$ (right). Taken from [49].

As a last ingredient for the quark-meson model we introduce an effective mesonic potential of the form

$$U(\sigma, \vec{\pi}) \equiv U(\phi^2) - c\sigma, \quad (2.25)$$

which consists of a chirally invariant part, $U(\phi^2)$, and a term $c\sigma$ that explicitly breaks chiral symmetry and represents a bosonized version of the small but non-vanishing current quark mass term in QCD. The symmetric potential $U(\phi^2)$ is not specified further and may depend on arbitrary powers of the invariant combination $\phi^2 \equiv \vec{\pi}^2 + \sigma^2$, giving rise to various mesonic self interactions. A non-vanishing expectation value of the sigma field can then be produced by a spontaneously broken effective potential, cf. Fig. 2.1. The explicit symmetry breaking term, $c\sigma$, on the other hand, gives rise to a non-vanishing pion mass of

$$m_\pi^2 = \left. \frac{\partial^2 U(\sigma, \vec{\pi})}{\partial \pi^2} \right|_{\langle \sigma \rangle} = \frac{c}{f_\pi}, \quad (2.26)$$

where we used that the minimum of the effective potential is given by $\langle \sigma \rangle = f_\pi$.

Combining Eq. (2.23), Eq. (2.24) and Eq. (2.25) gives the following expression for the Lagrangian of the quark-meson model in Minkowski space-time,

$$\mathcal{L}_{QM} = \bar{\psi}(i\gamma_\mu \partial^\mu - h(\sigma + i\gamma^5 \vec{\tau} \vec{\pi}))\psi + \frac{1}{2}(\partial_\mu \sigma)^2 + \frac{1}{2}(\partial_\mu \vec{\pi})^2 - U(\sigma, \vec{\pi}). \quad (2.27)$$

We note that the quark-meson model is renormalizable, in contrast to, e.g., the Nambu–Jona-Lasinio (NJL) model [50, 51], which represents a purely fermionic effective model and is perturbatively non-renormalizable in four dimensions. Moreover, the quark-meson model is expected to fall into the same universality class as QCD and may therefore be used to draw qualitative conclusions on critical phenomena of strongly interacting matter, cf. for example [23].

In this thesis, we will subject the quark-meson model to a Functional Renormalization Group study that focuses on the calculation of spectral functions and transport coefficients. Since the FRG is usually formulated in Euclidean space-time, we will conclude this section by deriving the Euclidean version of the quark-meson Lagrangian. To that aim, we

2. The quark-meson model as an effective model for QCD

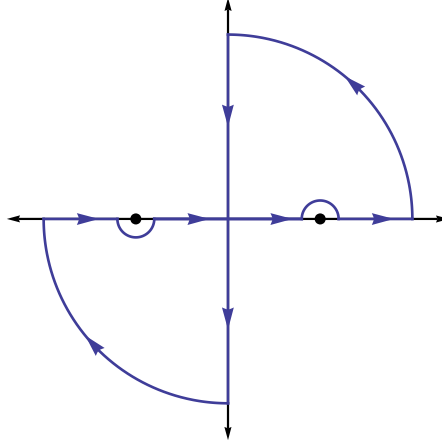


Figure 2.2.: In order to perform a Wick rotation, the integration along the real time or energy axis is translated to an integration along the imaginary axis by using the represented integration contour. Generic poles along the real axis are represented by solid dots. For example, the propagator of a free scalar field exhibits poles at $\omega = -m$ and $\omega = +m$, which are circumnavigated using the represented Feynman contour.

perform a Wick rotation of the QM Lagrangian, as given by Eq. (2.27), from Minkowski space-time to Euclidean space-time, which basically implies switching from real time to imaginary time via the replacement $t \rightarrow -i\tau$, where τ is the Euclidean time variable. Such a rotation of the time axis can be performed when the integrand has no singularities in the first and third quadrant of the complex plane and decreases fast enough asymptotically, see also Fig. 2.2.

Explicitly, after performing the replacement $t \rightarrow -i\tau$ in Eq. (2.27), we get

$$\mathcal{L}_{QM}(t \rightarrow -i\tau) = \bar{\psi}(i\gamma_0\partial^0 + \gamma_j\partial^j) - h(\sigma + i\gamma^5\vec{\tau}\vec{\pi})\psi - \frac{1}{2}(\partial_\mu\sigma)^2 - \frac{1}{2}(\partial_\mu\vec{\pi})^2 - U(\sigma, \vec{\pi}). \quad (2.28)$$

We now have to replace the gamma matrices appearing in this expression by their Euclidean counterparts. For the chiral representation, cf. App. A, the Minkowski and Euclidean gamma matrices are related by $\gamma_j^M = i\gamma_j^E$, while γ_0 and γ_5 remain unchanged. In Euclidean space-time the Lagrangian of the quark-meson model then reads

$$\mathcal{L}_{QM}^E = \bar{\psi}(\gamma_\mu\partial^\mu + h(\sigma + i\gamma^5\vec{\tau}\vec{\pi}))\psi + \frac{1}{2}(\partial_\mu\sigma)^2 + \frac{1}{2}(\partial_\mu\vec{\pi})^2 + U(\sigma, \vec{\pi}), \quad (2.29)$$

where we suppressed the Euclidean labels on the right-hand side and included an overall minus sign in the definition of the Euclidean Lagrangian.

3

Flow equations for the quark-meson model

We will now make use of the Functional Renormalization Group framework and derive flow equations for the quark-meson model. To that aim, we will first introduce some basic aspects of the FRG in Sec. 3.1. Then, the flow equation for the effective potential of the QM model is presented in Sec. 3.2, while flow equations for the mesonic 2-point functions are derived in Sec. 3.3. We note that Euclidean space-time will be used throughout this section. The analytic continuation procedure necessary to obtain flow equations for the retarded 2-point functions is discussed in Ch. 4.

3.1 Basic ideas of the Functional Renormalization Group

The Functional Renormalization Group represents a powerful continuum framework for non-perturbative calculations, in particular in quantum field theory and statistical physics, see for example [19, 20, 21, 22, 23, 24] for reviews. The basic aim is to understand the macroscopic physics at large distances, or small momenta, in terms of the underlying microscopic interaction. The connection between the microscopic and the macroscopic regime is then given by so-called flow equations which provide for a continuous interpolation between ultraviolet (UV) and infrared (IR) scales. By means of these flow equations, quantum fluctuations from intermediate scales are taken into account successively, momentum shell by momentum shell, as the RG energy scale k is lowered from some UV cutoff down to zero.

The central object within the FRG framework is the effective average action Γ_k , which is a simple generalization of the usual effective action Γ , cf. App. B. Therefore, it contains all physical information on, e.g. masses, form factors, scattering amplitudes and couplings. At the UV scale Λ , the effective average action should agree with the bare or classical action which is usually provided by some model ansatz and does not include any fluctuations. For a system including bosonic as well as fermionic fields, the

3. Flow equations for the quark-meson model

$$\partial_k \Gamma_k = \frac{1}{2} \text{ (dashed circle with blue dot) } - \text{ (solid circle with red dot) }$$

Figure 3.1.: The flow equation for the effective average action, Eq. (3.1), is represented diagrammatically. Dashed (solid) lines refer to bosonic (fermionic) fields while circles represent appropriate regulator insertions $\partial_k R_k$. From [55].

scale dependence of the effective average action Γ_k is given by the following exact flow equation [52, 53], which is also known as Wetterich equation and reads¹

$$\begin{aligned} \partial_k \Gamma_k[\phi, \psi, \bar{\psi}] = & \frac{1}{2} \text{Tr} \left\{ \partial_k R_k^B \left(\Gamma_k^{(2,0,0)}[\phi, \psi, \bar{\psi}] + R_k^B \right)^{-1} \right\} \\ & - \text{Tr} \left\{ \partial_k R_k^F \left(\Gamma_k^{(0,1,1)}[\phi, \psi, \bar{\psi}] + R_k^F \right)^{-1} \right\}. \end{aligned} \quad (3.1)$$

Therein, the trace represents an integration over the internal loop momentum q as well as a summation over flavor, color and Dirac indices. The bosonic and fermionic regulator functions are denoted as R_k^B and R_k^F , which are in the following chosen as

$$R_k^B(q) = (k^2 - \vec{q}^2)\theta(k^2 - \vec{q}^2), \quad (3.2)$$

$$R_k^F(q) = i\vec{q}(\sqrt{k^2/\vec{q}^2} - 1)\theta(k^2 - \vec{q}^2), \quad (3.3)$$

which represent three-dimensional analogues of the LPA-optimized regulator functions [54], where LPA refers to the local potential approximation, as introduced below. The functional derivatives of the effective average action with respect to the fields are defined as

$$\Gamma_k^{(l,m,n)}[\phi, \psi, \bar{\psi}] \equiv \frac{\delta^l}{\delta \phi^l} \frac{\delta^n}{\delta \bar{\psi}^n} \Gamma_k[\phi, \psi, \bar{\psi}] \frac{\overleftarrow{\delta^m}}{\delta \psi^m}. \quad (3.4)$$

Since the second functional derivative of the effective action represents the inverse of the propagator, cf. App. B, we define the scale-dependent Euclidean propagators as

$$D_k^B(q) \equiv \left(\Gamma_k^{(2,0,0)}(q) + R_k^B(q) \right)^{-1}, \quad (3.5)$$

$$D_k^F(q) \equiv \left(\Gamma_k^{(0,1,1)}(q) + R_k^F(q) \right)^{-1}. \quad (3.6)$$

A diagrammatic representation of the Wetterich equation, Eq. (3.1), is given by Fig. 3.1. We note that it has a simple one-loop structure, arising from the trace over the propagators. This one-loop structure will play a key role when performing the analytic

¹For a derivation of the Wetterich equation we refer to App. B.

3. Flow equations for the quark-meson model

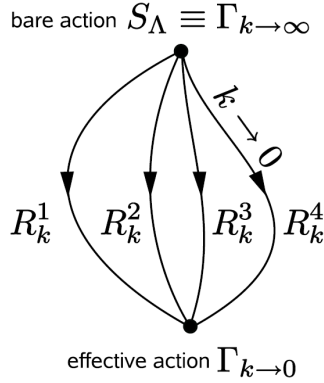


Figure 3.2.: Graphical representation of the flow of the effective average action, Γ_k , taken from [23]. At the UV scale, the effective average action is given by the classical or bare action S_Λ , while the full effective action Γ is recovered in the limit $k \rightarrow 0$. At intermediate scales, Γ_k depends on the chosen regulator function.

continuation procedure in order to calculate spectral functions in Ch. 4.

We note that the infrared regulator functions R_k^B and R_k^F appearing in Eq. (3.1) act as momentum-dependent mass terms and ensure the successive integration of fluctuations by satisfying the following properties. In order to implement IR regularization, a regulator function R_k is required to behave like $R_k(q) \simeq k^2$ for Euclidean momenta much smaller than the RG scale k , i.e. $q^2 \ll k^2$, which implies that the corresponding field components acquire an effective mass proportional to k and decouple from the dynamics, cf. [56]. On the other hand, the regulator function should vanish rapidly for $q^2 \gg k^2$ in order to recover the full effective action in the limit $k \rightarrow 0$. In general, the effective average action will depend on the chosen regulator function at intermediate scales, cf. Fig. 3.2. This regulator dependence is only removed in the limit $k \rightarrow 0$ upon solving the Wetterich equation exactly. In practise, however, truncations and approximations are necessary in order to solve this functional differential equation, and thus the regulator dependence is not removed completely.

The general idea of such truncation schemes is to turn the flow equation for the effective average action, Eq. (3.1), which represents a functional differential equation, into a coupled system of non-linear ordinary or partial differential equations by means of an expansion of Γ_k in terms of invariants with respect to its symmetries. In the following we will use the so-called derivative expansion in order to make an ansatz for the effective average action Γ_k . For a discussion of alternative truncation schemes like the vertex expansion or an expansion in the canonical dimension we refer to the literature, see e.g. [19, 20, 21, 22, 24].

For a scalar field theory, the derivative expansion of the effective average action is

3. Flow equations for the quark-meson model

given by

$$\Gamma_k[\phi] = \int d^4x \left\{ U_k(\phi) + \frac{1}{2} Z_k(\phi) (\partial_\mu \phi)^2 + \frac{1}{8} Y_k(\phi) (\partial_\mu \phi^2)^2 + \mathcal{O}(\partial^4) \right\}, \quad (3.7)$$

where the first corrections include the field- and scale dependent wave function renormalization factors $Z_k(\phi)$ and $Y_k(\phi)$. To lowest order, only the effective potential $U_k(\phi)$ carries a scale-dependence and the wave function renormalization factors are set to $Z_k(\phi) = 1$ and $Y_k(\phi) = 0$. This is known as the local potential approximation (LPA), which has been successfully applied to study, for example, critical phenomena, see, e.g., [57, 58]. We note, however, that controlling the truncation error of such non-perturbative analytic methods is, in general, not an easy task.

3.2 Flow equation for the effective potential of the QM model and thermodynamic observables

We will now use the local potential approximation in order to obtain an ansatz for the effective average action of the quark-meson model. Using the Euclidean Lagrangian of the QM model, cf. Eq. (2.29), we get

$$\Gamma_k[\bar{\psi}, \psi, \phi] = \int d^4x \left\{ \bar{\psi} (\gamma_\mu \partial^\mu + h(\sigma + i\vec{\tau}\vec{\pi}\gamma^5) - \mu\gamma_0) \psi + \frac{1}{2} (\partial_\mu \phi)^2 + U_k(\phi^2) \right\}, \quad (3.8)$$

where we introduced a finite quark chemical potential via the standard replacement $\partial^0 \rightarrow \partial^0 - \mu$. We note that the effective potential only includes the symmetric part, $U_k(\phi^2)$, since the explicit symmetry breaking term $c\sigma$ is only added to the effective potential in the IR, i.e. after solving the flow equation, since a linear symmetry breaking term remains unchanged in the RG flow [59]. We also note that the effective potential is the only scale-dependent quantity in this truncation. In particular, we neglect a possible running of the Yukawa coupling h , cf. for example [25, 60, 61], where this is taken into account. Moreover, as already mentioned, we do not include corrections arising from a non-trivial flow of the wave function renormalization factors. For the purpose of this thesis, where the focus is on qualitative rather than quantitative results, these approximations seem to be well justified, cf. also [62].

We will now apply the Wetterich equation, Eq. (3.1), to the LPA Ansatz for the effective average action of the quark-meson model, Eq. (3.8), in order to obtain the flow equation for the effective potential. An explicit derivation is provided in App. B and yields

$$\begin{aligned} \partial_k U_k = \frac{k^4}{12\pi^2} & \left[\frac{1}{E_{\sigma,k}} \coth\left(\frac{E_{\sigma,k}}{2T}\right) + \frac{3}{E_{\pi,k}} \coth\left(\frac{E_{\pi,k}}{2T}\right) \right. \\ & \left. - \frac{2N_c N_f}{E_{\psi,k}} \left(\tanh\left(\frac{E_{\psi,k} - \mu}{2T}\right) + \tanh\left(\frac{E_{\psi,k} + \mu}{2T}\right) \right) \right], \quad (3.9) \end{aligned}$$

3. Flow equations for the quark-meson model

where the effective quasi-particle energies are defined as

$$E_{\sigma,k}^2 \equiv k^2 + m_\sigma^2 \equiv k^2 + 2U'_k(\phi^2) + 4\phi^2 U''_k(\phi^2), \quad (3.10)$$

$$E_{\pi,k}^2 \equiv k^2 + m_\pi^2 \equiv k^2 + 2U'_k(\phi^2), \quad (3.11)$$

$$E_{\psi,k}^2 \equiv k^2 + m_\psi^2 \equiv k^2 + h^2 \phi^2. \quad (3.12)$$

The structure of the flow equation for the effective potential, Eq. (3.9), can be interpreted as follows. The first two terms correspond to the bosonic contributions from the sigma meson and the three pions, which tend to restore chiral symmetry. The fermionic quark term, on the other hand, enters the flow equation with a relative minus sign and is responsible for generating a non-vanishing quark condensate at intermediate scales. It exhibits a degeneracy factor of $2N_c N_f$ due to spin, color and flavor degrees of freedom.

Using a simplified notation in terms of threshold functions, cf. App.C, the flow equation for the effective potential can also be expressed as

$$\partial_k U_k = \frac{1}{2} I_{k,\sigma}^{(1)} + \frac{3}{2} I_{k,\pi}^{(1)} - N_c N_f I_{k,\psi}^{(1)}. \quad (3.13)$$

This flow equation has to be solved numerically, cf. Ch. 6, in order to obtain the effective potential in the IR. The global minimum of the effective potential then defines the thermodynamic grand potential per volume, the Landau free-energy density,

$$\Omega(T, \mu) \equiv U_{k \rightarrow 0}(T, \mu) \Big|_{\langle \sigma \rangle}, \quad (3.14)$$

which allows access to many thermodynamic quantities. The pressure, for example, is given by

$$p(T, \mu) = -\Omega(T, \mu) + \Omega(0, 0), \quad (3.15)$$

which is normalized to zero in the vacuum. By taking derivatives of the pressure with respect to temperature and chemical potential, one obtains the entropy density s and the quark number density n_q , i.e.

$$s(T, \mu) = \frac{\partial p(T, \mu)}{\partial T}, \quad (3.16)$$

$$n_q(T, \mu) = \frac{\partial p(T, \mu)}{\partial \mu}. \quad (3.17)$$

At high temperatures, the calculation of thermodynamic quantities is hampered by the finite UV cutoff Λ , since thermal modes with $2\pi T > \Lambda$ are excluded. This limitation can be remedied as follows. At large scales, $k \geq \Lambda$, quarks are expected to be the relevant degrees of freedom. The missing high-momentum modes can therefore be included in the effective potential by integrating the fermionic part of Eq. (3.9) from $k \rightarrow \infty$ to Λ [63, 64, 65], where we use $m_\psi = 0$. The result is then added to the effective potential at

3. Flow equations for the quark-meson model

the UV scale,

$$U_\Lambda(\phi^2) \rightarrow U_\Lambda(\phi^2) + U_\Lambda^\infty(\phi^2). \quad (3.18)$$

Using this corrected UV potential as input at $k = \Lambda$ for the full flow equation of the effective potential, Eq. (3.9), then allows to compute thermodynamic observables at high temperatures. The obtained results can be compared to the corresponding Stefan-Boltzmann values, which characterize a non-interacting gas of massless particles. For example, the Stefan-Boltzmann pressure of a gas of massless quarks and gluons is given by

$$\frac{p_{\text{SB}}}{T^4} = \frac{N_c N_f}{6} \left[\frac{7\pi^2}{30} + \left(\frac{\mu}{T}\right)^2 + \frac{1}{2\pi^2} \left(\frac{\mu}{T}\right)^4 \right] + (N_c^2 - 1) \frac{\pi^2}{45}. \quad (3.19)$$

3.3 Flow equations for the mesonic two-point functions of the QM model and thermodynamic consistency

In order to calculate spectral functions, we first have to calculate the retarded two-point functions. To that aim, we will now derive flow equations for the Euclidean mesonic two-point functions $\Gamma_{\sigma,k}^{(2)}$ and $\Gamma_{\pi,k}^{(2)}$ of the QM model.² The flow equations for the retarded two-point functions can then be obtained via analytic continuation, see also Ch. 4.

In general, flow equations for higher n -point functions can be obtained by taking n functional derivatives of the flow equation for the effective average action, Eq. (3.1), with respect to the fields. This gives rise to the following generic structure of the flow equation for a bosonic two-point function

$$\begin{aligned} \partial_k \Gamma_k^{(2)} &= \frac{1}{2} \frac{\delta^2}{\delta \phi^2} \text{Tr} \{ \partial_k R_k D_k \} \\ &= -\frac{1}{2} \text{Tr} \left\{ \partial_k R_k \frac{\delta}{\delta \phi} \left(D_k \Gamma_k^{(3)} D_k \right) \right\} \\ &= \text{Tr} \left\{ \partial_k R_k \left(D_k \Gamma_k^{(3)} D_k \Gamma_k^{(3)} D_k \right) \right\} - \frac{1}{2} \text{Tr} \left\{ \partial_k R_k \left(D_k \Gamma_k^{(4)} D_k \right) \right\}, \end{aligned} \quad (3.20)$$

see also Fig. 3.3. We note that the above flow equation for a two-point function depends on the scale dependent three- and four-point functions $\Gamma_k^{(3)}$ and $\Gamma_k^{(4)}$. In general, the flow equation for an n -point function requires information on the scale dependence of the $(n+1)$ - and $(n+2)$ -point functions, which gives rise to an infinite tower of flow equations. Since we cannot solve such an infinite system of equations exactly, we will truncate it at $n_{\text{max}} = 4$. Moreover, we will neglect the momentum dependence of the three- and four-point functions, which can be taken into account by more involved truncation schemes such as the BMW approximation [66, 67]. Another possible extension that takes

²We note that we will use a simplified notation for functional derivatives in the following, as compared to Eq. (3.4), which will be self-evident from the respective context.

3. Flow equations for the quark-meson model

$$\begin{aligned}
\partial_k \Gamma_{k,\sigma}^{(2)} &= \text{Diagram 1} + \text{Diagram 2} - \frac{1}{2} \text{Diagram 3} - \frac{1}{2} \text{Diagram 4} - 2 \text{Diagram 5} \\
\partial_k \Gamma_{k,\pi}^{(2)} &= \text{Diagram 6} + \text{Diagram 7} - \frac{1}{2} \text{Diagram 8} - \frac{1}{2} \text{Diagram 9} - 2 \text{Diagram 10}
\end{aligned}$$

Figure 3.3.: Diagrammatic representation of the flow equations for the sigma and pion two-point functions, cf. Eqs. (3.23)-(3.24). Dashed (solid) lines denote bosonic (fermionic) propagators, as indicated by respective labels. Bosonic (fermionic) regulator insertions are represented by blue (red) circles while bosonic (fermionic) three-point functions are denoted as blue (red) triangles and bosonic four-point functions are represented by blue squares. From [68].

into account a non-trivial momentum dependence of the propagators in an iterative way was proposed in [62].

In the following, we will extract the scale-dependent three- and four-point functions from the effective potential, i.e.

$$\begin{aligned}
\Gamma_{k,\phi_i\phi_j\phi_m}^{(3)} &= 4U_k'' (\delta_{ij}\phi_m + \delta_{im}\phi_j + \delta_{jm}\phi_i) \\
&\quad + 8U_k^{(3)} \phi_i\phi_j\phi_m, \tag{3.21}
\end{aligned}$$

$$\begin{aligned}
\Gamma_{k,\phi_i\phi_j\phi_m\phi_n}^{(4)} &= 4U_k'' (\delta_{ij}\delta_{mn} + \delta_{in}\delta_{jm} + \delta_{jn}\delta_{im}) \\
&\quad + 8U_k^{(3)} (\delta_{ij}\phi_m\phi_n + \delta_{jm}\phi_i\phi_n + \delta_{mn}\phi_i\phi_j \\
&\quad\quad + \delta_{jn}\phi_i\phi_m + \delta_{in}\phi_j\phi_m + \delta_{im}\phi_j\phi_n) \\
&\quad + 16U_k^{(4)} \phi_i\phi_j\phi_m\phi_n, \tag{3.22}
\end{aligned}$$

with $\phi_i = (\sigma, \vec{\pi})_i$ and where $U_k^{(n)}$ represents the n -th derivative of the effective potential with respect to ϕ^2 .

The flow equations for the sigma and the pion two-point functions are then given by

$$\begin{aligned}
\partial_k \Gamma_{k,\sigma}^{(2)}(p) &= J_{k,\sigma\sigma}(p) \left(\Gamma_{k,\sigma\sigma\sigma}^{(3)} \right)^2 + 3 J_{k,\pi\pi}(p) \left(\Gamma_{k,\sigma\pi\pi}^{(3)} \right)^2 \\
&\quad - \frac{1}{2} I_{k,\sigma}^{(2)} \Gamma_{k,\sigma\sigma\sigma\sigma}^{(4)} - \frac{3}{2} I_{k,\pi}^{(2)} \Gamma_{k,\sigma\sigma\pi\pi}^{(4)} - 2N_c N_f J_{k,\bar{\psi}\psi}^{(\sigma)}(p), \tag{3.23}
\end{aligned}$$

$$\begin{aligned}
\partial_k \Gamma_{k,\pi}^{(2)}(p) &= J_{k,\sigma\pi}(p) \left(\Gamma_{k,\sigma\pi\pi}^{(3)} \right)^2 + J_{k,\pi\sigma}(p) \left(\Gamma_{k,\sigma\pi\pi}^{(3)} \right)^2 \\
&\quad - \frac{1}{2} I_{k,\sigma}^{(2)} \Gamma_{k,\sigma\sigma\pi\pi}^{(4)} - \frac{5}{2} I_{k,\pi}^{(2)} \Gamma_{k,\pi\pi\bar{\pi}\bar{\pi}}^{(4)} - 2N_c N_f J_{k,\bar{\psi}\psi}^{(\pi)}(p), \tag{3.24}
\end{aligned}$$

3. Flow equations for the quark-meson model

with $\pi, \tilde{\pi} \in \{\pi_1, \pi_2, \pi_3\}$ and $\pi \neq \tilde{\pi}$, cf. Fig. 3.3 for a diagrammatic representation. The external Euclidean 4-momentum is denoted as p and will always be routed through the “upper” leg of the loops depicted in Fig. 3.3, i.e. the ones with the regulator insertion $\partial_k R_k$. The reason for this choice of routing is merely technical, cf. the discussion in App. C. We also checked explicitly that our results do not depend on the momentum routing. The bosonic and fermionic threshold or loop functions $J_{k,\alpha\beta}(p)$ and $J_{k,\bar{\psi}\psi}^{(\alpha)}(p)$ are then given by

$$J_{k,\alpha\beta}(p) = \text{Tr} [\partial_k R_k^B(q+p) D_{k,\alpha}(q+p)^2 D_{k,\beta}(q)], \quad (3.25)$$

$$J_{k,\bar{\psi}\psi}^{(\alpha)}(p) = \text{Tr} [\partial_k R_k^F(q+p) D_{k,\psi}(q+p) \Gamma_{\bar{\psi}\psi\alpha}^{(2,1)} D_{k,\psi}(q) \Gamma_{\bar{\psi}\psi\alpha}^{(2,1)} D_{k,\psi}(q+p)], \quad (3.26)$$

with $\alpha, \beta \in \{\sigma, \pi\}$. Therein, the quark-meson three-point vertex function $\Gamma_{\bar{\psi}\psi\alpha}^{(2,1)}$ is obtained by taking two fermionic and one bosonic derivative of Eq. (3.8), i.e.

$$\Gamma_{\bar{\psi}\psi\phi_i}^{(2,1)} = h \begin{cases} 1 & \text{for } i = 0 \\ i\gamma^5 \tau^i & \text{for } i = 1, 2, 3. \end{cases} \quad (3.27)$$

We note that our truncation is thermodynamically consistent in the sense that the two-point functions, evaluated at vanishing external momentum, agree with the curvature masses as extracted from the scale-dependent effective potential, cf. Eq. (3.10). This relation also holds for the respective flow equations, i.e.

$$\partial_k \Gamma_{\pi,k}^{(2)}(p=0) = 2\partial_k U_k', \quad (3.28)$$

$$\partial_k \Gamma_{\sigma,k}^{(2)}(p=0) = 2\partial_k U_k' + 4\partial_k U_k'' \phi^2, \quad (3.29)$$

cf. [17, 29]. This consistency is a simple consequence of determining the higher n -point vertices solely from the effective potential. It also holds at finite temperature and Euclidean external momenta. However, once the analytic continuation has been performed, cf. Ch. 5, the two limits of taking $\omega \rightarrow 0$ at $\vec{p} = 0$ and taking $\vec{p} \rightarrow 0$ at $\omega = 0$ do not commute, as also discussed in [31, 30, 69], and give different results for the flow equations of the two-point functions in Eqs. (3.28)-(3.29). In particular, the time-like limit of taking $\omega \rightarrow 0$ at $\vec{p} = 0$ gives the so-called plasmon mass while the space-like limit of taking $\vec{p} \rightarrow 0$ at $\omega = 0$ yields the screening mass. In the Euclidean case, these two limits commute and give the corresponding screening masses, which therefore agree with the curvature masses within our truncation. The above identities, Eqs. (3.28)-(3.29), then have to be understood as representing the space-like limit of taking $\vec{p} \rightarrow 0$ at $\omega = 0$.

4

Analytic continuation and spectral functions

In this chapter, we will first discuss the basic idea of analytic continuation in Sec. 4.1 and then present a simple example for an analytic continuation on the basis of a one-loop calculation in Sec. 4.2. The two-step analytic continuation procedure employed in this thesis to obtain flow equations for retarded two-point functions is presented in Sec. 4.3, which allows for the calculation of spectral functions. Basic properties of spectral functions are discussed in Sec. 4.4 and simple examples as well as a guideline for their interpretation are provided in Sec. 4.5.

4.1 Basic idea of analytic continuation

Analytic continuation generally refers to the task of extending the domain of a function $f(i\omega_n)$, that is only defined at discrete values along the imaginary axis, towards the entire complex plane, and in particular to the real axis, see also Fig. 4.1. Such an analytically continued function $F(z)$ then has to agree with the original function at the points $i\omega_n$, i.e.

$$F(z)\Big|_{z=i\omega_n} = f(i\omega_n). \quad (4.1)$$

In general, there are infinitely many ways to define such an analytic continuation, even when based on an infinite number of discrete points. Therefore, one has to impose boundary conditions in order to make this process unique. In particular, the physical boundary conditions, also known as Baym-Mermin boundary conditions [10], require $F(z)$ to be bounded as $|z| \rightarrow \infty$, and $F(z)$ to be analytic off, i.e. outside, the real axis.

In practise, however, analytic continuation procedures are often performed numerically and based on a discrete and finite set of data points. This is, for example, the case in lattice QCD calculations, where one aims at reconstructing real-time correlations

4. Analytic continuation and spectral functions

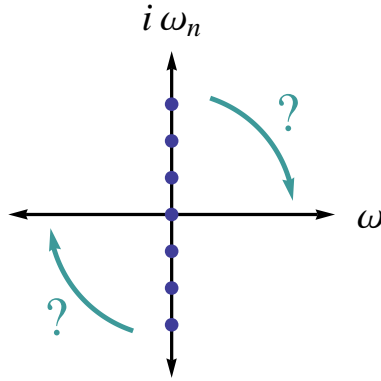


Figure 4.1.: Graphical representation of the analytic continuation problem. Based on discrete imaginary energies $i\omega_n$, the domain of some function $F(z)$ has to be extended to real energies ω .

based on numerical data at discrete imaginary Matsubara frequencies [12, 13, 70]. When based on such numerical schemes, the analytic continuation from Euclidean to Minkowski space-time is classified as an ill-posed inverse problem.

In this thesis, we use an analytical continuation procedure that does not rely on numerical techniques but can be performed analytically. It can be motivated by a simple one-loop example as discussed in the next section.

4.2 Simple one-loop example

Let us consider the following simple model, which is taken from [31] and consists of two bosonic fields, ϕ and B , that are described by the Lagrangian

$$\mathcal{L} = \frac{1}{2}(\partial_\mu\phi)^2 + \frac{1}{2}(\partial_\mu B)^2 - \frac{m^2}{2}\phi^2 - \frac{M^2}{2}B^2 - \frac{g}{2}\phi B^2, \quad (4.2)$$

where we assume that B describes some heavier particle than ϕ . We will now calculate the contribution of the B -field to the self-energy of the lighter mass field ϕ . At finite temperature the one-loop result for the Euclidean self-energy reads

$$\Pi^E(p_0, \vec{p}) = \frac{g^2 T}{2} \sum_n \int \frac{d^3 q}{(2\pi)^3} \frac{1}{\omega_n^2 + \vec{q}^2 + M^2} \frac{1}{(\omega_n + p_0)^2 + (\vec{q} + \vec{p})^2 + M^2}, \quad (4.3)$$

where the internal energy is given by discrete Matsubara frequencies, i.e. $\omega_n = 2n\pi T$. Moreover, also the external energy p_0 is assumed to be discrete at finite temperature. We note that $\Pi^E(p_0, \vec{p})$ has a simple one-loop structure in terms of Euclidean propagators, see also Fig. 4.2.

4. Analytic continuation and spectral functions

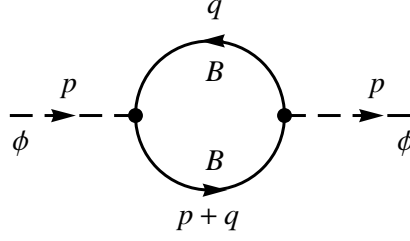


Figure 4.2.: Diagrammatic representation of the self-energy $\Pi(p_0, \vec{p})$, as given by Eq. (4.3). Dashed lines are associated to the light ϕ -field with external momentum p , while solid lines represent the heavier B -field with internal momentum q .

Using the notation

$$\omega_q^2 \equiv \vec{q}^2 + M^2, \quad (4.4)$$

$$\omega_{q+p}^2 \equiv (\vec{q} + \vec{p})^2 + M^2, \quad (4.5)$$

the Euclidean self energy $\Pi(p_0, \vec{p})$ can be written as

$$\begin{aligned} \Pi^E(p_0, \vec{p}) = \frac{g^2}{8} \int \frac{d^3 q}{(2\pi)^3} & \left[\frac{1}{\omega_q} (1 + 2n_B(\omega_q)) \left(\frac{1}{\omega_{q+p}^2 - (\omega_q + ip_0)^2} + \frac{1}{\omega_{q+p}^2 - (\omega_q - ip_0)^2} \right) \right. \\ & + \frac{1}{\omega_{q+p}} (1 + 2n_B(\omega_{q+p} + ip_0)) \frac{1}{\omega_q^2 - (\omega_{q+p} + ip_0)^2} \\ & \left. + \frac{1}{\omega_{q+p}} (1 + 2n_B(\omega_{q+p} - ip_0)) \frac{1}{\omega_q^2 - (\omega_{q+p} - ip_0)^2} \right], \quad (4.6) \end{aligned}$$

where the bosonic occupation number $n_B(E)$ is defined by Eq. (C.4). We note that the self-energy given by Eq. (4.6) is analytic in the origin, i.e. the two limits of taking $p_0 \rightarrow 0$ at $\vec{p} = 0$ and of taking $\vec{p} \rightarrow 0$ at $p_0 = 0$ commute,

$$\lim_{p_0 \rightarrow 0} \lim_{\vec{p} \rightarrow 0} \Pi(p_0, \vec{p}) = \lim_{\vec{p} \rightarrow 0} \lim_{p_0 \rightarrow 0} \Pi(p_0, \vec{p}). \quad (4.7)$$

However, if we now use the fact that the Euclidean external energy is given by discrete Matsubara frequencies, i.e. $p_0 = 2l\pi T$, the self-energy becomes

$$\begin{aligned} \Pi^E(p_0, \vec{p}) = \frac{g^2}{8} \int \frac{d^3 q}{(2\pi)^3} & \left[\frac{1}{\omega_q} (1 + 2n_B(\omega_q)) \left(\frac{1}{\omega_{q+p}^2 - (\omega_q + ip_0)^2} + \frac{1}{\omega_{q+p}^2 - (\omega_q - ip_0)^2} \right) \right. \\ & + \frac{1}{\omega_{q+p}} (1 + 2n_B(\omega_{q+p})) \frac{1}{\omega_q^2 - (\omega_{q+p} + ip_0)^2} \\ & \left. + \frac{1}{\omega_{q+p}} (1 + 2n_B(\omega_{q+p})) \frac{1}{\omega_q^2 - (\omega_{q+p} - ip_0)^2} \right], \quad (4.8) \end{aligned}$$

4. Analytic continuation and spectral functions

where we used the periodicity of the bosonic occupation number with respect to multiples of $i2\pi T$, i.e.

$$n_B(E + i2l\pi T) = n_B(E). \quad (4.9)$$

If we now study the two different limits again and let p_0 assume continuous values for this purpose, it turns out that the two limits do no longer commute and that hence the self-energy given by Eq. (4.8) is no longer analytic in the origin,

$$\lim_{p_0 \rightarrow 0} \lim_{\vec{p} \rightarrow 0} \Pi(p_0, \vec{p}) \neq \lim_{\vec{p} \rightarrow 0} \lim_{p_0 \rightarrow 0} \Pi(p_0, \vec{p}). \quad (4.10)$$

This non-analyticity does not appear in zero temperature field theory, where Lorentz invariance forces the self energy to be a function of the external four-momentum p^μ . At finite temperature, however, Lorentz invariance is broken since the heat bath singles out a specific frame of reference.¹

The two different limits can also be interpreted physically. The space-like limit of taking $\vec{p} \rightarrow 0$ at $p_0 = 0$ corresponds to taking the static limit and leads to the screening mass, while the time-like limit of taking $p_0 \rightarrow 0$ at $\vec{p} = 0$ gives the plasmon mass. In the case of the analytic self-energy given by Eq. (4.6), both limits agree and give the same result as the space-like limit of Eq. (4.8).

We conclude that first using the periodicity of the occupation number with respect to the external Euclidean momentum and then allowing the external momentum to assume continuous values allows access to real-time information like the plasmon mass. The final step of the analytic continuation procedure towards Minkowski space and a real energy ω is now straightforward. The retarded self-energy, for example, can be obtained from the Euclidean expression, Eq. (4.8), by substituting the Euclidean energy p_0 by a continuous real energy ω in the following way,

$$\Pi^R(\omega, \vec{p}) = - \lim_{\epsilon \rightarrow 0} \Pi^E(p_0 = -i(\omega + i\epsilon), \vec{p}), \quad (4.11)$$

see also Eq. (4.26) and Sec. 4.4. It can be shown that this procedure indeed yields the correct analytic continuation and fulfills the physical Baym-Mermin boundary conditions by a comparison to results from, e.g., real-time methods [11].

4.3 Analytic continuation of flow equations

We will now use the analytic continuation procedure discussed in the last section to obtain flow equations for the retarded two-point functions. This is possible since the flow equations for the 2-point functions have the same one-loop structure as the self-energy discussed in the last section, cf. Fig. 3.3, and since we are able to express them analytically in terms of occupation numbers. A formulation in terms occupation numbers is in turn made possible by using three-dimensional regulator functions, cf. Eqs. (3.2)-

¹We note that a covariant description is still possible at finite temperature, cf. [31].

4. Analytic continuation and spectral functions

(3.3), which do not affect the frequency component of the internal four-momentum and allow to perform the internal frequency integration, or Matsubara summation at finite temperature, on the right-hand side of the flow equations explicitly.²

The analytic continuation of the flow equations for the two-point functions now proceeds as follows. In a first step, we exploit the periodicity of the bosonic and fermionic occupation numbers with respect to their Euclidean energy argument $p_0 = 2n\pi T$, i.e.

$$n_{B,F}(E + ip_0) \rightarrow n_{B,F}(E), \quad (4.12)$$

see also [30, 71]. In a second step, the discrete Euclidean energy p_0 is replaced by a continuous real energy ω in the following way,

$$\partial_k \Gamma_k^{(2),R}(\omega, \vec{p}) = - \lim_{\epsilon \rightarrow 0} \partial_k \Gamma_k^{(2),E}(p_0 = -i(\omega + i\epsilon), \vec{p}), \quad (4.13)$$

where ϵ is taken to be a small real parameter in our numerical implementation. When performed in the given order, these two steps yield the physical Baym-Mermin boundary conditions [10, 11]. Explicit expressions for the analytically continued threshold or loop functions appearing in the flow equations of the two-point functions, cf. Eqs. (3.23)-(3.24), are given in App. C.

4.4 Definition and analytic properties of spectral functions

Spectral functions, also called spectral densities, are closely related to propagators and therefore encode a multitude of information, for example on the particle spectrum, masses, decay widths and decay channels. As a consequence, spectral functions can be used to calculate various observables, in particular real-time quantities like the shear viscosity, cf. Ch. 5. In the following we will discuss basic properties of spectral functions and relate them to the retarded two-point functions discussed previously. The notation and conventions used in this section are based on [71], cf. also App. A for the definitions of the Fourier representations used in this section.

We define the spectral function $\rho(\omega, \vec{p})$ as the difference between the retarded propagator $D^R(\omega, \vec{p})$ and the advanced propagator $D^A(\omega, \vec{p})$ in the following way,

$$\rho(\omega, \vec{p}) \equiv \frac{i}{2\pi} (D^R(\omega, \vec{p}) - D^A(\omega, \vec{p})), \quad (4.14)$$

where the retarded and advanced propagators for a scalar field $\phi(x)$ are given by

$$D^R(\omega, \vec{p}) \equiv D^R(p) = -i \int d^4x e^{ipx} \theta(x_0) \langle [\phi(x), \phi(0)] \rangle, \quad (4.15)$$

$$D^A(\omega, \vec{p}) \equiv D^A(p) = i \int d^4x e^{ipx} \theta(-x_0) \langle [\phi(x), \phi(0)] \rangle. \quad (4.16)$$

²For a discussion on the possible violation of Lorentz invariance due to the three-dimensional regulator functions, we refer to App. E.1.

4. Analytic continuation and spectral functions

We will now derive integral representations for the propagators in terms of the spectral function, i.e. the Källén-Lehmann spectral representations. To that aim we first note that the Green's function defined as

$$D(p) = \int d^4x e^{ipx} D(x) \equiv -i \int d^4x e^{ipx} \langle [\phi(x), \phi(0)] \rangle, \quad (4.17)$$

is related to the spectral function via

$$D(p) = \frac{2\pi}{i} \rho(p), \quad (4.18)$$

which follows from Eq. (4.14) and Eq. (4.15). The retarded propagator can then be written as

$$D^R(p) = \int d^4x \theta(x_0) D(x) e^{ipx}. \quad (4.19)$$

Together with the following integral representation of the theta-function,

$$\theta(x) = i \int \frac{d\omega'}{2\pi} \frac{e^{-i\omega'x}}{\omega' + i\epsilon}, \quad (4.20)$$

where the limit $\epsilon \rightarrow 0$ is implied, we can then write the retarded propagator as

$$D^R(p) = \int d^4x i \int \frac{d\omega'}{2\pi} \frac{e^{-i\omega'x}}{\omega' + i\epsilon} \int \frac{d\omega''}{2\pi} D(\omega'') e^{-i\omega''x} e^{ipx}. \quad (4.21)$$

Straightforward manipulations yield the following Källén-Lehmann spectral representation for the retarded propagator

$$D^R(\omega, \vec{p}) = - \int_{-\infty}^{\infty} \frac{\rho(\omega', \vec{p})}{\omega' - \omega - i\epsilon} d\omega'. \quad (4.22)$$

Similarly, one obtains the corresponding representation for the advanced propagator, which is given by

$$D^A(\omega, \vec{p}) = - \int_{-\infty}^{\infty} \frac{\rho(\omega', \vec{p})}{\omega' - \omega + i\epsilon} d\omega'. \quad (4.23)$$

These spectral representations can be generalized to complex values of ω . In this way, we obtain the analytic continuation $D(z)$ of the propagators as

$$D(z, \vec{p}) = - \int_{-\infty}^{\infty} \frac{\rho(\omega', \vec{p})}{\omega' - z} d\omega'. \quad (4.24)$$

In particular, when using $z = -ip_0$, we find the following spectral representation for the

4. Analytic continuation and spectral functions

Euclidean propagator,

$$D^E(p_0, \vec{p}) = \int_{-\infty}^{\infty} \frac{\rho(\omega', \vec{p})}{\omega' + ip_0} d\omega', \quad (4.25)$$

which is defined with an overall minus sign. By comparing this with Eq. (4.22) and Eq. (4.23), we find that the retarded and the advanced propagator can be obtained from the Euclidean propagator by analytic continuation, i.e.

$$D^R(\omega, \vec{p}) = -D^E(p_0 \rightarrow i\omega - \epsilon, \vec{p}), \quad (4.26)$$

$$D^A(\omega, \vec{p}) = -D^E(p_0 \rightarrow i\omega + \epsilon, \vec{p}). \quad (4.27)$$

This is equivalent to the analytic continuation used in Eq. (4.13) for the retarded two-point function. Similarly, the retarded and the advanced propagator can also be obtained from the analytic continuation $D(z)$ as follows,

$$D^R(\omega, \vec{p}) = D(z \rightarrow \omega + i\epsilon, \vec{p}), \quad (4.28)$$

$$D^A(\omega, \vec{p}) = D(z \rightarrow \omega - i\epsilon, \vec{p}), \quad (4.29)$$

cf. Eq. (4.24). By inserting these expression into Eq. (4.14), we can write the spectral function as

$$\rho(\omega, \vec{p}) = \frac{i}{2\pi} (D(z \rightarrow \omega + i\epsilon, \vec{p}) - D(z \rightarrow \omega - i\epsilon, \vec{p})), \quad (4.30)$$

which makes it evident that there has to be a non-analyticity on the real ω -axis in order for the spectral function to be non-vanishing. Such a non-analyticity can either be produced by a Dirac delta function, as for example in the case of a free particle, see also Sec. 4.5, or by a branch cut along the real axis, which represents the existence of decay channels for interacting particles, see also the discussion in Sec. 8.1. Such a branch cut gives rise to a discontinuity in the imaginary part of $D(z)$, while its real part does not change when crossing the real ω -axis. This can be seen from the following relations for the real and the imaginary part of the retarded and the advanced propagator,

$$\text{Im } D^R(\omega, \vec{p}) = -\text{Im } D^A(\omega, \vec{p}), \quad (4.31)$$

$$\text{Re } D^R(\omega, \vec{p}) = \text{Re } D^A(\omega, \vec{p}), \quad (4.32)$$

which follow from Eq. (4.22) and Eq. (4.23). We also note that the retarded propagator is analytic in the upper half of the complex ω -plane, while the advanced propagator is analytic in the lower half of the complex ω -plane.

By means of Eq. (4.31) we can express the spectral function solely in terms of the retarded propagator, i.e.

$$\rho(\omega, \vec{p}) = -\frac{1}{\pi} \text{Im } D^R(\omega, \vec{p}). \quad (4.33)$$

In terms of the retarded two-point function, $\Gamma^{(2),R}(\omega, \vec{p})$, which is essentially the inverse

4. Analytic continuation and spectral functions

of the retarded propagator, cf. Eq. (B.21), the spectral function is then given by

$$\rho(\omega, \vec{p}) = \frac{1}{\pi} \frac{\text{Im} \Gamma^{(2),R}(\omega, \vec{p})}{(\text{Re} \Gamma^{(2),R}(\omega, \vec{p}))^2 + (\text{Im} \Gamma^{(2),R}(\omega, \vec{p}))^2}. \quad (4.34)$$

This representation will be used in this thesis to calculate spectral functions based on retarded two-point functions.

We now summarize further important properties of spectral functions. For example, from

$$D^R(\omega, -\vec{p}) = D^R(\omega, \vec{p}), \quad (4.35)$$

$$D^R(-\omega, \vec{p}) = D^A(\omega, \vec{p}), \quad (4.36)$$

we find the following symmetry properties of the spectral function,

$$\rho(\omega, -\vec{p}) = \rho(\omega, \vec{p}), \quad (4.37)$$

$$\rho(-\omega, \vec{p}) = -\rho(\omega, \vec{p}), \quad (4.38)$$

$$\rho(-\omega, -\vec{p}) = -\rho(\omega, \vec{p}). \quad (4.39)$$

Moreover, the spectral function satisfies the sum rule

$$\int_{-\infty}^{\infty} d\omega \omega \rho(\omega, \vec{p}) = 1, \quad (4.40)$$

which can be derived by considering the derivative of the Green's function $D(x)$, as defined by Eq. (4.17), i.e.

$$\lim_{x_0 \rightarrow 0} \frac{\partial}{\partial x_0} D(x) = \lim_{x_0 \rightarrow 0} \int \frac{d^4 p}{(2\pi)^4} (-i\omega) e^{-ipx} D(p) = - \int \frac{d^3 p}{(2\pi)^3} e^{i\vec{p}\vec{x}} \int d\omega \omega \rho(\omega, \vec{p}), \quad (4.41)$$

where we used Eq. (4.18). On the other hand, we can express $D(x)$ in position space by using Eq. (4.17), which gives

$$\lim_{x_0 \rightarrow 0} \frac{\partial}{\partial x_0} D(x) = \lim_{x_0 \rightarrow 0} \frac{\partial}{\partial x_0} (-i \langle [\phi(x), \phi(0)] \rangle) = - \int \frac{d^3 p}{(2\pi)^3} e^{i\vec{p}\vec{x}}, \quad (4.42)$$

where we used the canonical commutation relation

$$i \langle [\hat{\pi}(0, \vec{x}), \hat{\phi}(0, \vec{0})] \rangle = \delta(\vec{x}) = \int \frac{d^3 p}{(2\pi)^3} e^{i\vec{p}\vec{x}}, \quad (4.43)$$

which holds for free fields. By comparing Eq. (4.41) with Eq. (4.42) we then find the sum rule given by Eq. (4.40).

We conclude this section by noting that spectral functions in general obeys the positivity

4. Analytic continuation and spectral functions

condition

$$\text{sgn}(\omega)\rho(\omega, \vec{p}) \geq 0, \quad (4.44)$$

which can be seen, for example, by writing the spectral function as a sum over a complete set of eigenstates, i.e.

$$\rho(p) = \sum_{\psi} (2\pi)^3 \delta^{(4)}(p - q_{\psi}) |\langle \Omega | \phi(0) | \psi \rangle|^2, \quad (4.45)$$

with $p_0 > 0$, see also [30, 71]. However, when dealing with non-observable degrees of freedom, such as quarks or gluons in the confined phase, there is, in general, no Källén-Lehmann spectral representation for the propagator and the positivity property does not hold, see for example [72, 73].

4.5 Interpretation of spectral functions

As already mentioned, spectral functions encode a multitude of information on, for example, masses, decay widths and decay channels. In this section, we present some simple examples for spectral functions in order to gain an intuitive understanding for their interpretation.

For example, the Euclidean propagator for a free bosonic field is given by

$$D^E(p_0, \vec{p}) = \frac{1}{p_0^2 + \vec{p}^2 + m^2}. \quad (4.46)$$

From this we can immediately derive the corresponding retarded and the advanced propagator by using Eq. (4.26) and Eq. (4.27), which yields

$$D^R(\omega, \vec{p}) = \frac{1}{(\omega + i\epsilon)^2 - \vec{p}^2 - m^2}, \quad (4.47)$$

$$D^A(\omega, \vec{p}) = \frac{1}{(\omega - i\epsilon)^2 - \vec{p}^2 - m^2}. \quad (4.48)$$

The corresponding spectral function can then be obtained by using Eq. (4.14) and reads

$$\rho^{\text{free}}(\omega, \vec{p}) = \text{sgn}(\omega)\delta(\omega^2 - \vec{p}^2 - m^2). \quad (4.49)$$

The spectral function of a free particle is therefore given by a Dirac delta function with all the weight concentrated on the mass shell of the particle, see also Fig. 4.3, where the spectral function for a hypothetical stable pion is shown. One can immediately verify that this spectral function satisfies the sum rule given by Eq. (4.40).

When taking interactions into account, the shape of the spectral function will get modified but the total integrated weight remains constant. For example, when there is a decay channel available at $\omega = m$, then the delta function will turn into a peak with finite height and non-zero width. This situation can be represented by assuming the

4. Analytic continuation and spectral functions

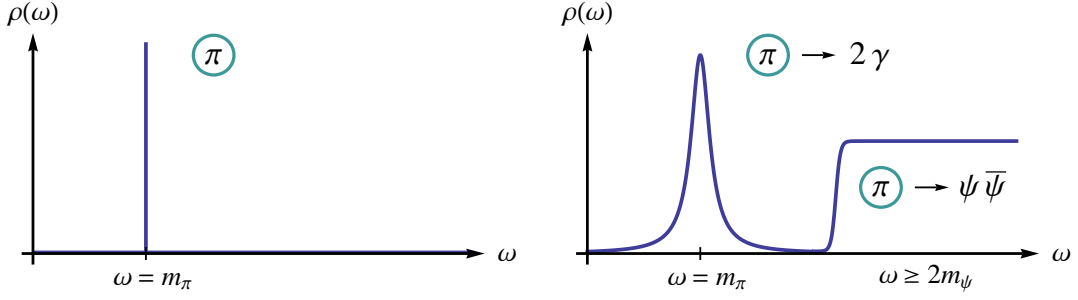


Figure 4.3.: Hypothetical spectral function $\rho(\omega, \vec{p} = 0)$ for a stable pion (left), which is given by a Dirac delta peak at an energy ω equal to the pion mass m_π , and for an unstable pion (right), where the peak assumes a Breit-Wigner shape due to the decay into two photons, and the spectral function exhibits a plateau for energies larger than two times the quarks mass $\omega \geq 2m_\psi$, thus indicating that this decay channel becomes available.

following form of the retarded propagator,

$$D^R(\omega, \vec{p}) = \frac{1}{(\omega + i\gamma)^2 - \vec{p}^2 - m^2 - \Pi^R}, \quad (4.50)$$

where Π^R is the retarded self-energy and $\gamma = \Gamma/2$ the spectral half-width. The spectral function then assumes the following Breit-Wigner form,

$$\rho(\omega, \vec{p}) = \frac{1}{\pi} \frac{2\omega\gamma}{(\omega^2 - \gamma^2 - \vec{p}^2 - m^2 - \Pi^R)^2 + 4\omega^2\gamma^2}, \quad (4.51)$$

where we used Eq. (4.33). Such a spectral function is represented by the right-hand side of Fig. 4.3, where the Breit-Wigner peak is being generated by the decay channel of a pion into two photons. We note that the spectral function is only non-zero due to the discontinuity of the imaginary part of the propagator when crossing the real axis, see also Eq. (4.14).

In addition to decay channels near $\omega = m$, which lead to a broadening of the delta peak, there are usually also decay channels available at higher energies. This situation is also shown in Fig. 4.3, where the threshold for the decay of a pion into a quark-antiquark pair is indicated by an increase of the spectral function at $\omega = 2m_\psi$. This decay channel is therefore available to off-shell pions that have an energy larger than two times the quark mass m_ψ .

5

Relativistic hydrodynamics and Green-Kubo formula for the shear viscosity

In this chapter, we will first introduce ideal relativistic hydrodynamics in Sec. 5.1 and then define the shear viscosity as a coefficient in an expansion of the energy-momentum tensor using viscous relativistic hydrodynamics in Sec. 5.2. The Green-Kubo formalism as well as Green-Kubo relations for various transport coefficients will be presented in Sec. 5.3. In Sec. 5.4, we will apply the Green-Kubo formula for the shear viscosity to the energy-momentum tensor of the quark-meson model in order to derive an equation that allows to calculate the shear viscosity using a momentum dependent spectral function as input.

5.1 Ideal relativistic hydrodynamics

Relativistic hydrodynamics is used to describe the macroscopic behavior of fluid-like systems, see for example [74, 75, 76, 77] for introductions. Within this framework, the evolution of a system is described in terms of local densities and currents, while the microscopic structure is encoded in the equation of state and, for dissipative dynamics, in transport coefficients.

Ideal relativistic hydrodynamics is based on the assumption of local thermodynamic equilibrium, which means that thermodynamic quantities like pressure and temperature are varying slowly within the medium. This also implies that the mean free path of a particle is much smaller than any characteristic dimension of the system. The system can then be characterized by the energy density $\varepsilon(x)$, the pressure $p(x)$, the fluid velocity $\vec{v}(x)$, and a density $\rho_a(x)$ for each conserved charge like, for example, baryon number, electric charge or strangeness. The equations of motion follow from the conservation of

5. Relativistic hydrodynamics and Green-Kubo formula for the shear viscosity

energy and momentum, i.e.

$$\partial_\mu T^{\mu\nu}(x) = 0, \quad (5.1)$$

where $T^{\mu\nu}(x)$ is the contravariant energy-momentum tensor. In particular, T^{00} is the energy density, T^{0j} is the density of the momentum component p^j , T^{i0} is the energy flux along the i -axis, and T^{ij} , also called the pressure tensor, represents the momentum flux of p^j along the i -axis.

In the fluid rest frame, where $\vec{v} = 0$, local thermodynamic equilibrium implies isotropy, which strongly constrains the energy-momentum tensor. In particular, isotropy requires the energy flux T^{i0} and the momentum density T^{0j} to vanish, and the pressure tensor to be $T^{ij} = p\delta_{i,j}$. The ideal energy-momentum tensor in the fluid rest frame is then given by

$$T_{\text{ideal},(0)} = \begin{pmatrix} \varepsilon & 0 & 0 & 0 \\ 0 & p & 0 & 0 \\ 0 & 0 & p & 0 \\ 0 & 0 & 0 & p \end{pmatrix}. \quad (5.2)$$

The energy momentum tensor in a moving frame can be obtained by applying a Lorentz transformation Λ to $T_{\text{ideal},(0)}$, i.e.

$$T_{\text{ideal}}^{\mu\nu} = \Lambda^\mu{}_\alpha \Lambda^\nu{}_\beta T_{\text{ideal},(0)}^{\alpha\beta}. \quad (5.3)$$

To first order in \vec{v} , the Lorentz transformation Λ can be written as

$$\Lambda = \begin{pmatrix} 1 & v_x & v_y & v_z \\ v_x & 1 & 0 & 0 \\ v_y & 0 & 1 & 0 \\ v_z & 0 & 0 & 1 \end{pmatrix}, \quad (5.4)$$

which gives for the ideal energy-momentum tensor in a moving frame

$$T_{\text{ideal}} = \begin{pmatrix} \varepsilon & (\varepsilon + p)v_x & (\varepsilon + p)v_y & (\varepsilon + p)v_z \\ (\varepsilon + p)v_x & p & 0 & 0 \\ (\varepsilon + p)v_y & 0 & p & 0 \\ (\varepsilon + p)v_z & 0 & 0 & p \end{pmatrix}. \quad (5.5)$$

In terms of the four-velocity u^μ , which is defined as

$$u^0 \equiv \frac{1}{\sqrt{1 - \vec{v}^2}}, \quad \vec{u} \equiv \frac{\vec{v}}{\sqrt{1 - \vec{v}^2}}, \quad (5.6)$$

the ideal energy-momentum tensor in a moving frame can also be written as

$$T_{\text{ideal}}^{\mu\nu} = (\varepsilon + p)u^\mu u^\nu - pg^{\mu\nu}, \quad (5.7)$$

5. Relativistic hydrodynamics and Green-Kubo formula for the shear viscosity

where the Minkowski metric tensor is $g^{\mu\nu} \equiv \text{diag}(1, -1, -1, -1)$. We note that taking the derivative of Eq. (5.7) with respect to the four-velocity u^μ yields

$$\frac{\partial}{\partial u^\nu} \partial_\mu T_{\text{ideal}}^{\mu\nu} = \partial_\mu (\varepsilon(x) + p(x)) u^\mu = 0, \quad (5.8)$$

which implies that entropy density is conserved, i.e.

$$\partial_\mu (s u^\mu) \equiv \partial_\mu \left(\frac{\varepsilon(x) + p(x)}{T} u^\mu \right) = 0. \quad (5.9)$$

Together with the conservation of the particle current $j^\mu(x)$,

$$\partial_\mu j^\mu(x) \equiv \partial_\mu (n(x) u^\mu(x)) = 0, \quad (5.10)$$

where $n u^0$ is the particle density and $n \vec{u}$ is the particle flux, Eq. (5.1) and Eq. (5.7) are the defining equations of inviscid, i.e. ideal, relativistic hydrodynamics. This system of equations is then closed by the equation of state, which provides a relation between the pressure p , the energy density ε and the particle number density n .

5.2 Viscous relativistic hydrodynamics and the shear viscosity

In order to describe irreversible processes which involve entropy production and where the mean free path of the particles is not small enough to guarantee an effectively instantaneous local equilibrium, dissipative terms have to be included. We will use the following Navier-Stokes ansatz for the energy-momentum tensor,

$$\begin{aligned} T^{\mu\nu} = & T_{\text{ideal}}^{\mu\nu} + \eta \left(\partial^\mu u^\nu + \partial^\nu u^\mu + u^\nu u^\lambda \partial_\lambda u^\mu + u^\mu u^\lambda \partial_\lambda u^\nu \right) \\ & + \left(\zeta - \frac{2}{3} \eta \right) (g^{\mu\nu} - u^\mu u^\nu) \partial_\lambda u^\lambda, \end{aligned} \quad (5.11)$$

where η is the shear viscosity and ζ is the bulk viscosity, see also [78, 79]. This ansatz corresponds to an expansion of the energy-momentum tensor in terms of powers of four-velocity gradients, which, to lowest order, gives rise to ideal relativistic hydrodynamics. In the local rest frame, where $u^\mu = (1, 0, 0, 0)$, the shear-stress tensor is given by

$$T_{ij}^{(0)} = p \delta_{ij} + \eta \left(\partial_i u_j + \partial_j u_i + \frac{2}{3} \delta_{ij} \partial_k u^k \right) - \zeta \delta_{ij} \partial_k u^k. \quad (5.12)$$

Similarly, the thermal conductivity κ is introduced by adding correction terms to the particle current $j^\mu(x)$, i.e.

$$j^\mu = n u^\mu + \kappa \left(\frac{n T}{\varepsilon + p} \right) \left(\partial^\mu - u^\mu u^\lambda \partial_\lambda \right) \frac{\mu}{T}, \quad (5.13)$$

5. Relativistic hydrodynamics and Green-Kubo formula for the shear viscosity

where μ is the chemical potential. We note that the thermal conductivity is only non-vanishing if there is a conserved four-current j_μ associated with the particle density and the gradient of the chemical potential is non-zero.

In general, the shear viscosity η is a measure for the resistance of a fluid to a deformation due to shear stress. For example, when considering a fluid between two parallel plates that are moving at different velocities, the shear stress $\tau = F/A$ needed to maintain a linear velocity gradient $\partial u/\partial y$ will be proportional to the shear viscosity, i.e.

$$\tau = \eta \frac{\partial u}{\partial y}. \quad (5.14)$$

In order to gain an intuitive understanding of the shear viscosity, we conclude this section by stating a simple expression for η for a classical dilute gas. Using the kinetic theory of gases, one finds

$$\eta = \frac{1}{3} n \bar{p} \lambda = \frac{\bar{p}}{3\sigma}, \quad (5.15)$$

where λ is the mean free path and σ is the cross section. We note that the shear viscosity decreases with increasing interaction. Thus, transport coefficients like the shear viscosity, which characterizes the ability of the gas to transport momentum, will become larger when the gas is more ideal, i.e. more weakly coupled. On the other hand, the shear viscosity of an ideal fluid is zero, cf. Eq. (5.11). This leads to the conclusion that an ideal fluid corresponds to a strongly coupled medium.

5.3 Green-Kubo relations for transport coefficients

Green and Kubo showed that transport coefficients like the electrical conductivity, the heat conductivity and the shear- and bulk viscosity can be expressed in terms of time correlation functions of the corresponding flux [80, 81]. For example, if we consider a general thermodynamic flux J that is linearly proportional to the conjugate thermodynamic force F , i.e.

$$J = L_0 F, \quad (5.16)$$

then L_0 represents a linear transport coefficient. The exact Green-Kubo relation for L_0 is given by

$$L_0 = \frac{V}{T} \int_0^\infty dt \langle J(0) J(t) \rangle_{F=0}, \quad (5.17)$$

where $\langle \cdot \rangle$ denotes the thermal average. In quantum field theory, the Green-Kubo relations are usually expressed in terms of a Fourier-transformed time correlation function, e.g.

$$\rho_L(\omega, \vec{p}) = \int d^4x e^{ipx} \langle [J(x), J(0)] \rangle. \quad (5.18)$$

5. Relativistic hydrodynamics and Green-Kubo formula for the shear viscosity

We will now summarize some important Green-Kubo relations for different transport coefficients. The electrical conductivity σ , for example, defines the linear response of matter to an external electric field \vec{E} via

$$\vec{J} = \sigma(\omega)\vec{E}, \quad (5.19)$$

where \vec{J} is the generated current. The Green-Kubo formula for the frequency-dependent electrical conductivity, also called AC conductivity, is then given by

$$\sigma(\omega) = -\frac{1}{6} \lim_{|\vec{p}| \rightarrow 0} \frac{1}{\omega} \int d^4x e^{ipx} \langle [J^i(x), J_i(0)] \rangle. \quad (5.20)$$

In the limit of a vanishing frequency we obtain the DC conductivity, i.e.

$$\sigma(\omega) = -\frac{1}{6} \lim_{\omega \rightarrow 0} \lim_{|\vec{p}| \rightarrow 0} \frac{1}{\omega} \int d^4x e^{ipx} \langle [J^i(x), J_i(0)] \rangle. \quad (5.21)$$

The Green-Kubo formula for the frequency-dependent shear viscosity $\eta(\omega)$ reads

$$\eta(\omega) = \frac{1}{20} \lim_{|\vec{p}| \rightarrow 0^+} \frac{1}{\omega} \int d^4x e^{ipx} \langle [\pi_{ij}(x), \pi^{ij}(0)] \rangle, \quad (5.22)$$

where π_{ij} is the traceless shear-stress tensor, see also App D. The static shear viscosity is then given by

$$\eta = \frac{1}{20} \lim_{\omega \rightarrow 0^+} \lim_{|\vec{p}| \rightarrow 0^+} \frac{1}{\omega} \int d^4x e^{ipx} \langle [\pi_{ij}(x), \pi^{ij}(0)] \rangle, \quad (5.23)$$

which can also be written as

$$\eta = - \lim_{\omega \rightarrow 0^+} \lim_{|\vec{p}| \rightarrow 0^+} \frac{1}{\omega} \text{Im} \Pi^R(\omega, |\vec{p}|), \quad (5.24)$$

where $\Pi^R(\omega, |\vec{p}|)$ is the retarded correlation function of the shear-stress tensor,

$$\Pi^R(\omega, |\vec{p}|) = -i \int d^4x e^{ipx} \theta(t) \langle [T_{ij}(x), T_{ij}(0)] \rangle, \quad (5.25)$$

where there is no summation implied and $i \neq j$ are off-diagonal spatial indices. A derivation of Eq. (5.23) and Eq. (5.24) based on linear response theory is provided in App. D.

Similarly, one obtains the Green-Kubo relation for the bulk viscosity ζ by focusing on the diagonal part of the energy-momentum tensor,

$$\zeta = \frac{1}{2} \lim_{\omega \rightarrow 0^+} \lim_{|\vec{p}| \rightarrow 0^+} \frac{1}{\omega} \int d^4x e^{ipx} \langle [T_i^i(x), T_j^j(0)] \rangle. \quad (5.26)$$

The bulk viscosity expresses the resistance of a system to a shear-less compression or

5. Relativistic hydrodynamics and Green-Kubo formula for the shear viscosity

expansion. For example, the energy loss of rapidly expanding sound and shock waves due to internal friction can be expressed in terms of the bulk viscosity.

We conclude this section by stating the Green-Kubo equation for the thermal conductivity κ , which is given by

$$\kappa = -\frac{1}{6T} \lim_{\omega \rightarrow 0^+} \lim_{|\vec{p}| \rightarrow 0^+} \frac{1}{\omega} \int d^4x e^{ipx} \langle [\mathcal{T}^i(x), \mathcal{T}_i(0)] \rangle. \quad (5.27)$$

where we defined

$$\mathcal{T}^i \equiv T^{0i} - hN^i, \quad (5.28)$$

with h the enthalpy density and N the particle number. We note that the thermal conductivity is zero if there is no conserved current like N^μ present in the system.

5.4 Application of the Green-Kubo formula for the shear viscosity to the quark-meson model

In this section, we will apply Eq. (5.24) to the quark-meson model in order to derive an expression for the mesonic contributions to the shear viscosity. Obtaining the energy-momentum tensor of the quark-meson model will be straightforward and the thermal average appearing in Eq. (5.24) will be evaluated by using the Matsubara formalism in Euclidean space-time. The retarded correlation function of the shear-stress tensor will then be obtained from its Euclidean counterpart via analytic continuation, i.e.

$$\Pi^R(\omega, \vec{p}) = -\Pi^E(p_0, \vec{p})|_{p_0 = -i(\omega + i\epsilon)}, \quad (5.29)$$

see also Eq. (4.13).

For scalar fields ϕ_a , the energy-momentum tensor is defined as

$$T^{\mu\nu} = \frac{\partial \mathcal{L}}{\partial(\partial_\mu \phi_a)} \partial^\nu \phi_a - g^{\mu\nu} \mathcal{L}. \quad (5.30)$$

When applied to the Lagrange density of the quark-meson model in Minkowski space-time, as given by Eq. (2.27), for $\mu \neq \nu$ we get

$$T^{\mu\nu} = \frac{\partial \mathcal{L}}{\partial(\partial_\mu \psi)} \partial^\nu \psi + \partial^\nu \bar{\psi} \frac{\partial \mathcal{L}}{\partial(\partial_\mu \bar{\psi})} + \frac{\partial \mathcal{L}}{\partial(\partial_\mu \sigma)} \partial^\nu \sigma + \frac{\partial \mathcal{L}}{\partial(\partial_\mu \pi_a)} \partial^\nu \pi_a \quad (5.31)$$

$$= \frac{i}{2} (\bar{\psi} \gamma^\mu \partial^\nu \psi - \partial^\nu \bar{\psi} \gamma^\mu \psi) + \partial^\mu \sigma \partial^\nu \sigma + \partial^\mu \pi_a \partial^\nu \pi_a, \quad (5.32)$$

where we used the symmetrized version of the kinetic quark part, i.e.

$$\frac{i}{2} (\bar{\psi} \gamma^\mu (\partial_\mu \psi) - (\partial_\mu \bar{\psi}) \gamma^\mu \psi). \quad (5.33)$$

5. Relativistic hydrodynamics and Green-Kubo formula for the shear viscosity

We will now focus on one of the off-diagonal spatial bosonic terms, i.e. with $i \neq j$, and use

$$T^{ij} = \partial^i \phi \partial^j \phi \quad (5.34)$$

in order to calculate the Euclidean correlator of the energy momentum tensor, $\Pi^E(x)$. In analogy to the usual field correlators, it is given by

$$\Pi^E(x) = \langle T_{ij}(x) T_{ij}(0) \rangle, \quad (5.35)$$

where we suppress the time-ordering operator. Inserting Eq. (5.34) into Eq. (5.35) yields

$$\Pi^E(x) = \langle \partial_i \phi(x) \partial_j \phi(x) \partial_i \phi(0) \partial_j \phi(0) \rangle \quad (5.36)$$

$$= 2 \langle \partial_i \phi(x) \partial_i \phi(0) \rangle \langle \partial_j \phi(x) \partial_j \phi(0) \rangle, \quad (5.37)$$

where we neglected the connected contributions to the four-point function and where the factor 2 arises from forming all possible contractions that lead to full propagators, see also [82]. Switching to momentum space by using Eq. (A.8) and

$$\Pi^E(p) = \int d^4x e^{ipx} \Pi^E(x), \quad (5.38)$$

gives for the Euclidean correlation function of the energy-momentum tensor

$$\begin{aligned} \Pi^E(p) = 2 \int d^4x e^{ipx} & \left\langle \int \frac{d^4p'}{(2\pi)^4} i p'_i \phi(p') e^{ip'x} \int \frac{d^4p''}{(2\pi)^4} i p''_i \phi(p'') \right\rangle \\ & \times \left\langle \int \frac{d^4p'''}{(2\pi)^4} i p'''_j \phi(p''') e^{ip'''x} \int \frac{d^4p''''}{(2\pi)^4} i p''''_j \phi(p''''') \right\rangle. \end{aligned} \quad (5.39)$$

This expression can be simplified by using

$$\int d^4x e^{i(p+p'+p''')x} = (2\pi)^4 \delta^{(4)}(p+p'+p'''), \quad (5.40)$$

which yields

$$\begin{aligned} \Pi^E(p) = 2 & \left\langle \int \frac{d^4p'}{(2\pi)^4} p'_i \phi(p') \int \frac{d^4p''}{(2\pi)^4} p''_i \phi(p'') \right\rangle \\ & \times \left\langle (-p_j - p'_j) \phi(-p - p') \int \frac{d^4p''''}{(2\pi)^4} p''''_j \phi(p''''') \right\rangle. \end{aligned} \quad (5.41)$$

A further simplification can be achieved by expressing Eq. (5.41) in terms of the Euclidean propagator,

$$D^E(p) = \langle \phi(p) \phi(-p) \rangle. \quad (5.42)$$

5. Relativistic hydrodynamics and Green-Kubo formula for the shear viscosity

Therefore, we use

$$\langle \phi(p)\phi(p') \rangle = D^E(p)(2\pi)^4 \delta^{(4)}(p+p'), \quad (5.43)$$

and get

$$\begin{aligned} \Pi^E(p) = 2 \int \frac{d^4 p'}{(2\pi)^4} \int \frac{d^4 p''}{(2\pi)^4} \int \frac{d^4 p'''}{(2\pi)^4} p'_i p''_i D^E(p') (2\pi)^4 \delta^{(4)}(p'+p'') (-p_j - p'_j) \\ \times p_j''' D^E(p+p') (2\pi)^4 \delta^{(4)}(-p-p'+p'''). \end{aligned} \quad (5.44)$$

Evaluating the Dirac delta functions then gives

$$\Pi^E(p) = 2 \int \frac{d^4 p'}{(2\pi)^4} p_i'^2 (p_j + p'_j)^2 D^E(p') D^E(p+p'). \quad (5.45)$$

Performing a shift in one of the integration variables, i.e. $p'_j \rightarrow p'_j - p_j$, gives for the Euclidean correlation function of the energy-momentum tensor

$$\Pi^E(p) = 2 \int \frac{d^4 q}{(2\pi)^4} q_i^2 q_j^2 D^E(q) D^E(q+p). \quad (5.46)$$

Diagrammatically, this corresponds to a closed loop with an external momentum p going through one of the full propagators, cf. Fig. 5.1.

At finite temperature, the integration over energy in Eq. (5.46) turns into a summation over Matsubara modes, i.e.

$$\Pi^E(p_0, \vec{p}) = 2T \sum_{q_0} \int \frac{d^3 q}{(2\pi)^3} q_x^2 q_y^2 D(iq_0, \vec{q}) D(iq_0 + ip_0, \vec{q} + \vec{p}), \quad (5.47)$$

where we sum over the internal Matsubara frequencies, which are given by $q_0 = 2n\pi T$ with $n \in \mathbb{Z}$. We now rewrite the Matsubara sum as a contour integral, where the two

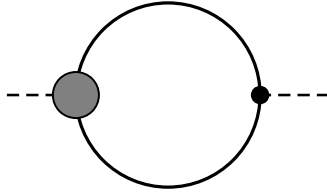


Figure 5.1.: Diagrammatic expression for the correlation function of the energy-momentum tensor as necessary for the calculation of the shear viscosity, cf. Eq. (5.24) and Eq. (5.46). Solid lines denote full propagators, the left circle denotes a dressed vertex and the right circle represents a bare vertex. In our implementation, however, both vertices are taken as bare.

5. Relativistic hydrodynamics and Green-Kubo formula for the shear viscosity

Matsubara frequencies that produce a propagator with argument zero, $D(0)$, are treated separately since the propagators can, in general, exhibit branch cuts along the real axis, cf. [31, 78]. Then we have

$$\begin{aligned} \Pi^E(p_0, \vec{p}) = 2 \int \frac{d^3q}{(2\pi)^3} q_x^2 q_y^2 & \left(TD(0, \vec{q})D(ip_0, \vec{q} + \vec{p}) + TD(-ip_0, \vec{q})D(0, \vec{q} + \vec{p}) \right. \\ & \left. + \oint_C \frac{dz}{2\pi i} n_B(z)D(z, \vec{q})D(z + ip_0, \vec{q} + \vec{p}) \right), \end{aligned} \quad (5.48)$$

where the contour C excludes the two extracted Matsubara modes and is represented by Fig. 5.2.

We now treat the contribution from the two Matsubara modes and the contribution from the contour integral separately and introduce the following short-hand notation,

$$A^E \equiv TD(0, \vec{q})D(ip_0, \vec{q} + \vec{p}) + TD(-ip_0, \vec{q})D(0, \vec{q} + \vec{p}), \quad (5.49)$$

$$B^E \equiv \oint_C \frac{dz}{2\pi i} n_B(z)D(z, \vec{q})D(z + ip_0, \vec{q} + \vec{p}). \quad (5.50)$$

Starting with A^E , we can immediately perform the analytic continuation by replacing the imaginary Matsubara frequencies by a continuous real energy in order to get the corresponding retarded expression,

$$A^R = -A^E(ip_0 \rightarrow \omega + i\epsilon), \quad (5.51)$$

cf. Eq. (4.13), which gives

$$A^R = -(TD(0, \vec{q})D(\omega + i\epsilon, \vec{q} + \vec{p}) + TD(-\omega - i\epsilon, \vec{q})D(0, \vec{q} + \vec{p})). \quad (5.52)$$

Taking the following symmetry property of the propagator into account, cf. Eq. (4.36),

$$D^A(-\omega, \vec{p}) \equiv D(-\omega - i\epsilon, \vec{p}) = D(\omega + i\epsilon, \vec{p}) \equiv D^R(\omega, \vec{p}), \quad (5.53)$$

yields the following expression for the imaginary part of A^R in the limit $\vec{p} \rightarrow 0$, cf. Eq. (D.31),

$$\lim_{|\vec{p}| \rightarrow 0^+} \text{Im} A^R = -2T \text{Re} D(0, \vec{q}) \text{Im} D^R(\omega, \vec{q}). \quad (5.54)$$

The imaginary part of the retarded propagator can be expressed in terms of the spectral function,

$$\text{Im} D^R(\omega, \vec{p}) = -\pi\rho(\omega, \vec{p}), \quad (5.55)$$

cf. Eq. (4.33), which gives

$$\lim_{|\vec{p}| \rightarrow 0^+} \text{Im} A^R = -2T \text{Re} D^R(0, \vec{q}) (-\pi\rho(\omega, \vec{q})) \quad (5.56)$$

$$= 2\pi T \text{Re} D^R(0, \vec{q})\rho(\omega, \vec{q}). \quad (5.57)$$

5. Relativistic hydrodynamics and Green-Kubo formula for the shear viscosity

By taking the derivative with respect to ω and taking the limit $\omega \rightarrow 0$, cf. Eq. (5.24), we get

$$\lim_{\omega \rightarrow 0^+} \lim_{|\vec{p}| \rightarrow 0^+} \frac{d}{d\omega} \text{Im} A^R = 2\pi T \text{Re} D(0, \vec{q}) \rho'(0, \vec{q}). \quad (5.58)$$

We now turn to part B^E , as defined by Eq. (5.50), and deform the contour as shown in Fig. 5.2. The contour reduces to integrations along horizontal lines with $\text{Im} z = 0$ and $i \text{Im} z = -i p_0$. Taking the limit $\vec{p} \rightarrow 0$ then yields

$$\begin{aligned} \lim_{|\vec{p}| \rightarrow 0^+} B^E = \int_{-\infty}^{\infty} \frac{dq_0}{2\pi i} & \left(+ n_B(q_0 + i\epsilon) D(q_0 + i\epsilon, \vec{q}) D(q_0 + ip_0 + i\epsilon, \vec{q}) \right. \\ & - n_B(q_0 - i\epsilon) D(q_0 - i\epsilon, \vec{q}) D(q_0 + ip_0 - i\epsilon, \vec{q}) \\ & + n_B(q_0 - ip_0 + i\epsilon) D(q_0 - ip_0 + i\epsilon, \vec{q}) D(q_0 + i\epsilon, \vec{q}) \\ & \left. - n_B(q_0 - ip_0 - i\epsilon) D(q_0 - ip_0 - i\epsilon, \vec{q}) D(q_0 - i\epsilon, \vec{q}) \right). \end{aligned} \quad (5.59)$$

Using the continuity of the bosonic occupation number, n_B , along the real axis and its periodicity along the imaginary axis gives

$$\begin{aligned} \lim_{|\vec{p}| \rightarrow 0^+} B^E = \int_{-\infty}^{\infty} \frac{dq_0}{2\pi i} & \left(+ n_B(q_0) D(q_0 + i\epsilon, \vec{q}) D(q_0 + ip_0, \vec{q}) \right. \\ & - n_B(q_0) D(q_0 - i\epsilon, \vec{q}) D(q_0 + ip_0, \vec{q}) \\ & + n_B(q_0) D(q_0 - ip_0, \vec{q}) D(q_0 + i\epsilon, \vec{q}) \\ & \left. - n_B(q_0) D(q_0 - ip_0, \vec{q}) D(q_0 - i\epsilon, \vec{q}) \right), \end{aligned} \quad (5.60)$$

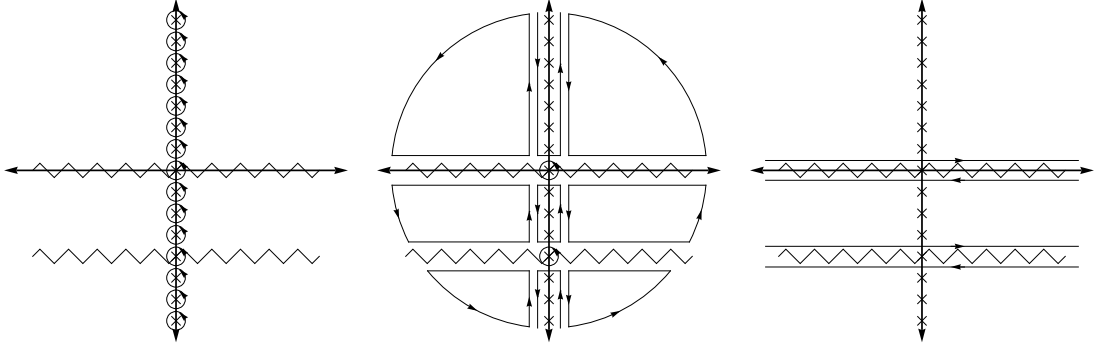


Figure 5.2.: The summation over Matsubara modes in Eq. (5.47) is represented by the left figure. This summation can be replaced by a contour integration (center), where we added additional contours that contain no poles in the complex plane and therefore give no contribution to the integration. All these contours can be combined to give the contour shown by the right figure. Possible branch cuts are denoted by zig-zag lines.

5. Relativistic hydrodynamics and Green-Kubo formula for the shear viscosity

where we dropped the small imaginary part $i\epsilon$ wherever possible. Writing this in terms of advanced and retarded propagators gives

$$\lim_{|\vec{p}| \rightarrow 0^+} B^E = \int_{-\infty}^{\infty} \frac{dq_0}{2\pi i} n_B(q_0) \left(D(q_0 + ip_0, \vec{q}) (D^R(q_0, \vec{q}) - D^A(q_0, \vec{q})) \right. \\ \left. + D(q_0 - ip_0, \vec{q}) (D^R(q_0, \vec{q}) - D^A(q_0, \vec{q})) \right). \quad (5.61)$$

We now use the following relation between the retarded and the advanced propagator,

$$i(D^R - D^A) = -2 \operatorname{Im} D^R, \quad (5.62)$$

$$D^R - D^A = 2i \operatorname{Im} D^R, \quad (5.63)$$

cf. Eq. (4.36), and get

$$\lim_{|\vec{p}| \rightarrow 0^+} B^E = \int_{-\infty}^{\infty} \frac{dq_0}{2\pi i} n_B(q_0) \left(D(q_0 + ip_0, \vec{q}) 2i \operatorname{Im} D^R(q_0, \vec{q}) + D(q_0 - ip_0, \vec{q}) 2i \operatorname{Im} D^R(q_0, \vec{q}) \right) \quad (5.64)$$

$$= \int_{-\infty}^{\infty} \frac{dq_0}{\pi} n_B(q_0) \left(D(q_0 + ip_0, \vec{q}) \operatorname{Im} D^R(q_0, \vec{q}) + D(q_0 - ip_0, \vec{q}) \operatorname{Im} D^R(q_0, \vec{q}) \right). \quad (5.65)$$

Performing the analytic continuation,

$$B^R = -B^E(ip_0 \rightarrow \omega + i\epsilon), \quad (5.66)$$

yields the corresponding retarded expression, i.e.

$$\lim_{|\vec{p}| \rightarrow 0^+} B^R = - \int_{-\infty}^{\infty} \frac{dq_0}{\pi} n_B(q_0) \left(D(q_0 + \omega + i\epsilon, \vec{q}) \operatorname{Im} D^R(q_0, \vec{q}) \right. \\ \left. + D(q_0 - \omega - i\epsilon, \vec{q}) \operatorname{Im} D^R(q_0, \vec{q}) \right). \quad (5.67)$$

We now shift the integration variable in the second part of Eq. (5.67), i.e. $q_0 \rightarrow q_0 + \omega$, which gives

$$\lim_{|\vec{p}| \rightarrow 0^+} B^R = - \int_{-\infty}^{\infty} \frac{dq_0}{\pi} \left(n_B(q_0) D^R(q_0 + \omega, \vec{q}) \operatorname{Im} D^R(q_0, \vec{q}) \right. \\ \left. + n_B(q_0 + \omega) D^A(q_0, \vec{q}) \operatorname{Im} D^R(q_0 + \omega, \vec{q}) \right). \quad (5.68)$$

Using

$$\operatorname{Im} D^A(q_0, \vec{q}) = -\operatorname{Im} D^R(q_0, \vec{q}) \quad (5.69)$$

and expressing the retarded propagators in terms of the spectral function, cf. Eq. (5.55),

5. Relativistic hydrodynamics and Green-Kubo formula for the shear viscosity

then yields for the imaginary part of B^R

$$\lim_{|\vec{p}| \rightarrow 0^+} \text{Im } B^R = - \int_{-\infty}^{\infty} \frac{dq_0}{\pi} \left(n_B(q_0) \text{Im } D^R(q_0 + \omega, \vec{q}) \text{Im } D^R(q_0, \vec{q}) \right. \\ \left. - n_B(q_0 + \omega) \text{Im } D^R(q_0, \vec{q}) \text{Im } D^R(q_0 + \omega, \vec{q}) \right) \quad (5.70)$$

$$= - \int_{-\infty}^{\infty} \frac{dq_0}{\pi} \left(n_B(q_0) (-\pi \rho(q_0 + \omega, \vec{q})) (-\pi \rho(q_0, \vec{q})) \right. \\ \left. - n_B(q_0 + \omega) (-\pi \rho(q_0, \vec{q})) (-\pi \rho(q_0 + \omega, \vec{q})) \right) \quad (5.71)$$

$$= -\pi \int_{-\infty}^{\infty} dq_0 \left(n_B(q_0) \rho(q_0 + \omega, \vec{q}) \rho(q_0, \vec{q}) \right. \\ \left. - n_B(q_0 + \omega) \rho(q_0, \vec{q}) \rho(q_0 + \omega, \vec{q}) \right) \quad (5.72)$$

$$= -\pi \int_{-\infty}^{\infty} dq_0 (n_B(q_0) - n_B(q_0 + \omega)) \rho(q_0 + \omega, \vec{q}) \rho(q_0, \vec{q}). \quad (5.73)$$

Taking the derivative with respect to ω and letting $\omega \rightarrow 0$ gives

$$\lim_{\omega \rightarrow 0^+} \lim_{|\vec{p}| \rightarrow 0^+} \frac{d}{d\omega} \text{Im } B^R = \pi \int_{-\infty}^{\infty} dq_0 n'_B(q_0) \rho^2(q_0, \vec{q}). \quad (5.74)$$

Finally, we combine the results for part *A* and *B*, given by Eq. (5.58) and Eq. (5.74), and get for the shear viscosity

$$\eta = - \lim_{\omega \rightarrow 0^+} \lim_{|\vec{p}| \rightarrow 0^+} \frac{d}{d\omega} \text{Im } \Pi^R(\omega) \quad (5.75)$$

$$= 2 \int \frac{d^3 q}{(2\pi)^3} q_x^2 q_y^2 \left(-2\pi T \text{Re } D^R(0, \vec{q}) \rho'(0, \vec{q}) - \pi \int_{-\infty}^{\infty} dq_0 n'_B(q_0) \rho^2(q_0, \vec{q}) \right). \quad (5.76)$$

We now rename $q \rightarrow p$ and switch to spherical coordinates, which reduces the three-dimensional integration over the spatial loop momentum to a one-dimensional integration over $p_r \equiv |\vec{p}|$. The static shear viscosity is then given by

$$\eta = -\frac{1}{15\pi} \int_0^{\infty} dp_r \left(p_r^6 T \text{Re } D^R(0, p_r) \rho'(0, p_r) + \int_0^{\infty} d\omega p_r^6 n'_B(\omega) \rho^2(\omega, p_r) \right). \quad (5.77)$$

This expression allows to calculate the shear viscosity using only the momentum dependent spectral function as input, since the real part of the retarded propagator appearing in Eq. (5.77) can also be obtained from the spectral function via the corresponding Källén-Lehmann spectral representation, cf. Eq. (4.22). The numerical implementation of Eq. (5.77) will be discussed in Sec. 6.3.

6

Numerical implementation

We will now discuss details on our numerical implementation used to obtain the results presented in the following. In particular, the flow equation for the effective potential is solved using the grid method, which is described in Sec. 6.1. Information on the scale-dependent effective potential is then used to solve the flow equations for the retarded two-point functions, as discussed in Sec. 6.2. Finally, details on the numerical calculation of the shear viscosity are presented in Sec. 6.3.

6.1 Solving the flow equation for the effective potential

The flow equation for the effective potential $U_k(\phi^2)$, given by Eq. (3.9), represents an infinite set of coupled ordinary differential equations and cannot be solved analytically. There are, however, several numerical methods available in the literature to deal with equations of this type. One possibility is to perform a Taylor expansion of the effective potential about a scale-dependent expansion point. Truncating such a Taylor expansion at some finite order then reduces the flow equation for the effective potential to a finite set of flow equations for the expansion parameters. More recently, also a Taylor expansion using a scale-independent expansion point was proposed [61]. In general, such Taylor methods are numerically cheap and well suited to calculate, for example, critical exponents to high accuracy. On the other hand, the correct description of first-order phase transitions is often difficult.

We will therefore use a so-called grid method in this thesis to solve the flow equation for the effective potential, cf. [26]. This method is based on discretizing the field variable ϕ^2 and allows access to the full field-dependence of the effective potential. The grid method is therefore well suited to describe also first order phase transitions. In particular, we will discretize the invariant field ϕ^2 along a one-dimensional grid which reduces the

6. Numerical implementation

Λ	m_Λ/Λ	λ_Λ	c/Λ^3	h	$\sigma_0 \equiv f_\pi$	m_π	m_σ	m_ψ
1 GeV	0.794	2.00	0.00175	3.2	93.5 MeV	138 MeV	509 MeV	299 MeV

Table 6.1.: Parameter set used for the quark-meson model and values for observables obtained in the vacuum at an IR scale of $k_{\text{IR}} = 40$ MeV.

flow equation for the effective potential $U_k(\phi^2)$, Eq. (3.9), to a finite set of flow equations for $U_k(\phi_i^2)$ at the grid points ϕ_i^2 . Higher field-derivatives of $U_k(\phi^2)$ are then obtained by using the method of finite differences.

At the UV scale Λ we choose the effective potential to be of the form

$$U_\Lambda(\phi^2) = \frac{1}{2}m_\Lambda^2\phi^2 + \frac{1}{4}\lambda_\Lambda(\phi^2)^2, \quad (6.1)$$

where explicit values for the parameters m_Λ and λ_Λ are given by Tab. 6.1. These values have been chosen such as to reproduce realistic values for the pion decay constant and the effective particle masses in the IR. For the UV cutoff we choose a value of $\Lambda = 1$ GeV, which is an energy scale below which the quark-meson model is expected to provide for an effective description of the chiral aspects of QCD with two flavors, while at higher energies quarks and, in particular, gluons become the relevant degrees of freedom.

In principle, the flow equations for the effective potential at the grid points ϕ_i^2 then have to be integrated down to a scale of $k = 0$. For numerical reasons, however, the flow has to be stopped at some finite IR scale, cf. [26]. In the following, we choose this IR scale to be $k_{\text{IR}} = 40$ MeV, cf. also Tab. 6.1. Stopping the flow of the effective potential at this finite scale does, however, not impair the validity of our results since the minimum of the potential as well as the values of observables like the effective particle masses are basically fixed as soon as the lightest degree of freedom decouples from the flow. In most cases, this will be the pion with a vacuum mass of $m_\pi \approx 138$ MeV, which is considerably larger than k_{IR} . The main effect of the fluctuations included at lower scales is then to turn the potential convex.

After solving the flow equation for the effective potential, the explicit symmetry breaking term $c\sigma$ is added in the IR, cf. Sec. 3.2, and observables like the pion decay constant and the effective particle masses are determined, cf. Tab. 6.1. We can also estimate the quark condensate by using the operator product expansion (OPE) of the quark propagator together with

$$\langle \bar{\psi}\psi \rangle = -N_c \int_\Lambda \frac{d^4q}{(2\pi)^4} \text{Tr} \left(S(q) - S_0(q) \right), \quad (6.2)$$

where the quark propagator $S(q)$ is associated to an infrared constituent mass m_ψ and $S_0(q)$ is the quark propagator at the UV cutoff Λ , with explicit current mass $m_{\psi,c}$, cf. also [83]. From Eq. (6.2) we then obtain the estimate

$$\langle \bar{\psi}\psi \rangle = -\frac{N_c}{4\pi^2} \left[m_\psi \Lambda^2 + m_\psi^3 \ln \left(\frac{m_\psi^2}{\Lambda^2 + m_\psi^2} \right) - m_{\psi,c} \Lambda^2 + m_{\psi,c}^3 \ln \left(\frac{m_{\psi,c}^2}{\Lambda^2 + m_{\psi,c}^2} \right) \right]. \quad (6.3)$$

6. Numerical implementation

Using the parameters from Tab. 6.1 we find a value of $\sigma_{0,\Lambda} = 2.78$ MeV for the location of the global minimum of the explicitly broken effective potential at the UV scale, which corresponds to a current quark mass of $m_{\psi,c} = h\sigma_{0,\Lambda} = 8.86$ MeV. Inserting this into Eq. (6.3) gives the following estimate for the quark condensate in the vacuum,

$$\langle \bar{\psi}\psi \rangle \approx -(257 \text{ MeV})^3, \quad (6.4)$$

in very good agreement with QCD sum rules. This result can be compared to the GOR relation, cf. Eq. (2.16), which yields

$$-m_{\psi,c}\langle \bar{\psi}\psi \rangle = f_\pi^2 m_\pi^2 \approx (114 \text{ MeV})^4, \quad (6.5)$$

which is in good agreement with our result since Eq. (6.4) gives

$$-m_{\psi,c}\langle \bar{\psi}\psi \rangle \approx (111 \text{ MeV})^4. \quad (6.6)$$

6.2 Solving the flow equations for the two-point functions and MPI parallelization

Once the flow equation for the effective potential has been solved, we have access to the scale-dependent effective potential and its derivatives at the grid points. This information is then used to solve to flow equations for the retarded 2-point functions, cf. Eqs. (3.23)-(3.24). In principle, these flow equations are also solved on a grid in field space. Since the flow equations for the two point functions at a given grid point do not depend on information on the two-point functions from other grid points, it suffices to use only one grid point, namely the grid point corresponding to the global minimum of the effective potential in the IR.

As for the effective potential, we have to provide initial values for the retarded two-point functions at the UV scale. By taking two functional derivatives of the effective action, cf. Eq. (3.8), we get

$$\Gamma_{\Lambda,\sigma}^{(2),R}(\omega, \vec{p}) = (\omega + i\epsilon)^2 - \vec{p}^2 - 2U'_\Lambda - 4\phi^2 U''_\Lambda, \quad (6.7)$$

$$\Gamma_{\Lambda,\pi}^{(2),R}(\omega, \vec{p}) = (\omega + i\epsilon)^2 - \vec{p}^2 - 2U'_\Lambda, \quad (6.8)$$

where we use $\epsilon = 0.1$ in most of our numerical calculations.

We note that there are some difficulties that can occur when solving the flow equations for the retarded two-point functions. There are, for example, cutoff effects that are generated by the “abrupt” start and end of the integration of the flow equations. These cutoff effects produce unphysical values of the two-point functions at energies ω that correspond to the UV and IR values of the effective particle energies obtained from Eqs. (3.10)-(3.12). Since these energies are approximately proportional to the scale k , the UV cutoff effects are located at very high energies and usually do not affect our calculations. The IR cutoff effects, on the other hand, manifest themselves at lower energies and, although being a lot smaller than the UV cutoff effects, should be corrected.

6. Numerical implementation

Therefore, we use an extrapolation of the required derivatives of the effective potential $U_k^{(i)}$ below k_{IR} in order to integrate the flow equations for the two-point functions down to $k = 0$. In this way, the IR cutoff effects can be removed completely. The same procedure can also be used to remove the UV cutoff effects, or rather, to shift them to ever higher energies, which is, however, not done in the following.

Another difficulty arises from the fact that the flow equations for the two-point functions are highly sensitive to the scale dependence of the energies E_k , as given by Eqs. (3.10)-(3.12). Near the critical endpoint, for example, the sigma mass undergoes drastic changes within a small k range, which hampers the calculation of two-point functions, and consequently spectral functions. These effects can be attenuated by using a larger value for ϵ , cf. the discussion in App. E.2. A similar effect arises at finite temperature, $T > 50$ MeV, where contributions from thermal processes, in particular from the process of two pions going into a sigma meson, can produce unphysical values of the two-point functions and the spectral functions at energies where these processes are relevant. Where necessary, we therefore use a quadratic fit for the scale-dependent energies E_k in order to eliminate numerical fluctuations and to provide a smooth shape for the scale-dependence of the energies. We checked that this method leaves the two-point functions and spectral functions basically unchanged at energies where the thermal processes cannot occur.

We also note that the use of dimensionally reduced regulator functions, cf. Eqs. (3.2)-(3.3), gives rise to a slight breaking of Lorentz or $O(4)$ invariance. This effect can be remedied to a large extent by adding an ω -independent constant to the real part of the two-point function, as discussed in detail in App. E.1. This procedure has been used to obtain the 3D plots of the momentum dependence of the spectral functions, see App. F, which serve as a basis for the calculation of the shear viscosity, cf. Ch. 5.

Especially for finite values of the spatial momentum \vec{p} , the numerical evaluation of the flow equations for the retarded two-point functions is very time-consuming. Therefore, we use the MPI (Message Passing Interface) framework in order to solve these equations in a parallelized manner on high-performance computers. This parallelization is implemented as follows.

First, all k -dependent quantities needed for the evaluation of the flow equation for the two-point functions are stored as continuous functions of the scale k by means of interpolations. In particular, the first, second, third and fourth derivative of the scale-dependent effective potential $U_k(\phi^2)$ have to be known at the global IR minimum σ_0 . The integration of the flow equation for the two-point functions can then be split into small parts, such that a single CPU core only integrates a small k -range, usually chosen to be $\Delta k = 1$ MeV. Once a “worker” core finishes such an integration over Δk , it sends the result back to the “master” core and is assigned the next k -range to integrate. When interested in the two-point function at different energies ω and spatial momenta \vec{p} , or at different temperatures T and chemical potentials μ , such a parallelized integration over k can be supplemented with additional global loops associated to these parameters.

Our calculations were carried out on the Lichtenberg high performance computer in Darmstadt and the LOEWE CSC in Frankfurt, typically using 256 CPU cores in parallel.

6. Numerical implementation

In total, approximately ten million CPU core hours were needed to produce the results presented in this thesis.

6.3 Calculating the shear viscosity

The shear viscosity can be calculated by using the momentum dependent spectral functions as input, see Eq. (5.77). This equation is difficult to handle numerically since the derivative of the bosonic occupation number diverges at $\omega = 0$. Therefore, we make use of the following series expansion for $\omega < 1$ MeV,

$$n_B(\omega) = \frac{1}{\exp(\omega/T) - 1}, \quad (6.9)$$

$$n'_B(\omega) = \frac{-\exp(\omega/T)}{(\exp(\omega/T) - 1)^2 T}, \quad (6.10)$$

$$n'_B(\omega) = -\frac{T}{\omega^2} + \frac{1}{12T} - \frac{\omega^2}{240T^3} + \mathcal{O}(\omega^3). \quad (6.11)$$

Together with the following Ansatz for the spectral function at small ω ,

$$\rho(\omega, p_r) = a(p_r)\omega + b(p_r)\omega^2 + \mathcal{O}(\omega^3), \quad (6.12)$$

which has been checked to describe the spectral functions well for $\omega < 1$ MeV, we find

$$n'_B(\omega)\rho^2(\omega, p_r) \approx -\frac{T}{\omega^2}a^2(p_r)\omega^2 = -Ta^2(p_r) = -T\rho'(0, p_r)^2. \quad (6.13)$$

Using this result for $\omega < 1$ MeV in Eq. (5.77) yields the following equation for the shear viscosity,

$$\eta = -\frac{1}{15\pi} \int_0^\infty dp_r \left(\int_1^\infty d\omega p_r^6 n'_B(\omega)\rho^2(\omega, p_r) - p_r^6 T \rho'(0, p_r)^2 + p_r^6 T \text{Re} D^R(0, p_r)\rho'(0, p_r) \right). \quad (6.14)$$

Still, this expression is not well suited for a numerical treatment since the integration ranges up to arbitrarily high energies and momenta. In our numerical implementation, we therefore use finite values for the upper integration bounds in Eq. (6.14). In particular, the energy ω is integrated up to $\Lambda = 1$ GeV, while the integration over spatial momentum ranges up to 5Λ . For large spatial momenta, i.e. $p_r \geq \Lambda$, we use an exponentially decreasing function of the form

$$\rho(\omega, p_r) = a_0 e^{-a_1(p_r - a_2)} \quad (6.15)$$

to obtain the corresponding values for the spectral function. This form for the extrapolation functions has been checked to agree well with the observed high momentum behavior of the spectral functions.

Due to the cutoff applied for the ω -integration, the spectral functions will not be

6. Numerical implementation

correctly normalized, cf. Eq. (4.40) and the discussion in App. E.3. Therefore, the spectral functions are normalized by hand such that the following modified sum rule holds for $\vec{p} = 0$,

$$\int_0^\Lambda d\omega 2\omega \rho(\omega, \vec{p}) = 1. \quad (6.16)$$

The final equation for the shear viscosity, which is used in our numerical implementation, then reads

$$\eta = -\frac{1}{15\pi} \int_0^{5\Lambda} dp_r \left(\int_1^\Lambda d\omega p_r^6 n'_B(\omega) \rho^2(\omega, p_r) - p_r^6 T \rho'(0, p_r)^2 + \frac{p_r^6 T \rho'(0, p_r)}{\text{Re } \Gamma^{(2),R}(0, p_r)} \right), \quad (6.17)$$

where we expressed the retarded propagator D^R in terms of the retarded two-point function $\Gamma^{(2),R}$, and where the derivative of the spectral function, $\rho'(0, p_r)$, is obtained by using finite differences.

Part II.
Results

7

Phase diagram and thermodynamics

In this chapter, which is based on [29], we will first discuss the phase diagram of the quark-meson model as obtained by representing the chiral order parameter in the T - μ -plane, cf. Sec. 7.1. The temperature and chemical potential-dependence of the different quasi-particle masses is then studied in Sec. 7.2, where we focus on two lines in the phase diagram, i.e. the line of vanishing chemical potential and the constant-temperature line that crosses the critical endpoint. Moreover, we will study the temperature dependence of the entropy density in Sec. 7.2, which will be used in Ch. 10 to calculate the shear viscosity to entropy density ratio. We note that we use the parameter set given by Tab. 6.1 throughout the following chapters.

7.1 The phase diagram of the quark-meson model

The phase diagram of the quark meson-model is shown in Fig. 7.1. It has been obtained by solving the flow equation for the effective potential, Eq. (3.9), without the high temperature corrections discussed in Sec. 3.2, and using the global minimum $\sigma_0(T, \mu)$ of the effective potential in the IR as an order parameter for chiral symmetry.

The phase diagram displays the same structure as found in previous studies that go beyond the mean-field approximation, see for example [26]. In particular, it exhibits a regime at low temperatures and small chemical potentials where $\sigma_0(T, \mu)$ is close to its vacuum value and where hence chiral symmetry is spontaneously as well as explicitly broken. At high temperatures and large chemical potentials, on the other hand, we observe a progressing restoration of chiral symmetry, indicated by smaller values of $\sigma_0(T, \mu)$. These two regimes are separated by a first order phase transition at small temperatures which turns into a critical endpoint at $T \approx 10$ MeV and $\mu \approx 293$ MeV, cf. Fig. 7.1. At higher temperatures the phase transition is lost and a crossover is observed.

7. Phase diagram and thermodynamics

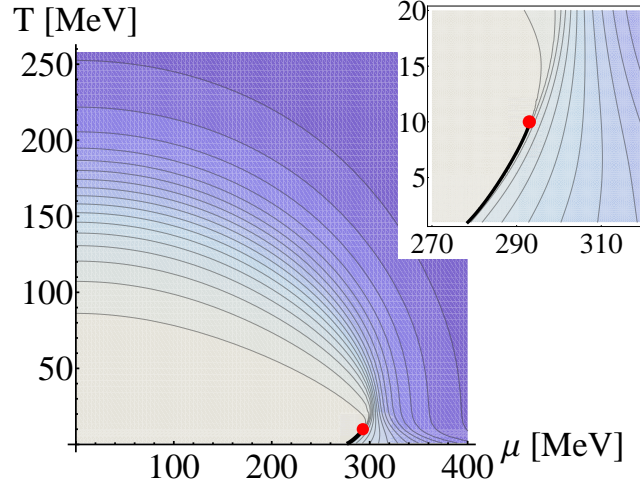


Figure 7.1.: The phase diagram of the quark-meson model is represented by a contour plot of the chiral order parameter $\sigma_0(T, \mu)$ vs. quark chemical potential μ and temperature T . The order parameter decreases towards higher μ and T , indicated by darker color. The critical endpoint is denoted by a red dot, which is connected to the black first-order transition line. Taken from [29].

When discussing results on spectral functions and other observables in the following, we will always focus on their temperature dependence at $\mu = 0$ and their chemical potential dependence at a constant temperature of $T = 10$ MeV. This corresponds to two lines in the phase diagram, namely to the temperature axis and to a horizontal line that crosses the critical endpoint.

7.2 Quasi-particle masses and entropy density

We will now study the temperature- and chemical potential-dependence of the effective particle masses and the order parameter, cf. Fig. 7.2, where the sigma mass m_σ and the pion mass m_π represent the curvature masses, since they are extracted from the shape of the effective potential at the global minimum σ_0 in the IR, cf. Eqs. (3.10)-(3.11), while the quark mass m_ψ is given by Eq. (3.12) and proportional to σ_0 . Since these masses serve as input for the calculation of spectral functions and determine, for example, the location of decay thresholds, their T - and μ -dependence will play a key role when interpreting the structure of spectral functions.

At vanishing chemical potential, the masses and the order parameter show the expected smooth crossover behavior. The pseudo-critical temperature of this crossover is found to be $T_c \approx 175$ MeV, where we used the maximum of the chiral susceptibility $\chi_\sigma \equiv 1/m_\sigma^2$ to determine the location of the crossover, see [84, 85] and [86] for a comparison of different definitions of pseudo-critical temperatures. At higher temperatures, i.e. beyond $T \approx 200$ MeV, the sigma and pion mass degenerate, while the order parameter drastically

7. Phase diagram and thermodynamics

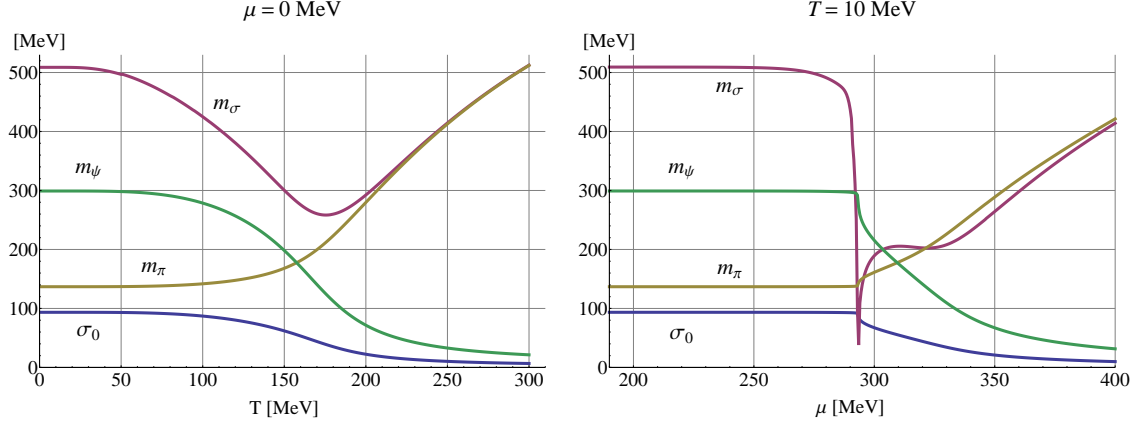


Figure 7.2.: The sigma mass m_σ , the pion mass m_π , the quark mass m_ψ and the chiral order parameter σ_0 are shown vs. temperature T at $\mu = 0 \text{ MeV}$ (left panel), and vs. quark chemical potential μ at $T = 10 \text{ MeV}$ (right panel). Taken from [29].

decreases, indicating the progressive restoration of chiral symmetry.

For a fixed temperature of $T = 10 \text{ MeV}$, we observe that the masses as well as the order parameter basically don't change over a wide range of chemical potential. This is expected from the Silver Blaze property [87], which in this case implies that the partition function and correspondingly all thermodynamic observables at vanishing temperature remain independent of the chemical potential μ until it becomes larger than the constituent quark mass reduced by the binding energy of the resulting quark matter at the first-order transition. Due to the finite temperature of $T = 10 \text{ MeV}$ in our case, we observe small deviations from the Silver Blaze property, in particular there is a small decrease in the sigma mass already before reaching the critical endpoint at $\mu \approx 293 \text{ MeV}$. At the critical endpoint, which represents a second order phase transition, the sigma mass is expected to vanish, which is reproduced to a good extent by our numerical calculation, cf. Fig. 7.2. At larger values of the quark chemical potential we again observe that the meson masses tend to become degenerate, similar to the high temperature case, as chiral symmetry is gradually restored.

We now turn to the entropy density $s(T)$, which will be used in Ch. 10 in order to calculate the shear viscosity to entropy density ratio η/s . The entropy density can be obtained from the temperature dependence of the pressure, cf. Eq. (3.16), and is shown in Fig. 7.3 vs. temperature at $\mu = 0$. Without including the thermal corrections from higher scales, cf. Sec. 3.2, the entropy density does not approach the Stefan-Boltzmann value of

$$\frac{s_{\text{SB}}}{T^3} = \frac{14}{15}\pi^2 \approx 9.21 \quad (7.1)$$

at high temperatures, cf. Eq. (3.19). On the other hand, when these UV corrections are

7. Phase diagram and thermodynamics

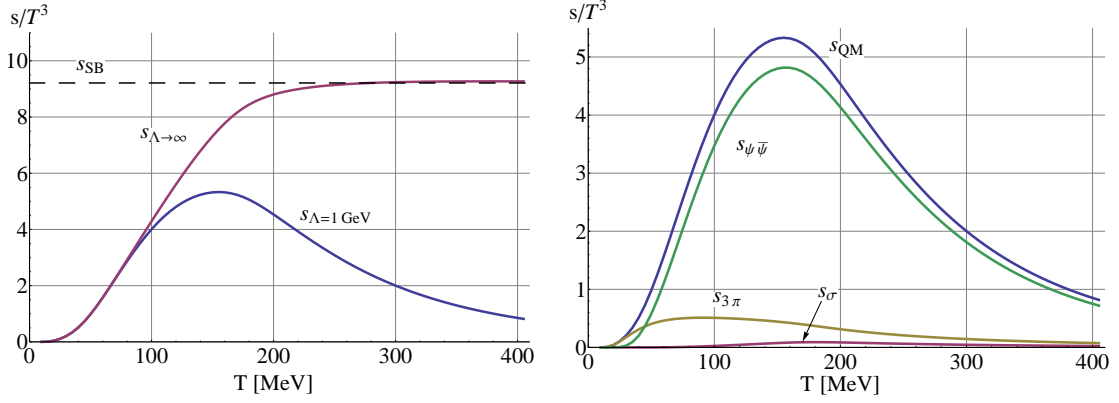


Figure 7.3.: Left: The entropy density of the quark-meson model is shown for the standard choice of $\Lambda = 1 \text{ GeV}$ without UV corrections, $s_{\Lambda=1 \text{ GeV}}$, and with UV corrections, $s_{\Lambda \rightarrow \infty}$. The corresponding Stefan-Boltzmann value is denoted as $s_{\text{SB}} = 14/15\pi^2 \approx 9.21$. Right: The different contributions to the entropy density $s_{\text{QM}} \equiv s_{\Lambda=1 \text{ GeV}}$ are shown, where $s_{\psi\bar{\psi}}$ corresponds to quarks and anti-quarks, $s_{3\pi}$ to the three pion species, and s_{σ} to the sigma mesons.

included, the Stefan-Boltzmann value is reproduced at high temperatures, cf. Fig. 7.3.

It is also instructive to study the different contributions to the entropy density from the different particles. These can be obtained via Eq. (3.16), where, however, when using finite differences to obtain the derivative with respect to temperature, only the temperature of the particle species in question is changed in the flow equation for the effective potential.

On the right-hand side of Fig. 7.3 we show the entropy density of the quarks, the three pion species and the sigma mesons together with the full entropy density of the quark-meson system, without the thermal corrections. We note that the quarks and anti-quarks generate the bulk value of the entropy density while the mesonic contribution to the entropy density is considerably smaller, except at temperature below $T \approx 50 \text{ MeV}$, where the entropy density corresponds to that of a pion gas. In particular, we checked that our result for the entropy density agrees quantitatively for $T \lesssim 30 \text{ MeV}$ with the result based on chiral perturbation theory presented in [82].

8

Decay channels and two-point functions

In this chapter, we will first discuss the different time-like and space-like quasi-particle processes that can occur within our framework in Sec. 8.1. These processes determine the shape of the retarded two-point functions and, consequently, the structure of the spectral functions. As an instructive example, we then study the real and imaginary part of the retarded sigma and pion two-point functions at a temperature of $T = 100$ MeV and discuss the effects from the different decay channels in Sec. 8.2.

8.1 Available decay channels and quasi-particle processes

In order to interpret the shape of the spectral functions, it will be instructive to study the different particle processes that can occur in our framework. In this section, which is based on [68], we therefore summarize the possible processes and their kinematic constraints. The possible processes can already be read off from the structure of the flow equations for the two-point functions, cf. Fig. 3.3, and are represented explicitly in Fig. 8.1.

For example, the first diagram in Fig. 8.1 represents the decay of an off-shell sigma meson, denoted as σ^* , with total energy ω and spatial momentum \vec{p} into two on-shell sigma mesons, denoted as σ . If the spatial momentum is zero, this process can only occur when the energy ω is larger than two times the sigma mass m_σ , which follows from requiring energy conservation at the vertex. For a finite spatial momentum \vec{p} , the kinematic constraint also follows from energy- and momentum-conservation at the vertex and is given by Eq. (8.1). In the following, we will classify such processes, where the squared four-momentum of the off-shell particle is larger than zero, $p^2 = \omega^2 - \vec{p}^2 > 0$, as being time-like, while processes with $p^2 < 0$ will be called space-like. In general, time-like processes can be interpreted in terms of particle creation, annihilation and absorption

8. Decay channels and two-point functions

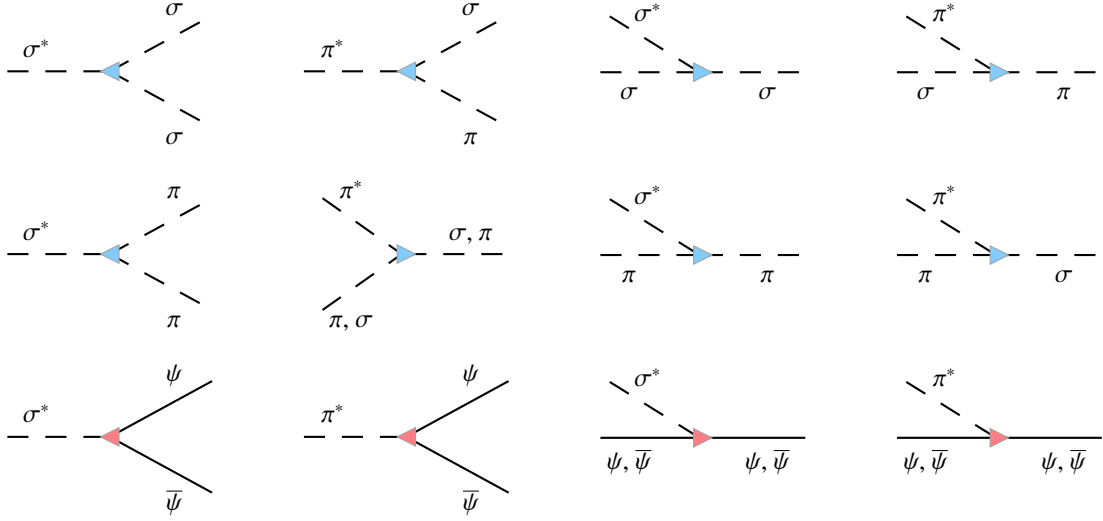


Figure 8.1.: Graphical representation of the possible time-like, $p^2 = \omega^2 - \vec{p}^2 > 0$, and space-like, $p^2 < 0$, processes. Asterisks denote off-shell particles while others represent on-shell particles from a heat bath. First column: time-like decay channels for an off-shell sigma, σ^* . Second column: time-like decay channels for an off-shell pion, π^* . Third column: absorption or emission of a space-like sigma excitation. Fourth column: absorption or emission of a space-like pion excitation. Taken from [68].

reactions, while space-like processes represent the emission or absorption of space-like excitations.

The available time-like processes for an external off-shell sigma meson with energy ω and spatial momentum \vec{p} are represented by the first column of Fig. 8.1 and are explicitly given by

$$\sigma^* \rightarrow \sigma + \sigma, \quad \omega \geq \sqrt{(2m_\sigma)^2 + \vec{p}^2}, \quad (8.1)$$

$$\sigma^* \rightarrow \pi + \pi, \quad \omega \geq \sqrt{(2m_\pi)^2 + \vec{p}^2}, \quad (8.2)$$

$$\sigma^* \rightarrow \psi + \bar{\psi}, \quad \omega \geq \sqrt{(2m_\psi)^2 + \vec{p}^2}. \quad (8.3)$$

We note that the decay products are on-shell, since they represent real particles in a heat bath, and that their masses are to be identified with the curvature masses in our truncation. Moreover, the inverse of the above processes is also possible at finite temperature, giving rise to an equilibrium between direct and inverse processes. In fact, the total decay rates for these processes can be read off from the flow equations for the retarded two-point functions, which can be expressed in terms of statistical weight factors, i.e. combinations of occupation numbers, see also the discussion in App. C.

8. Decay channels and two-point functions

Similarly, the time-like processes for an off-shell pion π^* are given by

$$\pi^* \rightarrow \sigma + \pi, \quad \omega \geq \sqrt{(m_\sigma + m_\pi)^2 + \vec{p}^2}, \quad (8.4)$$

$$\pi^* + \pi \rightarrow \sigma, \quad |\vec{p}| \leq \omega \leq (m_\sigma - m_\pi) \sqrt{1 + \vec{p}^2 / \Delta m^2}, \quad (8.5)$$

$$\pi^* + \sigma \rightarrow \pi, \quad |\vec{p}| \leq \omega \leq (m_\pi - m_\sigma) \sqrt{1 + \vec{p}^2 / \Delta m^2}, \quad (8.6)$$

$$\pi^* \rightarrow \psi + \bar{\psi}, \quad \omega \geq \sqrt{(2m_\psi)^2 + \vec{p}^2}, \quad (8.7)$$

with $\Delta m^2 \equiv (m_\sigma - m_\pi)^2$. These processes are represented by the second column in Fig. 8.1. As compared to the time-like decays of the sigma meson, we note that the pion cannot decay into two sigma mesons, nor into two pions. This is due to the fact that parity is conserved in our framework. Hence, parity-violating processes like $\pi^* \rightarrow \sigma + \sigma$ are forbidden. The pion can therefore only decay into a sigma meson and a pion, cf. Eq. (8.4), or into a quark-antiquark pair, cf. Eq. (8.7). Another possibility for the pion to undergo a time-like process is to absorb a particle from the heat bath. For example, the process given by Eq. (8.5) describes the absorption of an on-shell pion by an off-shell pion resulting in the generation of a sigma meson. Such thermal processes require real particles from the heat bath and can only occur at finite temperature or density. Moreover, the kinematical constraint given by Eq. (8.5) requires the sigma mass to be larger than the pion mass for this process to be possible.¹ Near the critical endpoint, however, the sigma mass can become smaller than the pion mass, cf. Fig. 7.2. In this case, the process $\pi^* + \pi \rightarrow \sigma$ can no longer occur, while the process $\pi^* + \sigma \rightarrow \pi$, where a sigma meson is absorbed and a pion is produced, becomes possible, cf. Eq. (8.6).

We now turn to the space-like processes of the sigma meson. They can only occur when the energy ω is smaller than the spatial momentum $|\vec{p}|$ and are given by

$$\left. \begin{array}{l} \sigma^* + \sigma \rightarrow \sigma \\ \sigma^* + \pi \rightarrow \pi \\ \sigma^* + \psi \rightarrow \psi \\ \sigma^* + \bar{\psi} \rightarrow \bar{\psi} \end{array} \right\} 0 \leq \omega < |\vec{p}|. \quad (8.8)$$

They are represented by the third column of Fig. 8.1 and describe the absorption, or, when considering the inverse processes, the emission of an off-shell sigma meson by a particle from the heat bath.

Similarly, the space-like processes for a pion excitation are given by

$$\left. \begin{array}{l} \pi^* + \sigma \rightarrow \pi \\ \pi^* + \pi \rightarrow \sigma \\ \pi^* + \psi \rightarrow \psi \\ \pi^* + \bar{\psi} \rightarrow \bar{\psi} \end{array} \right\} 0 \leq \omega < |\vec{p}|, \quad (8.9)$$

¹We note that the lower kinematical bound of the processes given by Eq. (8.5) and Eq. (8.6) only arises due to their classification as being time-like.

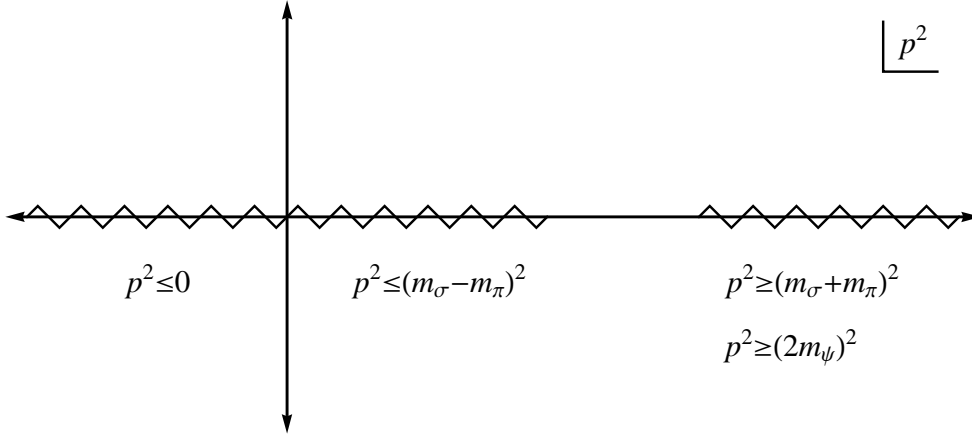


Figure 8.2.: The branch cut structure of the pion propagator $D_\pi(p^2)$ at finite temperature is represented in the complex p^2 -plane, where $p^2 = \omega^2 - \vec{p}^2$. The location of the branch cuts are given by the thresholds of the different time-like and space-like processes, cf. Eqs. (8.4)-(8.7) and Eq. (8.9).

as represented by the fourth column of Fig. 8.1. We note that all space-like processes require real particles from the heat bath and are therefore only possible at finite temperature or density.

We conclude this section by discussing the branch cut structure of the two-point functions induced by these time-like and space-like processes. As an example, the different branch cuts of the pion two-point function are represented in Fig. 8.2. We note that the time-like processes $\pi^* \rightarrow \pi + \sigma$ and $\pi^* \rightarrow \psi + \bar{\psi}$, as given by Eq. (8.4) and Eq. (8.7), give rise to discontinuities along the real axis for $p^2 \geq (m_\sigma + m_\pi)^2$ and $p^2 \geq (2m_\psi)^2$, respectively. Similarly, one of the thermal processes $\pi^* + \pi \rightarrow \sigma$ and $\pi^* + \sigma \rightarrow \pi$, cf. Eq. (8.5) and Eq. (8.6), gives rise to a branch cut at $p^2 \leq (m_\sigma - m_\pi)^2$. This branch cut extends to $p^2 \rightarrow -\infty$ and is responsible for the non-analyticity at the origin at finite temperature, as discussed in Sec. 4.2. At $p^2 < 0$, also the space-like processes given by Eq. (8.9) give rise to a discontinuity of the imaginary part of the two-point function at finite temperature.

8.2 Real and imaginary part of retarded two-point functions

The different processes discussed in the last section give rise to modifications of the shape of the two-point functions, i.e. the inverse propagators, which consequently determine the shape of the spectral functions, cf. Eq. (4.34). In this section, which is based on [29], we will therefore present an instructive example for the real and imaginary part of the retarded sigma and pion two-point functions, cf. Eqs. (3.23)-(3.24), and discuss how they are affected by the different processes described in the last section. For a discussion of retarded two-point functions within the $O(N)$ model we refer to [16].

8. Decay channels and two-point functions

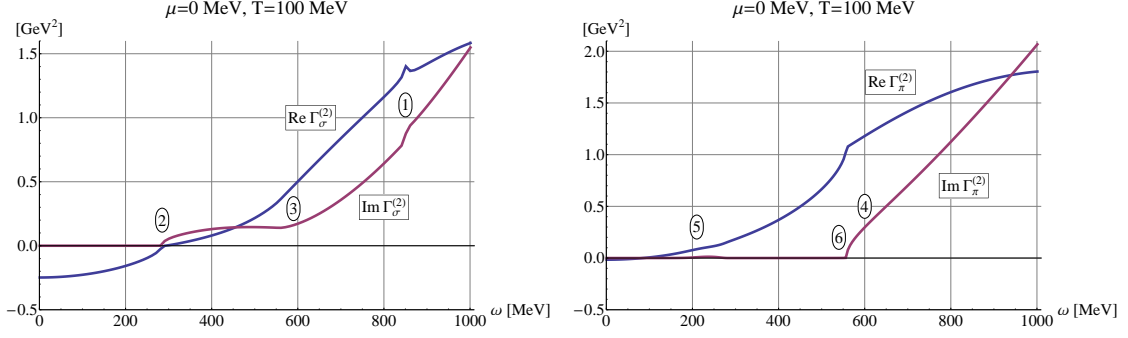


Figure 8.3.: The real and imaginary part of the retarded sigma and pion two-point functions, $\Gamma_{\sigma,\pi}^{(2),R}(\omega)$, are shown versus external energy ω at a temperature of $T = 100$ MeV, chemical potential $\mu = 0$ and vanishing external momentum $\vec{p} = 0$. Inset numbers refer to the different processes affecting the 2-point functions in the corresponding energy regimes, see also Eqs. (8.1)-(8.7). In particular, the processes are labelled as 1: $\sigma^* \rightarrow \sigma\sigma$, 2: $\sigma^* \rightarrow \pi\pi$, 3: $\sigma^* \rightarrow \psi\bar{\psi}$, 4: $\pi^* \rightarrow \sigma\pi$, 5: $\pi^*\pi \rightarrow \sigma$, 6: $\pi^* \rightarrow \psi\bar{\psi}$.

In particular, we will discuss the influence of the time-like processes on the sigma and the pion two-point function at a temperature of $T = 100$ MeV at $\mu = 0$ and vanishing external spatial momentum, i.e. $\vec{p} = 0$, cf. Fig. 8.3. We note that the two-point functions show significant modifications due to the different processes in energy regimes where these processes are possible, cf. Eqs. (8.1)-(8.7), as indicated by inset numbers in Fig. 8.3.

At energies where there is no decay channel available, the imaginary part of the mesonic two-point functions is given by its UV value, cf. Eqs. (6.7)-(6.8), which is zero in the limit $\epsilon \rightarrow 0$. The real part, in general, shows the same $-\omega^2$ -behaviour as its UV value but is shifted to negative values. This effect is partly due to the mesonic tadpole diagrams, cf. Fig. 3.3, which only give rise to ω -independent contributions in our truncation, where the vertices are taken to be momentum independent.

The real part of the retarded sigma two-point function shows a zero-crossing at $\omega \approx 290$ MeV. Since the corresponding imaginary part takes on a non-zero value already for $\omega \geq 2m_\pi \approx 280$ MeV, due to the decay of a sigma meson into two pions, the zero-crossing of the real part does not correspond to a stable sigma state in this case, nor to a pronounced peak in the spectral function, cf. Fig. 9.1. At higher energies, i.e. for $\omega \geq 2m_\psi \approx 560$ MeV, the decay into a quark anti-quark pair gives rise to a significant increase of the imaginary part of $\Gamma_\sigma^{(2),R}(\omega)$, which is further enhanced when the decay channel into two sigma mesons becomes available, cf. Eq. (8.1).

The real part of the pion two-point function exhibits a zero-crossing at $\omega \approx 100$ MeV, giving rise to a pronounced peak in the spectral function, cf. Fig. 9.1. In the vacuum, this peak would turn into a Dirac delta function in the limit $\epsilon \rightarrow 0$ in our framework. At finite temperature, however, the thermal scattering process $\pi^* + \pi \rightarrow \sigma$ is possible at energies $\omega \leq m_\sigma - m_\pi \approx 260$ MeV, cf. Eq. (8.5), which gives rise to a non-vanishing

8. Decay channels and two-point functions

imaginary part of $\Gamma_{\pi}^{(2),R}(\omega)$ and, consequently, to a finite peak height and width of the spectral function. At higher energies, the quark decay channel, cf. Eq. (8.7), and the decay into a pion and a sigma meson, cf. Eq. (8.4), are possible and generate large values of the imaginary part of $\Gamma_{\pi}^{(2),R}(\omega)$.

9

Spectral functions

In this chapter, we will present results on the pion and sigma spectral functions at finite temperature, chemical potential and finite external spatial momentum. In particular, the temperature and chemical potential dependence of the spectral functions is discussed in Sec. 9.1, where we again focus on the line of zero chemical potential, and the fixed temperature line that crosses the critical endpoint in the phase diagram of the quark-meson model. In Sec. 9.2, we then discuss the spatial momentum dependence of the spectral functions. The energy- and momentum dependence of the spectral functions will be used in Ch. 10 to calculate the shear viscosity.

9.1 Spectral functions at finite temperature and chemical potential

In this section, which is based on [29], results on the sigma and pion spectral function, as obtained from the corresponding retarded two-point functions via Eq. (4.34), are presented at finite temperature and chemical potential. In particular, we will study their temperature dependence at vanishing chemical potential and their change with chemical potential along the fixed-temperature line that crosses the critical endpoint, cf. Fig. 9.1.

We note, however, that the quark-meson model is not expected to provide a quantitatively reliable description of the QCD phase diagram at large values of the chemical potential since explicit baryonic (and gluonic) degrees of freedom are not included. In particular, the mixing of the sigma fluctuations with those of the baryon density in the nuclear matter region might lead to significant changes, e.g., in the location of the CEP and the phase structure at higher densities. However, we expect that the qualitative effects discussed below, such as the sigma spectral function developing a pole at zero energy near the CEP, are to a large extent universal and not qualitatively affected by

9. Spectral functions

baryonic or gluonic fluctuations.

We now turn to a discussion of Fig. 9.1, where the sigma and pion spectral functions, $\rho_\sigma(\omega)$ and $\rho_\pi(\omega)$, are shown as a function of external energy ω at vanishing external spatial momentum, $\vec{p} = 0$. The different time-like processes affecting the spectral functions, cf. Eqs. (3.23)-(3.24), are indicated by inset numbers.

At $T = 10$ MeV and $\mu = 0$ MeV the spectral functions closely resemble the vacuum structure already observed in previous studies, cf. [16, 17]. The pion spectral function exhibits a peak close to $\omega = 100$ MeV, originating from a zero-crossing of the real part of $\Gamma_\pi^{(2),R}(\omega)$, to be identified with the pion pole mass, see also Sec. 8.2. The corresponding curvature mass, as determined from the effective potential, is found to be $m_\pi = 138$ MeV, cf. Fig. 7.2, and thus is considerably larger than the pole mass. Discrepancies between the pole and screening masses were also observed in [69] and less pronounced in purely bosonic models within similar truncations [16, 88], and are expected to decrease with an increased momentum dependence of the truncation. In particular, already the so-called LPA' truncation, where the scale-dependence of momentum-independent wavefunction renormalization factors is taken into account, is able to resolve these inconsistencies to a large extent [62]. For external energies larger than $2m_\psi$ the decay of an (off-shell) pion into two quarks becomes energetically possible, giving rise to an increase of the imaginary part of $\Gamma_\pi^{(2),R}(\omega)$ and thus also to the pion spectral function for $\omega \geq 2m_\psi \approx 600$ MeV. In addition, the process $\pi^* \rightarrow \sigma + \pi$ leads to modifications of the pion spectral function for $\omega \geq m_\sigma + m_\pi \approx 650$ MeV, but its contribution is about a magnitude smaller than that of the quark decay and therefore not visible in Fig. 9.1. The thermal scattering process $\pi^* + \pi \rightarrow \sigma$ is also suppressed at such low temperatures, as expected.

Turning to the sigma spectral function at $T = 10$ MeV, we note that it is most strongly affected by the decay into two pions, $\sigma^* \rightarrow \pi + \pi$, which is possible for $\omega \geq 2m_\pi$. This process leads to a strong increase of the imaginary part of $\Gamma_\sigma^{(2),R}(\omega)$ at $\omega \gtrsim 275$ MeV, even before the zero-crossing of the real part at $\omega \approx 340$ MeV. At external energies larger than $2m_\psi$, the $\sigma^* \rightarrow \psi + \bar{\psi}$ channel opens up but yields only small contributions compared to the decay into two pions. The process $\sigma^* \rightarrow \sigma + \sigma$ can only occur at external energies larger than $2m_\sigma$, i.e. beyond 1 GeV, and does therefore not appear in Fig. 9.1.

When going to higher temperatures the process $\pi^* + \pi \rightarrow \sigma$, which describes the absorption of a pion from the heat bath by an off-shell pion resulting in the formation of a sigma meson, becomes less suppressed and contributes to the pion spectral function for $\omega \leq m_\sigma - m_\pi$. Since the difference between the meson and pion screening mass continuously decreases with higher temperature at $\mu = 0$ MeV, cf. Fig. 7.2, the maximum energy up to which this process is possible is also shifted to smaller values, as is the corresponding bump in pion spectral function, cf. Fig. 9.1.

Another effect induced by the temperature dependence of the meson and quark masses is the emergence of a stable sigma meson at temperatures close to the crossover temperature, where neither the decay into two pions nor into two quarks is energetically possible. At $T = 150$ MeV we therefore observe a pronounced peak in the sigma spectral function at $\omega \approx 280$ MeV, originating from a zero-crossing of the real part of $\Gamma_\sigma^{(2),R}(\omega)$. When increasing the temperature further, the quarks become the lightest degrees of freedom

9. Spectral functions

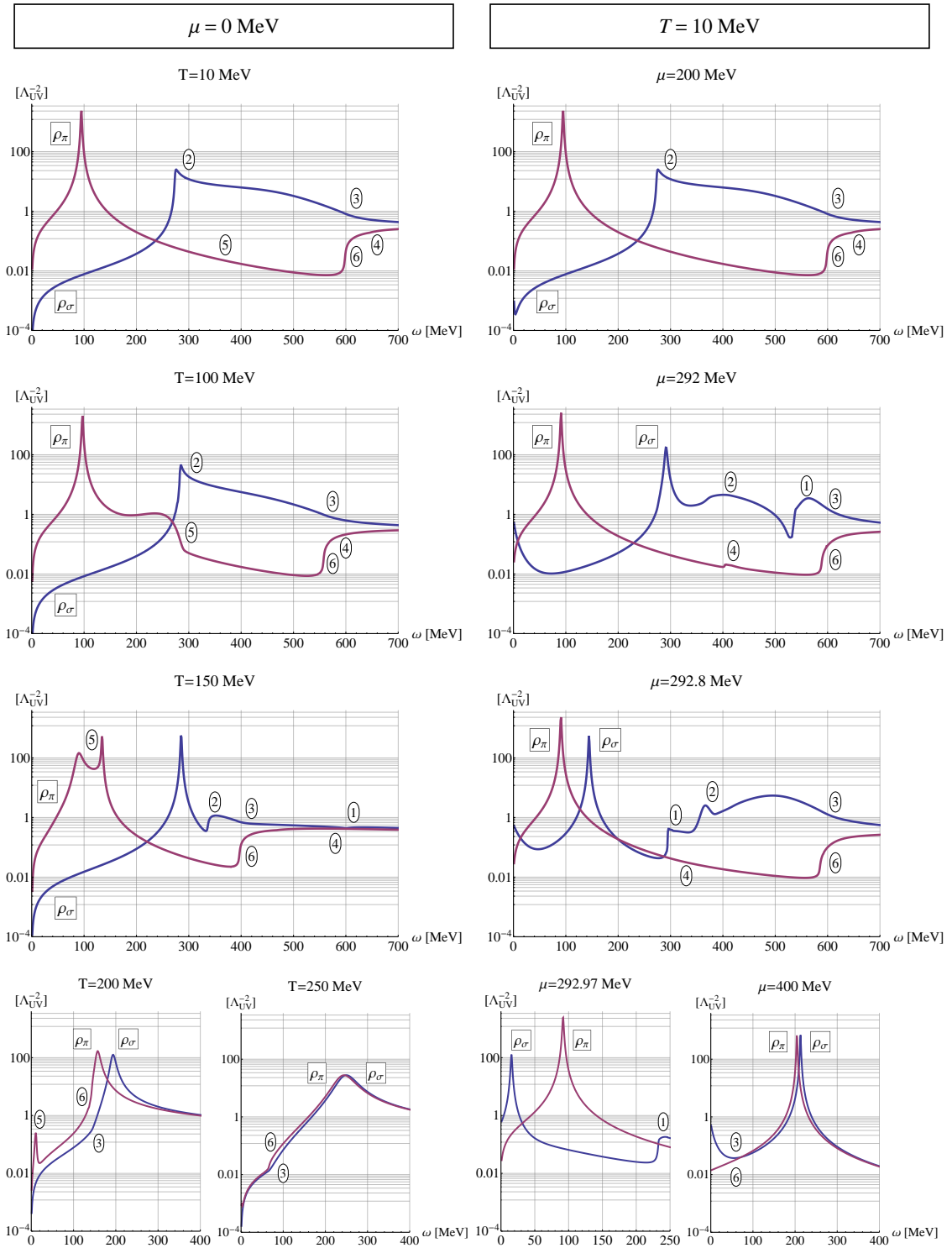


Figure 9.1.: Sigma and pion spectral function, $\rho_\sigma(\omega)$ and $\rho_\pi(\omega)$, shown vs. external energy ω at $\mu = 0$ MeV but different T (left) and at $T = 10$ MeV but different μ (right). Inserted numbers refer to different processes: 1: $\sigma^* \rightarrow \sigma\sigma$, 2: $\sigma^* \rightarrow \pi\pi$, 3: $\sigma^* \rightarrow \psi\bar{\psi}$, 4: $\pi^* \rightarrow \sigma\pi$, 5: $\pi^*\pi \rightarrow \sigma$, 6: $\pi^* \rightarrow \psi\bar{\psi}$. From [29].

9. Spectral functions

considered here, providing decay channels for both the pion and the sigma meson down to small external energies and leading to a broadening of the pronounced peaks in the spectral functions.

At $T = 250$ MeV, the meson screening masses are nearly degenerate and have increased to about 400 MeV, thus shifting the threshold for decays into mesons to twice that value. Additionally, the quark mass has further decreased to approximately 30 MeV, leading to a broad maximum in the almost degenerate sigma and pion spectral functions.

The right column of Fig. 9.1 shows the sigma and pion spectral function at a fixed temperature of $T = 10$ MeV and different values of the quark chemical potential, corresponding to points on a horizontal line in the phase diagram near the critical endpoint. We note that contributions to the pion spectral function arising from the process $\pi^* + \pi \rightarrow \sigma$ are negligible at such low temperatures and are therefore not indicated in these figures. Over a wide range of chemical potentials the spectral functions remain basically unchanged, as expected from the aforementioned Silver Blaze property. Between $\mu = 0$ and $\mu = 200$ MeV the results are practically identical (compare the top left and top right panels in Fig. 9.1). When approaching the critical endpoint, however, especially the sigma spectral function undergoes significant changes.

At $\mu = 292$ MeV, i.e. only about 1 MeV from the critical endpoint, the sigma screening mass has already dropped to about half its vacuum value, leading to a minimal energy for the $\sigma^* \rightarrow \sigma + \sigma$ decay of $\omega \geq 2m_\sigma \approx 540$ MeV. Additionally, a pronounced sigma peak starts to develop at $\omega \approx 290$ MeV, indicating the formation of a stable dynamical sigma meson.

Even closer to the CEP, i.e. at $\mu = 292.8$ MeV, the threshold for the two-sigma decay has decreased to $\omega \approx 290$ MeV and thus occurs already at smaller energies than the $\sigma^* \rightarrow \pi + \pi$ process. The sigma pole mass, given by the location of the sharp peak in the sigma spectral function, has also decreased considerably, taking a value of $m_\sigma^p \approx 140$ MeV, which is still in very good agreement with its screening mass at this point.

At $\mu = 292.97$ MeV, however, the sigma pole mass has already decreased to $m_\sigma^p \approx 20$ MeV, which is in agreement with the expectation that the radial σ -field becomes massless at the CEP, whereas the $\sigma^* \rightarrow \sigma + \sigma$ threshold, as determined by the screening mass here, lags behind. Because the sigma screening mass changes very rapidly close to the endpoint, cf. Fig. 7.2, the difference between the pole and half the 2σ -threshold is very sensitive to this remaining inconsistency in our present truncation and, hence, enhanced in this tiny region around the endpoint. It is manifest in our approach, however, that the pole mass and the screening mass of the sigma meson will both be zero precisely at the critical endpoint and consequently identical again.

When increasing the chemical potential further, the sigma and pion spectral functions become degenerate, similar to the case of high temperatures, but with the difference that the spectral functions exhibit sharp peaks instead of broad resonances, indicating stable dynamical particles. We also observe a small increase of the sigma spectral function at small external energies which has been verified to be due to the finite value of ϵ in our truncation and is expected to vanish in the limit $\epsilon \rightarrow 0$. Moreover, this effect is found to diminish when going to even higher values of the chemical potential, as expected since the fermionic loop functions $J_{k,\bar{\psi}\psi}^{(\sigma)}$ and $J_{k,\bar{\psi}\psi}^{(\pi)}$ are identical in the limit of vanishing quark mass.

9.2 Momentum dependence of spectral functions

In this section, which is based on [68], we study the dependence of the sigma and pion spectral functions on the external spatial momentum \vec{p} . As an instructive example, that allows to study the effects of most of the different time-like and space-like processes presented in Sec. 8.1, we will first discuss the spatial-momentum dependence of the sigma and pion spectral functions at a temperature of $T = 100$ MeV for vanishing quark chemical potential. Then, the influence of a finite external spatial momentum on the mesonic spectral functions near the critical endpoint (CEP) in the phase diagram of the quark-meson model is studied.

The sigma spectral function, $\rho_\sigma(\omega, \vec{p})$, is shown on the left-hand side of Fig. 9.2 at a temperature of $T = 100$ MeV and for different external spatial momenta \vec{p} . For finite external spatial momenta we observe two main effects. On one hand, the time-like regime of the spectral function, $\omega \geq |\vec{p}|$, is boosted to higher energies, as expected from Lorentz covariance, cf. App. E.1, and from the kinematic constraints in Eqs. (8.1)-(8.3). We also note that a small peak forms near the two-pion threshold at larger $|\vec{p}|$, cf. the discussion in App. E.1 on the effects of the small residual violation of Lorentz covariance. On the other hand, the space-like processes given by Eq. (8.8) give rise to an increase of the spectral function in the regime $0 \leq \omega \leq |\vec{p}|$, where the largest contribution is found to stem from the absorption or emission of a sigma excitation by a quark or anti-quark. With increasing momentum $|\vec{p}|$ this new space-like regime is broadened and flattened due to the fact that the same range of loop momenta now gives rise to space-like processes in a larger ω -range, cf. the explicit example given for the pion spectral function below.

We now turn to the momentum-dependence of the pion spectral function, $\rho_\pi(\omega, \vec{p})$, as shown on the right-hand side of Fig. 9.2 at a temperature of $T = 100$ MeV, see also Fig. 9.1 for a discussion of its structure at $\vec{p} = 0$. For finite external spatial momenta we again observe the expected Lorentz-boosting of the spectral function. The effect of the

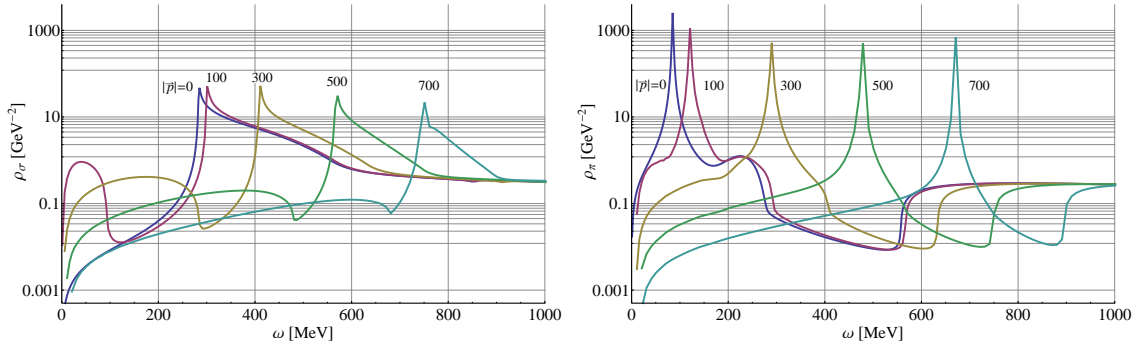


Figure 9.2.: The sigma (left) and pion (right) spectral functions, $\rho_\sigma(\omega, \vec{p})$ and $\rho_\pi(\omega, \vec{p})$, are shown versus external energy ω at $T = 100$ MeV and $\mu = 0$ MeV for different external momenta $|\vec{p}|$ as indicated by inset labels: 0 MeV, 100 MeV, 300 MeV, 500 MeV, 700 MeV. From [68].

9. Spectral functions

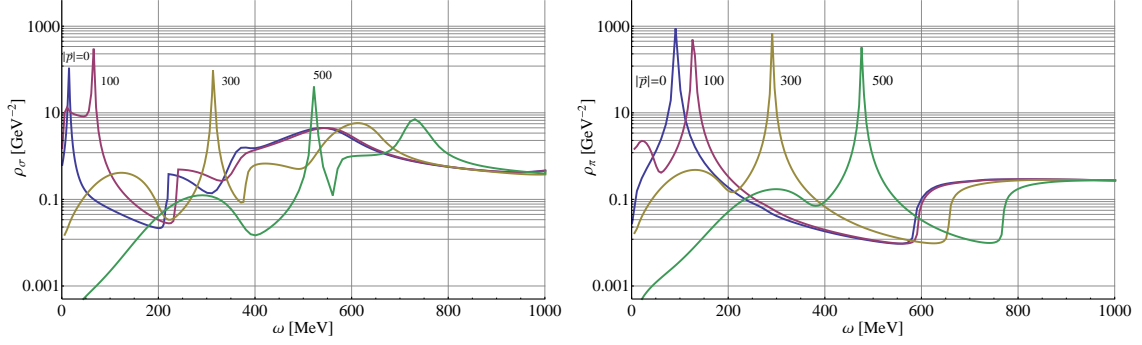


Figure 9.3.: The sigma and pion spectral functions, $\rho_\sigma(\omega, \vec{p})$ and $\rho_\pi(\omega, \vec{p})$, are shown versus external energy ω at $T = 10$ MeV and $\mu = 292.97$ MeV for different external momenta $|\vec{p}|$ as indicated by inset labels: 0 MeV, 100 MeV, 300 MeV, 500 MeV. From [68].

space-like processes is not as pronounced as for the sigma spectral function, which can be explained as follows. When comparing Eqs. (8.5)-(8.6) and the corresponding expressions in Eq. (8.9), we note that they describe essentially the same processes and that it depends on the loop momentum whether the process classifies as time-like or space-like. For example, if we take the loop momentum to be zero, $\vec{q} = 0$, energy conservation yields that $\omega = \sqrt{m_\sigma^2 + \vec{p}^2} - m_\pi$ for the process $\pi^* + \pi \rightarrow \sigma$, which for $T = 100$ MeV and $|\vec{p}| = 100$ MeV leads to a time-like energy of $\omega \approx 295$ MeV. On the other hand, for a loop momentum of, e.g., $\vec{q} = -5\vec{p}$, one gets $\omega \approx 64$ MeV, clearly a space-like configuration.

This explicit example illustrates the fact that the integration over the loop momentum can give rise to space-like as well as time-like contributions which correspond to the same process and that we therefore observe only one threshold associated with the process $\pi^* + \pi \rightarrow \sigma$, given by the upper bound in Eq. (8.5). The process $\pi^* + \sigma \rightarrow \pi$ on the other hand, only gives rise to a space-like contribution since $m_\pi - m_\sigma < 0$ at $T = 100$ MeV. Finally, we note that the effect of the time-like process $\pi^* + \pi \rightarrow \sigma$ decreases with higher momentum $|\vec{p}|$, cf. Fig. 9.2. This is in agreement with the expectation that a particle propagating through a heat bath at a momentum significantly larger than average thermal fluctuations, i.e. $|\vec{p}| \gg T$, should experience no significant modifications from the medium.

We now discuss the influence of a finite spatial momentum on the sigma and pion spectral function near the CEP, cf. Fig. 9.3, which shows $\rho_\sigma(\omega, \vec{p})$ and $\rho_\pi(\omega, \vec{p})$ at a chemical potential of $\mu = 292.97$ MeV and a temperature of $T = 10$ MeV for different external spatial momenta, see also Fig. 9.1 for a discussion of their structure at $\vec{p} = 0$. We note that a value of $\epsilon = 20$ MeV has been used for the sigma spectral function instead of the standard choice of $\epsilon = 0.1$ in an energy range of $\Delta\omega \approx 200$ MeV beyond the sigma-sigma threshold for $|\vec{p}| = 0$ MeV and $|\vec{p}| = 100$ MeV in order to circumvent numerical problems. This method is justified in App. E.2, where it is shown that the spectral functions in our calculation are rather insensitive to ϵ in energy regimes that allow for quasi-particle processes. We have also checked explicitly that the sigma spectral function

9. Spectral functions

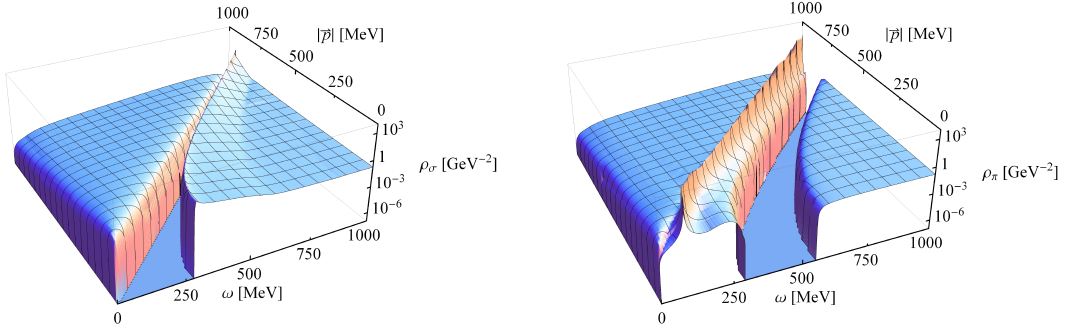


Figure 9.4.: The sigma and pion spectral functions, $\rho_\sigma(\omega, \vec{p})$ and $\rho_\pi(\omega, \vec{p})$, are shown vs. external energy ω and vs. external spatial momentum $|\vec{p}|$ at $T = 100$ MeV and $\mu = 0$ MeV.

shown in Fig. 9.3 does not depend on ϵ at higher energies, where the aforementioned numerical problems do not arise.

For finite external spatial momenta, the sigma spectral function is affected by the same space-like processes as described before, which are now, however, suppressed by the low temperature. For small momenta \vec{p} , these space-like processes affect the shape of the peak in the sigma spectral function, cf. Fig. 9.3. This interference of the space-like part and the peak at time-like energies is, however, only possible due to the finite value for ϵ . In the limit $\epsilon \rightarrow 0$, the peak will turn into a delta function, leaving the space-like part clearly separated, cf. the discussion in App. E.2. The separation of these two regimes becomes more pronounced at higher spatial momenta where the spectral function is boosted to higher energies.

We now turn to the momentum dependence of the pion spectral function near the CEP, as shown on the right panel of Fig. 9.3. At $\vec{p} = 0$ the pion spectral function closely resembles its vacuum shape, cf. Fig. 9.1. At higher momenta we observe similar modifications in the space-like regime as for the sigma spectral function. This is due to the fact that the thresholds for the time-like processes $\pi^* + \pi \rightarrow \sigma$ and $\pi^* + \sigma \rightarrow \pi$, cf. Eqs. (8.5)-(8.6), are now located at very small time-like energies since $m_\sigma \approx 106$ MeV and $m_\pi \approx 139$ MeV in this critical regime. Therefore, the integration over the loop momentum now gives a large contribution for space-like energies, a situation similar to the case of the sigma spectral function, where all thermal processes are anyhow limited to the space-like region. Besides these modifications at space-like energies, we observe that the pion spectral function is boosted to higher energies with increasing spatial momentum, as expected.

It is also instructive to represent the momentum dependence of the spectral functions in a three-dimensional manner, cf. Fig. 9.4, where the sigma and pion spectral function are plotted vs. ω and $|\vec{p}|$ at a temperature of $T = 100$ MeV and $\mu = 0$. Therein, the spectral function has been set to zero within energy- and momentum regions where there are no decay channels available, cf. Eqs. (8.1)-(8.9). This corresponds to taking the limit $\epsilon \rightarrow 0$ since the spectral functions are found to be independent of ϵ at energies and momenta

9. Spectral functions

that allow for quasi-particle processes, cf. App. E.2. As already discussed in Sec. 9.2, we observe a separation of the space-like part of the spectral functions, where $\omega < |\vec{p}|$, and the time-like part, where $\omega > |\vec{p}|$, in particular for the sigma spectral function. For additional 3D plots of the spectral functions at different temperatures and chemical potentials we refer to App. F. We note that the energy- and momentum dependence encoded in these plots serve as input for the calculation of the shear viscosity, as also discussed in the next chapter.

10

Shear viscosity

In this chapter, we present results on the mesonic contributions to the shear viscosity of the quark-meson model as obtained from the energy- and momentum dependence of the spectral functions by using the corresponding Green-Kubo formula, see also Sec. 5.4 for a derivation of the explicit formula used to calculate the shear viscosity. For details on our numerical implementation of this formula we refer to Sec. 6.3. The temperature dependence of the shear viscosity as well as of the shear-viscosity to entropy density ratio is discussed in Sec. 10.1, and results on the shear viscosity near the critical endpoint are presented in Sec. 10.2.

10.1 Shear viscosity and shear viscosity to entropy density ratio at finite temperature

In Fig. 10.1 we show results on the contribution to the shear viscosity from one of the three pion species, η_π , and from the sigma mesons, η_σ , together with the Weinberg result on the shear viscosity of a pion gas, see for example [78], and another result, also based on chiral perturbation theory taken from [82] for comparison.

In general, the main contribution to the shear viscosity is found to be due to the first part in Eq. (6.14), i.e. the integration of the weighted square of the spectral function over energy and spatial momentum, while the other contributions to the shear viscosity are several orders of magnitude smaller. Moreover, if the spectral function exhibits a pronounced peak, as for the pion spectral function in Fig. 9.4, the contribution from the time-like region is found to be a few orders of magnitude larger than the contribution from the space-like region.

At low temperatures, our values for η_π are considerably smaller than the result for a pion gas with a constant scattering amplitude from Weinberg's theorem, which is denoted

10. Shear viscosity

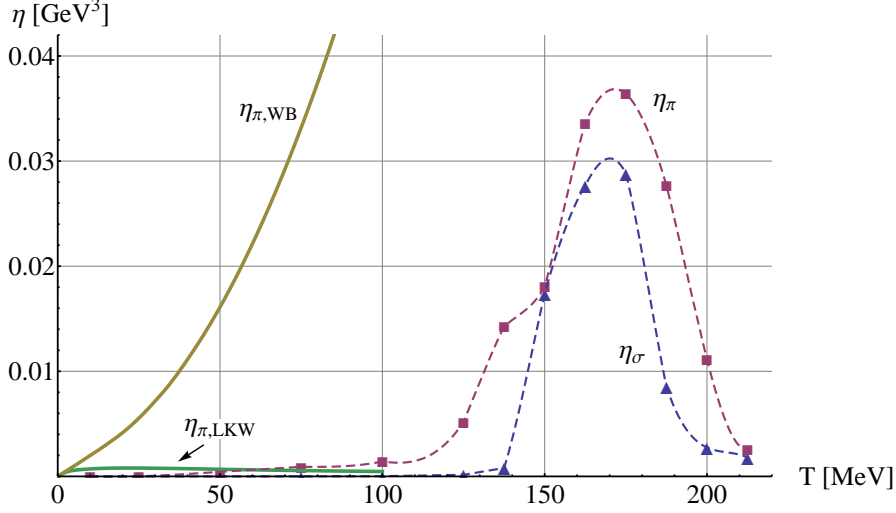


Figure 10.1.: The shear viscosity generated by the sigma mesons η_{σ} and one of the three pion species η_{π} is shown vs. T at $\mu = 0$. For comparison, we also show the corresponding Weinberg result for a pion gas with a constant scattering amplitude η_{WB} from [78], and a more recent result on the shear viscosity of a pion gas by Lang, Kaiser, and Weise [82], denoted as η_{LKW} . Dashed lines are drawn to guide the eye.

as η_{WB} in Fig. 10.1. This is, however, expected, since the Weinberg estimate for the shear viscosity of a pion gas is known to be unrealistically large even at small temperatures, see also [89, 78]. When compared to the results on the shear viscosity of a pion gas by Lang, Kaiser, Weise [82], which is denoted as η_{LKW} in Fig. 10.1, our results are in better agreement, but still smaller for $T \lesssim 50$ MeV. This is due to the finite value of $\epsilon = 0.1$ used in our calculation, which results in a too large width and a too small height of the pion peak at $T \lesssim 100$ MeV. Since the value of the shear viscosity in general increases when the pion peak gets sharper, this overestimation of the peak width gives rise to too small values for the shear viscosity. This problem does not arise for η_{σ} , where we expect the spectral function to be ϵ -independent at low temperatures. The small values of η_{σ} are therefore expected to be reliable and have their origin in the behavior of the derivative of the bosonic occupation number $n'_B(\omega)$ in Eq. (6.14), which decreases rapidly with increasing energy, in particular at low temperatures.

At higher temperatures, $T \gtrsim 100$ MeV, we expect our results to be largely independent of ϵ , except for temperatures that allow for a stable pion or sigma meson. In this case, the corresponding spectral function will exhibit a Dirac delta peak in the limit $\epsilon \rightarrow 0$, which gives rise to an infinite shear viscosity, as for an ideal gas. This is, of course, unrealistic, since the pion and the sigma meson are expected to always have a finite width due to other decay channels like the decay into two photons or weak interaction channels, which are, however, not taken into account in the present approach.

We observe that η_{π} and η_{σ} increase with higher temperatures until they reach a

10. Shear viscosity

maximum at the crossover temperature of $T \approx 170$ MeV, cf. Sec. 7.1. In the case of the pions, this increase of η_π is partly due to the larger temperature itself, which gives rise to larger values of $n'_B(\omega)$ in Eq. (6.14). Another effect that contributes to the larger values of η_π is that the threshold for the thermal scattering process $\pi^* + \pi \rightarrow \sigma$ moves to smaller energies with higher temperatures and eventually gives rise to a stable pion, see Fig. 9.1 and also App. F. Similarly, the increase of η_σ with higher temperatures can be explained by the larger values for $n'_B(\omega)$ and due to the fact that the sigma meson becomes stable for $T \gtrsim 135$ MeV, cf. App. F. The larger values for the shear viscosity therefore indicate small decay widths and long-range correlations, i.e. small masses.

Beyond the crossover temperature of $T \approx 170$ MeV, the shear viscosity of pions and sigma mesons decreases. This is due to the sigma meson and the pion becoming unstable and heavier with higher temperatures, as represented by broad peaks in the spectral functions which move to higher energies with increasing temperature, cf. App. F. The main contribution to the shear viscosity is then expected to be generated by the quarks, which become the relevant degrees of freedom at high temperatures. The calculation of quark spectral functions and of the corresponding shear viscosity therefore represents an interesting extension of our present approach.

We now turn to a discussion of the shear viscosity to entropy density ratio η/s . For the entropy density, we will use the result obtained for the quark-meson model including the UV correction, see also Sec. 7.2, as well as the result obtained for a two-flavor Polyakov-quark-meson (PQM) model in [64], for comparison. The reason for using the entropy density of the PQM model is, that the entropy density of the QM model is unphysical at temperatures below the crossover transition. Within this region of the phase diagram, the entropy density obtained from the QM model is too large due to the contribution from the quarks, which are not confined within hadrons in the QM model. This is also evident from Fig. 10.2, where we show the UV corrected entropy density of the QM model, s_{QM} , together with the entropy density of the PQM model, s_{PQM} , taken from [64], as well as the corresponding Stefan-Boltzmann values. These entropy densities will be used in the following to calculate the shear viscosity to entropy density ratio.

When using the entropy density of the QM model, we obtain the results on the shear viscosity to entropy density ratio presented in Fig. 10.3. Therein, we show the contribution to η/s from a single pion species, η_π/s_{QM} , and from the sigma mesons, $\eta_\sigma/s_{\text{QM}}$, as well as the result obtained from the sum of all three pions and the sigma meson, $\eta_{3\pi+\sigma}/s_{\text{QM}}$, as a function of temperature at $\mu = 0$. For comparison, we also show the result on a pion gas obtained by Lang, Kaiser, Weise [82], which is denoted as $(\eta_{3\pi}/s)_{\text{LKW}}$, and the KSS bound of $\eta/s > 1/4\pi \approx 0.08$.

We note that the KSS bound, which represents a limiting value for the shear viscosity to entropy density ratio, is based on the Maldacena conjecture [91], which states that, under certain conditions, there is a duality between conformal field theories (CFT) and string theory defined on an Anti de Sitter space (AdS). This duality is also referred to as AdS/CFT correspondence or the holographic principle. In the right circumstances it is thus possible to map strong coupling problems in four-dimensional gauge field theory onto problems in five-dimensional classical general relativity. For a large number of such AdS/CFT duals one obtains precisely $\eta/s = 1/4\pi$, which lead Kovtun, Son, and

10. Shear viscosity

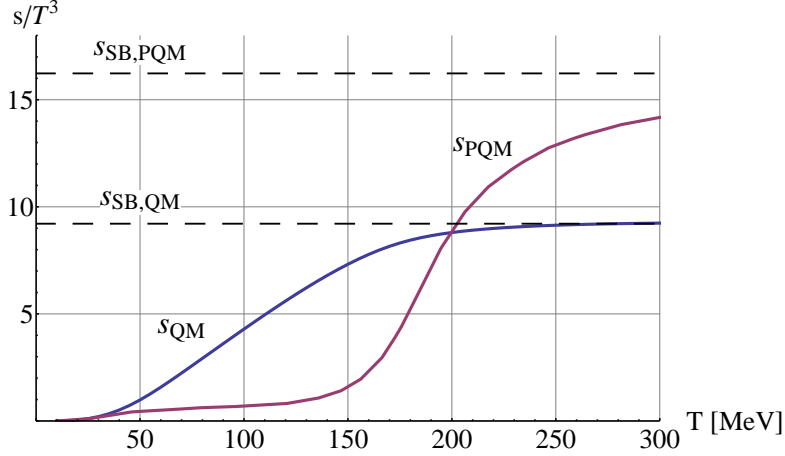


Figure 10.2.: The entropy density of the quark-meson (QM) model, s_{QM} , is shown vs. temperature at $\mu = 0$ in comparison to the entropy density of a two-flavor Polyakov-quark-meson model (PQM), s_{PQM} , taken from [64]. The corresponding Stefan-Boltzmann values are given by $s_{\text{SB,QM}} = 14\pi^2/15$ and $s_{\text{SB,PQM}} = 74\pi^2/45$.

Starinets (KSS) [8] to propose a lower bound of $\eta/s \geq 1/4\pi$ for all relativistic quantum field theories at finite temperature and zero chemical potential. Although this bound is so far respected by experimental results on a wide variety of systems [6], theoretical counterexamples have been found [92, 93]. A more universal bound may be given by $\eta/s \geq (16/25)/4\pi$, which arises from a class of theories dual to Gauss-Bonnet gravity [94, 95].

Turning back to Fig. 10.3, we note that η_π/s_{QM} increases drastically, as expected from chiral perturbation theory, which for example gives

$$\frac{\eta}{s} = \frac{15}{16\pi} \frac{f_\pi^4}{T^4} \quad (10.1)$$

in the chiral limit. When compared to $(\eta_{3\pi}/s)_{\text{LKW}}$, our results are smaller at low temperatures, i.e. at $T \lesssim 50$ MeV, which is due to the small values for the shear viscosity discussed above. At $T \approx 110$ MeV we observe a minimum of $\eta_{3\pi+\sigma}/s_{\text{QM}}$, which is due to the increase of the entropy density at these temperatures, cf. Fig. 10.2. The ratio $\eta_{3\pi+\sigma}/s_{\text{QM}}$ then increases with higher temperatures until it reaches a maximum at the crossover temperature of $T \approx 170$ MeV, which is due to the maximum of the shear viscosity, cf. Fig. 10.1. Beyond the crossover temperature, the shear viscosity to entropy density ratio $\eta_{3\pi+\sigma}/s_{\text{QM}}$ decreases again, due to the decreasing shear viscosity.

From a QCD point-of-view, the shear viscosity to entropy density ratio is expected to increase with higher temperature. In particular, for three flavors of massless quarks the

10. Shear viscosity

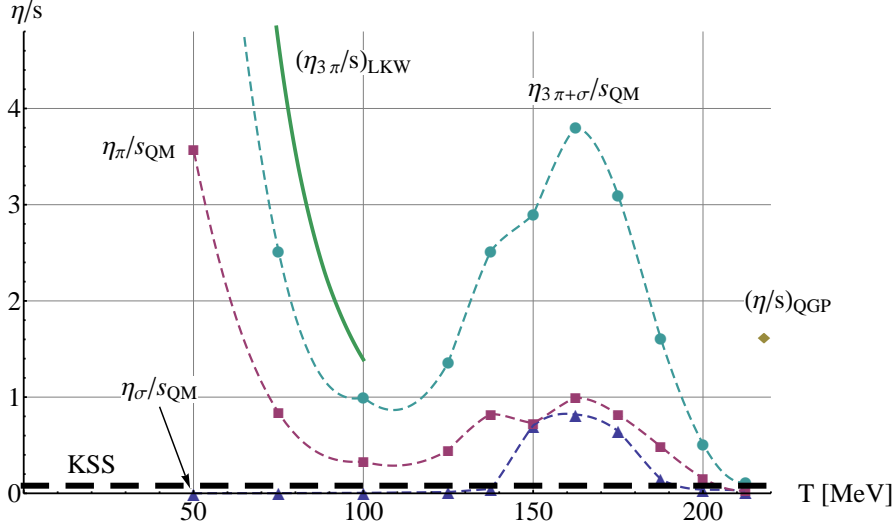


Figure 10.3.: We show the contribution to the shear viscosity to entropy density ratio from a single pion species η_{π}/s_{QM} and from the sigma mesons $\eta_{\sigma}/s_{\text{QM}}$ as well as the result obtained from the sum of all three pions and the sigma meson $\eta_{3\pi+\sigma}/s_{\text{QM}}$ as a function of temperature at $\mu = 0$, where dashed lines are drawn to guide the eye. For the entropy density, we use the UV corrected result obtained from the quark-meson model, s_{QM} , as shown in Fig. 10.2. For comparison, we also show the result obtained for a pion gas by Lang, Kaiser, and Weise [82] based on chiral perturbation theory, denoted as $(\eta_{3\pi}/s)_{\text{LKW}}$, and an estimate for the quark-gluon plasma $(\eta/s)_{\text{QGP}}$ from [90] based on perturbation theory. The limiting bound of $\eta/s \geq 1/4\pi \approx 0.08$ proposed by Kovtun, Son, and Starinets (KSS) [8] is represented by a black dashed line.

perturbative result reported in [90] gives

$$\left(\frac{\eta}{s}\right)_{\text{QGP}} = \frac{5.12}{g^4 \ln(2.42/g)}, \quad (10.2)$$

where the running of the QCD coupling $g(T)$ can be estimated by the following two-loop renormalization group expression,

$$\frac{1}{g^2(T)} = \frac{9}{8\pi^2} \ln\left(\frac{T}{\Lambda_T}\right) + \frac{4}{9\pi^2} \ln\left(2 \ln\left(\frac{T}{\Lambda_T}\right)\right), \quad (10.3)$$

with $\Lambda_T = 30$ MeV, which approximately corresponds to using an energy scale of $2\pi T$ and $\Lambda_{\overline{MS}} = 200$ MeV. For comparison, the resulting shear viscosity to entropy density ratio $(\eta/s)_{\text{QGP}}$, at a temperature of $T \approx 220$ MeV, is also shown in Fig. 10.3.

When using the entropy density of the PQM model, we obtain the results on the shear

10. Shear viscosity

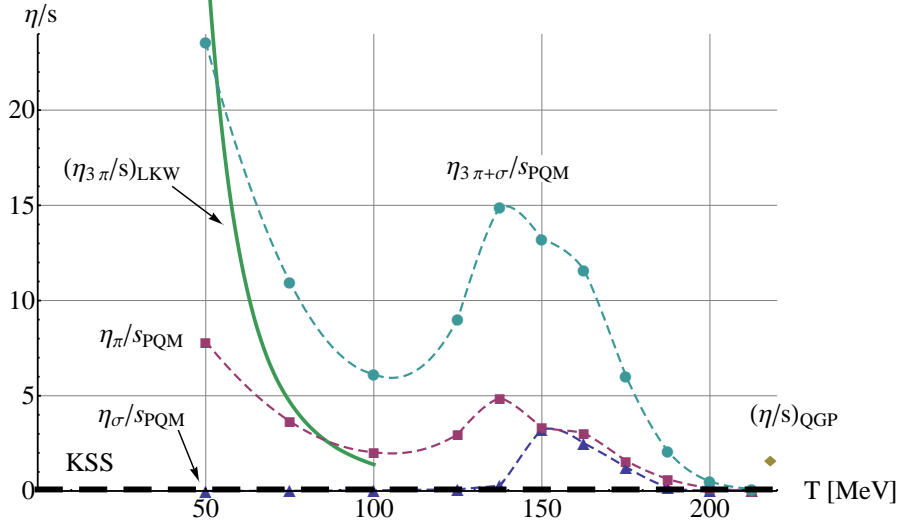


Figure 10.4.: We show the contribution to the shear viscosity to entropy density ratio from a single pion species $\eta_{\pi}/s_{\text{PQM}}$ and from the sigma mesons $\eta_{\sigma}/s_{\text{PQM}}$ as well as the result obtained from the sum of all three pions and the sigma meson $\eta_{3\pi+\sigma}/s_{\text{PQM}}$ as a function of temperature at $\mu = 0$, where dashed lines are drawn to guide the eye. For the entropy density we use the result obtained for the Polyakov quark-meson model in [64], s_{PQM} , as shown in Fig. 10.2. For comparison, we also show the result obtained for a pion gas by Lang, Kaiser, and Weise [82] based on chiral perturbation theory, denoted as $(\eta_{3\pi}/s)_{\text{LKW}}$, and an estimate for the quark-gluon plasma $(\eta/s)_{\text{QGP}}$ from [90] based on perturbation theory. The limiting bound of $\eta/s \geq 1/4\pi \approx 0.08$ proposed by Kovtun, Son, and Starinets (KSS) [8] is represented by a black dashed line.

viscosity to entropy density ratio presented in Fig. 10.4. In particular at temperatures below the crossover transition, i.e. at $T \lesssim 175$ MeV, corresponding to the confined phase, the entropy density of the PQM model is more realistic than the entropy density obtained from the QM model, see also the discussion and the comparison to results from lattice QCD in [64]. We therefore expect, that our results for η/s are more realistic at $T \lesssim 175$ MeV when using the PQM entropy density. Indeed, when comparing Fig. 10.3 and Fig. 10.4, we note that $\eta_{3\pi+\sigma}/s_{\text{PQM}}$ is, at low temperatures, in better agreement with the result obtained for a pion gas, $(\eta_{3\pi}/s)_{\text{LKW}}$, from [82]. At temperatures higher than $T \approx 200$ MeV, the entropy density of the PQM model becomes larger than the entropy density of the QM model, cf. Fig. 10.2, which leads to a smaller shear viscosity to entropy density ratio. At such high temperatures, $\eta_{3\pi+\sigma}/s_{\text{PQM}}$ even falls below the KSS bound, which again indicates that the quark contribution to the shear viscosity is missing.

10.2 Shear viscosity near the critical endpoint

Now we turn to results on the shear viscosity near the critical endpoint, cf. Fig. 10.5, where η_σ and η_π are shown as a function of μ at a fixed temperature of $T = 10$ MeV. As already discussed, the standard choice of $\epsilon = 0.1$ MeV is too large at small temperatures when the spectral functions exhibit sharp peaks, which results in unrealistically small values for the shear viscosity. However, since the temperature is kept constant, this effect is expected to affect the results shown in Fig. 10.5 like a μ -independent overall scaling factor. Hence, relative changes in the shear viscosity are still meaningful.

We observe that the pion contribution to the shear viscosity remains almost constant within the shown μ -range near the CEP, which is located at $\mu \approx 293$ MeV and $T \approx 10$ MeV. On the other hand, the shear viscosity generated by the sigma mesons drastically increases near the CEP, which is due to the stable particle peak in the spectral function moving to smaller energies, cf. Fig. 9.1. We note that exactly at the critical endpoint, the shear viscosity is expected to diverge. For example, a measurement of ${}^3\text{He}$ gives an increase of 10% in the shear viscosity when T is within one part in 10^4 of T_c , see [96]. This divergence is, however, unlikely to be observable in heavy ion collisions [6].

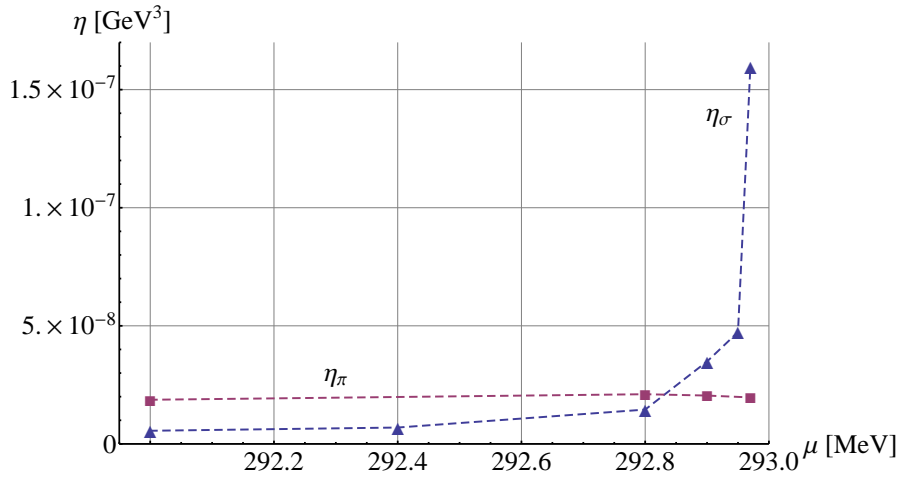


Figure 10.5.: The shear viscosity generated by the sigma mesons η_σ and one of the three pion species η_π is shown vs. μ at $T = 10$ MeV. Dashed lines are drawn to guide the eye.

11

Summary and Outlook

In this thesis, we have developed a new method to calculate real-time quantities like spectral functions and transport coefficients at finite temperature and density within the Functional Renormalization Group approach. Our method involves an analytic continuation from imaginary to real energies on the level of the flow equations which realizes the physical Baym-Mermin boundary conditions. In particular, no numerical scheme for the reconstruction of real-time correlation functions is needed. Our method furthermore preserves the symmetry-breaking pattern of chiral symmetry, it is thermodynamically consistent and does not rely on any assumptions on the analytic structure of the propagators.

We demonstrated the usefulness and practicalness of our method by applying it to the quark-meson model, which acts as a low-energy effective model for QCD. Within this scope, we presented results on the momentum-dependent pion and sigma spectral function at finite temperature and chemical potential, as well as on the corresponding shear viscosity and shear viscosity to entropy density ratio. Our presentation concentrated on the temperature dependence at vanishing chemical potential and on the vicinity of the critical endpoint in the phase diagram of the quark-meson model.

We have shown that the in-medium spectral functions experience a variety of modifications which can be directly connected to several time-like and space-like processes. In particular, the time-like decay channels affecting the sigma spectral function are given by $\sigma^* \rightarrow \sigma + \sigma$, $\sigma^* \rightarrow \pi + \pi$ and $\sigma^* \rightarrow \psi + \bar{\psi}$ while the corresponding space-like processes are summarized as $\sigma^* + \sigma \rightarrow \sigma$, $\sigma^* + \pi \rightarrow \pi$ and $\sigma^* + \psi \rightarrow \psi$. Similarly, the time-like channels available to an off-shell pion are given by $\pi^* \rightarrow \sigma + \pi$, $\pi^* + \pi \rightarrow \sigma$, $\pi^* + \sigma \rightarrow \pi$, $\pi^* \rightarrow \psi + \bar{\psi}$ while the space-like processes can be written as $\pi^* + \sigma \rightarrow \pi$, $\pi^* + \pi \rightarrow \sigma$ and $\pi^* + \psi \rightarrow \psi$.

At low temperatures, the pion spectral function exhibits a sharp peak, associated to a stable pion, while the sigma spectral function shows a broad maximum, indicating an

11. Summary and Outlook

unstable sigma resonance. At higher temperatures corresponding to the smooth crossover region, the sigma meson becomes lighter and even stable. Beyond the crossover, the pion and the sigma meson become unstable, due to the quark-antiquark decay channel, and degenerate, as expected from the progressing restoration of chiral symmetry.

When turning to a finite chemical potential, we observe that the sigma and pion spectral functions do not change over a wide range of chemical potential at low temperatures, as expected from the Silver Blaze property. Near the critical endpoint, however, we observe that the sigma meson turns into an almost massless excitation and that the decay of an off-shell sigma meson into two on-shell sigma mesons results in drastic changes of the sigma spectral function. At larger values of the chemical potential, the sigma meson again becomes unstable and degenerate with the pion, as in the high-temperature case.

Furthermore, we studied the spatial-momentum dependence of the spectral functions at finite temperature and chemical potential. It was found that the time-like region of the spectral functions is boosted towards higher energies while the regime with energies smaller than the spatial momentum is modified by space-like processes.

Based on the momentum dependence of the spectral functions, we were able to calculate the corresponding shear viscosity and the shear viscosity to entropy density ratio using the corresponding Green-Kubo formula. At temperatures and chemical potentials that allow for an (almost) stable particle excitation, our results are impaired by numerical difficulties and are too small as compared to results based on, e.g., chiral perturbation theory. At $\mu = 0$ and $T \gtrsim 100$ MeV, we, however, expect our results to be more reliable and observe a maximum of the pion and sigma shear viscosity at the crossover temperature, i.e. $T \approx 170$ MeV. Similarly, also the shear viscosity to entropy density ratio shows a maximum near the crossover, in addition to a minimum at $T \approx 110$ MeV. We note that the quark contribution to the shear viscosity is not included in the present approach. Still, our results respect the lower bound of $\eta/s \leq 1/4\pi$ up to temperatures of $T \approx 200$ MeV. Near the critical endpoint, we find that the shear viscosity contribution from the sigma mesons tends to diverge, as expected at this second order phase transition.

The new method to calculate real-time quantities like spectral functions and transport coefficients developed in this thesis represents a promising first step towards a multitude of further applications. For example, a straightforward extension of our method is to calculate the quark spectral function, which will allow for a more realistic description of the shear viscosity and the shear viscosity to entropy density ratio at high temperatures. In addition, also the calculation of further transport coefficients like the bulk viscosity, the thermal conductivity and the electrical conductivity are promising applications of our approach. Moreover, the inclusion of vector and axial-vector mesons is feasible and particularly interesting, for example, in terms of the calculation and interpretation of dilepton spectra. Finally, we note that our approach can also be systematically improved towards full QCD by using appropriate input to model the influence of the gauge-field dynamics.

A

Notation and Conventions

A.1 Natural units and notation

Throughout this thesis we use natural units, i.e.

$$\hbar = 1, \quad c = 1, \quad k_B = 1. \quad (\text{A.1})$$

The conversion factor $\hbar c \approx 197 \text{ MeV}\cdot\text{fm}$ can be used to recover SI units.

Unless stated otherwise, roman indices, e.g. i, j, \dots , refer to spatial components and range over the set $\{1, 2, 3\}$, while greek indices, e.g. μ, ν, \dots , refer to space-time components and range over the set $\{0, 1, 2, 3\}$.

Moreover, we use the Einstein summation convention, which implies a summation over indices that appear twice in a single term, once in an upper (superscript) and once in a lower (subscript) position, i.e.

$$c_i x^i = \sum_{i=1}^3 c_i x^i. \quad (\text{A.2})$$

When both indices appear in upper or lower positions there is, in general, no summation implied. For example, there is no summation included in the following expression,

$$\langle [T^{ij}(x), T^{ij}(x')] \rangle, \quad (\text{A.3})$$

where the commutator is defined as $[A, B] = AB - BA$, and $\langle \cdot \rangle$ in general refers to the (thermal) expectation value.

A.2 Euclidean space-time

When performing calculations within the FRG framework in this thesis, we usually employ Euclidean space-time. In particular, we use a purely positive Euclidean metric and the chiral representation of the Euclidean gamma matrices, which reads

$$\gamma^0 = \begin{pmatrix} 0 & \mathbb{1} \\ \mathbb{1} & 0 \end{pmatrix}, \quad \gamma^j = \begin{pmatrix} 0 & i\sigma^j \\ -i\sigma^j & 0 \end{pmatrix}, \quad (\text{A.4})$$

where σ^j are the Pauli matrices,

$$\sigma^1 = \begin{pmatrix} 0 & 1 \\ 1 & 0 \end{pmatrix}, \quad \sigma^2 = \begin{pmatrix} 0 & -i \\ i & 0 \end{pmatrix}, \quad \sigma^3 = \begin{pmatrix} 1 & 0 \\ 0 & -1 \end{pmatrix}. \quad (\text{A.5})$$

The Dirac matrices then fulfill the Euclidean Clifford algebra,

$$\{\gamma^\mu, \gamma^\nu\} = 2\delta^{\mu\nu} \mathbb{1}, \quad (\text{A.6})$$

and the matrix γ^5 is given by

$$\gamma^5 = \gamma^0 \gamma^1 \gamma^2 \gamma^3 = \begin{pmatrix} \mathbb{1} & 0 \\ 0 & -\mathbb{1} \end{pmatrix}. \quad (\text{A.7})$$

A.3 Fourier transform and functional calculus

For the momentum space representations of bosonic and fermionic fields we use

$$\phi(x) = \int \frac{d^4 p}{(2\pi)^4} \phi(p) e^{ipx}, \quad (\text{A.8})$$

$$\psi(x) = \int \frac{d^4 p}{(2\pi)^4} \psi(p) e^{ipx}, \quad (\text{A.9})$$

$$\bar{\psi}(x) = \int \frac{d^4 p}{(2\pi)^4} \bar{\psi}(p) e^{-ipx}. \quad (\text{A.10})$$

Analogously, the representations in position space are given by

$$\phi(p) = \int d^4 x \phi(x) e^{-ipx}, \quad (\text{A.11})$$

$$\psi(p) = \int d^4 x \psi(x) e^{-ipx}, \quad (\text{A.12})$$

$$\bar{\psi}(p) = \int d^4 x \bar{\psi}(x) e^{ipx}. \quad (\text{A.13})$$

A. Notation and Conventions

We note that we deviate from these definitions in Sec. 4.4, where we adopt the conventions used in [71], i.e.

$$\phi(x) = \int \frac{d^4 p}{(2\pi)^4} \phi(p) e^{-ipx}, \quad (\text{A.14})$$

$$\phi(p) = \int d^4 x \phi(x) e^{ipx}. \quad (\text{A.15})$$

Useful representations of the Dirac delta function are given by

$$\int d^4 x e^{i(p+p')x} = (2\pi)^4 \delta^{(4)}(p + p'), \quad (\text{A.16})$$

$$\int \frac{d^4 p}{(2\pi)^4} e^{ip(x+x')} = \delta^{(4)}(x + x'). \quad (\text{A.17})$$

while basic expressions for functional derivatives include

$$\frac{\delta\phi(p)}{\delta\phi(p')} = (2\pi)^4 \delta^{(4)}(p - p'), \quad (\text{A.18})$$

$$\frac{\delta\phi(x)}{\delta\phi(x')} = \delta^{(4)}(x - x'). \quad (\text{A.19})$$

B

Derivation of Flow Equations

B.1 Flow equation for the effective action

In this section, we will derive the so-called Wetterich equation which represents an exact flow equation for the effective average action Γ_k . We will first consider bosonic fields and then fermionic fields. The notation and derivations presented here are based on [19, 24, 49, 97].

B.1.1. Derivation for bosonic fields

In Euclidean quantum field theory, the generating functional $Z[J]$ for a real scalar field φ in the presence of a source $J(x)$ is given by

$$Z[J] = \int \mathcal{D}\varphi \exp \left(-S[\varphi] + \int d^4x J(x)\varphi(x) \right). \quad (\text{B.1})$$

A general correlation function or n -point function can then be obtained via functional differentiation,

$$\langle \varphi(x_1) \dots \varphi(x_n) \rangle = \frac{1}{Z[0]} \left(\frac{\delta^n Z[J]}{\delta J(x_1) \dots \delta J(x_n)} \right) \Big|_{J=0}. \quad (\text{B.2})$$

The generating functional for the connected n -point functions is given by

$$W[J] = \log Z[J]. \quad (\text{B.3})$$

In a sense, the generating functional $W[J]$ represents a more efficient way to store the physical information since it does not include disconnected graphs, which are not

B. Derivation of Flow Equations

necessary to compute, e.g., scattering amplitudes. The connected correlation functions are then generated by taking functional derivatives of $W[J]$, e.g.

$$\frac{\delta W[J]}{\delta J(x)} = \frac{1}{Z[J]} \frac{\delta Z[J]}{\delta J(x)} = \langle \varphi(x) \rangle \equiv \phi(x), \quad (\text{B.4})$$

where $\phi(x)$ is the expectation value of $\varphi(x)$ in the presence of the source $J(x)$. Analogously, we have

$$\frac{\delta^2 W[J]}{\delta J(x) \delta J(y)} = \langle \varphi(x) \varphi(y) \rangle - \langle \varphi(x) \rangle \langle \varphi(y) \rangle \equiv D(x, y), \quad (\text{B.5})$$

where $D(x, y)$ is the propagator. We now define the effective action $\Gamma[\phi]$, which generates only one-particle-irreducible (1PI) graphs and is obtained by a Legendre transform of $W[J]$,

$$\Gamma[\phi] = \sup_J \left(\int d^4x J(x) \phi(x) - W[J] \right), \quad (\text{B.6})$$

i.e. for any given $\phi(x)$, the source $J(x)$ is chosen such that a supremum is approached. By taking a functional derivative of the effective action with respect to $J(x) = J_{\text{sup}}(x)$, and using that Γ is convex by construction, we have

$$\frac{\delta}{\delta J(x)} \left(\int d^4x J(x) \phi(x) - W[J] \right) \stackrel{!}{=} 0, \quad (\text{B.7})$$

which leads to Eq. (B.4). Taking a functional derivative of $\Gamma[\phi]$ with respect to the field $\phi(x)$ leads to the quantum equation of motion,

$$\frac{\delta \Gamma[\phi]}{\delta \phi(x)} = \int d^4y \frac{\delta J(y)}{\delta \phi(x)} \phi(y) + J(x) - \int d^4y \frac{\delta W[J]}{\delta J(y)} \frac{\delta J(y)}{\delta \phi(x)} = J(x). \quad (\text{B.8})$$

We now define scale-dependent analogues of the generating functionals $Z[J]$, $W[J]$ and $\Gamma[\phi]$ as

$$Z_k[J] = \int \mathcal{D}\varphi \exp \left(-S[\varphi] - \Delta S_k[\varphi] + \int d^4x J(x) \varphi(x) \right), \quad (\text{B.9})$$

$$W_k[J] = \log \int \mathcal{D}\varphi \exp \left(-S[\varphi] - \Delta S_k[\varphi] + \int d^4x J(x) \varphi(x) \right), \quad (\text{B.10})$$

$$\Gamma_k[\phi] = \sup_J \left(\int d^4x J(x) \phi(x) - W_k[J] \right) - \Delta S_k[\phi], \quad (\text{B.11})$$

where we introduced an IR cutoff term $\Delta S_k[\phi]$ which reads in momentum space

$$\Delta S_k[\phi] = \frac{1}{2} \int \frac{d^4q}{(2\pi)^4} \phi(-q) R_k(q) \phi(q). \quad (\text{B.12})$$

Since $\Delta S_k[\phi]$ is quadratic in the fields, it acts as a mass term and suppresses low momentum modes, cf. the discussion on the regulator function R_k in Sec. 3.1. We now

B. Derivation of Flow Equations

introduce the notation

$$\tilde{\Gamma}_k[\phi] \equiv \Gamma_k[\phi] + \Delta S_k[\phi] = \int d^4x J(x)\phi(x) - W_k[J], \quad (\text{B.13})$$

where $J(x) = J_{\text{sup}}(x)$. The scale derivative of $\tilde{\Gamma}_k[\phi]$ is given by,

$$\partial_k \tilde{\Gamma}_k[\phi] = -\partial_k W_k[J] \quad (\text{B.14})$$

$$= \langle \partial_k \Delta S_k[\phi] \rangle \quad (\text{B.15})$$

$$= \left\langle \frac{1}{2} \int d^4x \int d^4y \varphi(x) \partial_k R_k(x, y) \varphi(y) \right\rangle, \quad (\text{B.16})$$

where $R_k(x, y) \equiv R_k(i\partial_x)\delta^{(4)}(x - y)$ and the expectation value $\langle \cdot \rangle$ is defined as

$$\langle A[\varphi] \rangle \equiv \frac{1}{Z_k[J]} \int \mathcal{D}\varphi A[\varphi] \exp \left(-S[\varphi] - \Delta S_k[\varphi] + \int d^4x J(x)\varphi(x) \right). \quad (\text{B.17})$$

We can express Eq. (B.14) in terms of the propagator $D(x, y)$ by using Eq. (B.4) and find

$$\partial_k \tilde{\Gamma}_k[\phi] = \frac{1}{2} \int d^4x \int d^4y (\partial_k R_k(x, y) D_k(x, y) + \phi(x) \partial_k R_k(x, y) \phi(y)) \quad (\text{B.18})$$

$$= \frac{1}{2} \text{Tr} \{ D_k \partial_k R_k \} + \partial_k \Delta S_k[\phi]. \quad (\text{B.19})$$

We now switch back to the effective average action $\Gamma_k[\phi]$ by means of Eq. (B.13) and get

$$\partial_k \Gamma_k[\phi] = \frac{1}{2} \text{Tr} \{ D_k \partial_k R_k \}. \quad (\text{B.20})$$

We note that the scale-dependent propagator is related to the second functional derivative of the effective average action,

$$\int d^4y D_k(x, y) \left(\Gamma_k^{(2)} + R_k \right) (y, z) = \delta^{(4)}(x - z), \quad (\text{B.21})$$

which follows from the following relations,

$$\tilde{\Gamma}_k^{(2)}(x, y) = \frac{\delta^2 \tilde{\Gamma}_k}{\delta \phi(x) \delta \phi(y)} = \frac{\delta J(x)}{\delta \phi(y)}, \quad (\text{B.22})$$

$$D_k(x, y) = \frac{\delta^2 W_k}{\delta J(x) \delta J(y)} = \frac{\delta \phi(x)}{\delta J(y)}. \quad (\text{B.23})$$

Finally, we arrive at the Wetterich equation for the effective average action,

$$\partial_k \Gamma_k[\phi] = \frac{1}{2} \text{Tr} \left\{ \partial_k R_k \left(\Gamma_k^{(2)}[\phi] + R_k \right)^{-1} \right\}. \quad (\text{B.24})$$

B. Derivation of Flow Equations

B.1.2. Derivation for fermionic fields

We now derive the fermionic analogue of this flow equation. As in the bosonic case, we can introduce scale-dependent generating functionals $Z_k[\bar{\eta}, \eta]$, $W_k[\bar{\eta}, \eta]$ and $\Gamma_k[\psi, \bar{\psi}]$,

$$Z_k[\bar{\eta}, \eta] = \int \mathcal{D}\bar{\Psi}\mathcal{D}\Psi \exp(-S[\bar{\Psi}, \Psi] - \Delta S_k[\bar{\Psi}, \Psi] + \langle \bar{\eta}, \Psi \rangle + \langle \bar{\Psi}, \eta \rangle), \quad (\text{B.25})$$

$$W_k[\bar{\eta}, \eta] = \log \int \mathcal{D}\bar{\Psi}\mathcal{D}\Psi \exp(-S[\bar{\Psi}, \Psi] - \Delta S_k[\bar{\Psi}, \Psi] + \langle \bar{\eta}, \Psi \rangle + \langle \bar{\Psi}, \eta \rangle), \quad (\text{B.26})$$

$$\Gamma_k[\psi, \bar{\psi}] = \langle \bar{\eta}, \psi \rangle + \langle \bar{\psi}, \eta \rangle - W_k[\bar{\eta}, \eta] - \Delta S_k[\bar{\psi}, \psi], \quad (\text{B.27})$$

where $\psi(x)$ is the expectation value of $\Psi(x)$,

$$\psi(x) \equiv \langle \Psi(x) \rangle = \frac{\delta W_k[\bar{\eta}, \eta]}{\delta \bar{\eta}(x)}, \quad (\text{B.28})$$

$$\bar{\psi}(x) \equiv \langle \bar{\Psi}(x) \rangle = -\frac{\delta W_k[\bar{\eta}, \eta]}{\delta \eta(x)}, \quad (\text{B.29})$$

and the Dirac spinors are elements of $\mathcal{H}^4 \otimes \text{SU}(N_c) \otimes \text{SU}(N_f)$, with \mathcal{H}^4 the Hilbert space of the spinor components, $\text{SU}(N_c)$ the color symmetry group and $\text{SU}(N_f)$ the flavor symmetry group. The inner product $\langle \cdot, \cdot \rangle$ is then defined by

$$\langle \bar{\psi}, \eta \rangle = \int d^4x \sum_{i=1}^4 \sum_{m=1}^{N_c} \sum_{r=1}^{N_f} \bar{\psi}_{i,m,r}(x) \eta_{i,m,r}(x), \quad (\text{B.30})$$

and the bilinear regulator term $S_k[\bar{\psi}, \psi]$ is given by

$$\Delta S_k[\bar{\psi}, \psi] = \langle \bar{\psi}, R_k \psi \rangle. \quad (\text{B.31})$$

We note that there is no factor 1/2 involved in the definition of $\Delta S_k[\bar{\psi}, \psi]$, in contrast to the bosonic case, cf. Eq. (B.12). The factor 1/2 appears only if $\eta(x)$ and $\bar{\eta}(x)$ are related, as for Majorana spinors. For Dirac spinors this factor is absent, cf. [98] for a more detailed discussion. In analogy to the bosonic case we now introduce the notation

$$\tilde{\Gamma}_k[\psi, \bar{\psi}] \equiv \Gamma_k[\psi, \bar{\psi}] + \Delta S_k[\bar{\psi}, \psi] \quad (\text{B.32})$$

B. Derivation of Flow Equations

and study the scale dependence of $\tilde{\Gamma}_k[\psi, \bar{\psi}]$. We find

$$\partial_k \tilde{\Gamma}_k[\psi, \bar{\psi}] = -\partial_k W_k[\bar{\eta}, \eta] \quad (\text{B.33})$$

$$= \langle \partial_k \Delta S_k[\bar{\Psi}, \Psi] \rangle \quad (\text{B.34})$$

$$= \left\langle \int d^4x d^4y \sum_{i,j} \sum_{m,n} \sum_{r,s} \bar{\Psi}_{i,m,r}(y) (\partial_k R_k)_{ij,mn,rs}(x,y) \Psi_{j,n,s}(x) \right\rangle \quad (\text{B.35})$$

$$= \int d^4x d^4y \sum_{i,j} \sum_{m,n} \sum_{r,s} (\partial_k R_k)_{ij,mn,rs}(x,y) \langle \bar{\Psi}_{i,m,r}(x) \Psi_{j,n,s}(y) \rangle. \quad (\text{B.36})$$

We now express Eq. (B.36) in terms of the scale-dependent fermionic propagator by using

$$D_k(x, y) \equiv \frac{\delta}{\delta \bar{\eta}_{i,m,r}(x)} W_k[\bar{\eta}, \eta] \overleftarrow{\frac{\delta}{\delta \eta_{j,n,s}(y)}} \quad (\text{B.37})$$

$$= \langle \bar{\Psi}_{j,n,s}(y) \rangle \langle \Psi_{i,m,r}(x) \rangle - \langle \bar{\Psi}_{j,n,s}(y) \Psi_{i,m,r}(x) \rangle. \quad (\text{B.38})$$

We then have

$$\partial_k \tilde{\Gamma}_k[\psi, \bar{\psi}] = -\text{Tr} \{ D_k \partial_k R_k \} + \langle \bar{\psi}, \partial_k R_k \psi \rangle \quad (\text{B.39})$$

$$= -\text{Tr} \{ D_k \partial_k R_k \} + \partial_k \Delta S_k[\psi, \bar{\psi}], \quad (\text{B.40})$$

and finally, after switching back to $\Gamma_k[\psi, \bar{\psi}]$ by means of Eq. (B.32) and using the fermionic analogue of Eq. (B.21), we get the following flow equation for the effective average action,

$$\partial_k \Gamma_k[\psi, \bar{\psi}] = -\text{Tr} \left\{ \partial_k R_k \left(\Gamma_k^{(1,1)} + R_k \right)^{-1} \right\}. \quad (\text{B.41})$$

B.2 Flow equation for the effective potential of the quark-meson model

In the case of the quark-meson model, the effective action depends on bosonic as well as fermionic fields. The corresponding flow equation can be obtained by combining Eq. (B.24) and Eq. (B.41), which yields

$$\begin{aligned} \partial_k \Gamma_k[\phi, \psi, \bar{\psi}] &= \frac{1}{2} \text{Tr} \left\{ \partial_k R_k^B \left(\Gamma_k^{(2,0,0)}[\phi, \psi, \bar{\psi}] + R_k^B \right)^{-1} \right\} \\ &\quad - \text{Tr} \left\{ \partial_k R_k^F \left(\Gamma_k^{(0,1,1)}[\phi, \psi, \bar{\psi}] + R_k^F \right)^{-1} \right\}. \end{aligned} \quad (\text{B.42})$$

B. Derivation of Flow Equations

As discussed in Sec. 3.2, we employ the following truncation for the Euclidean effective average action of the quark-meson model

$$\Gamma_k[\phi, \psi, \bar{\psi}] = \int d^4x \left\{ \bar{\psi} (\gamma_\mu \partial^\mu - \mu \gamma^0 + h(\sigma + i\vec{\tau}\vec{\pi}\gamma_5)) \psi + \frac{1}{2}(\partial_\mu \sigma)^2 + \frac{1}{2}(\partial_\mu \vec{\pi})^2 + U_k(\phi^2) - c\sigma \right\}. \quad (\text{B.43})$$

In the following two sections, we will derive the bosonic and the fermionic contributions to the flow equation for the effective potential $U_k(\phi^2)$.

B.2.1. Bosonic contribution

By inserting Eq. (B.43) into the left-hand side of Eq. (B.42) and assuming that the fields are spatially homogeneous, we find

$$\partial_k U_k(\phi^2) = \frac{1}{2\Omega} \text{Tr} \left\{ \partial_k R_k^B \left(\frac{\delta^2 \Gamma_k[\phi, \psi, \bar{\psi}]}{\delta \phi_j \delta \phi_i} + R_k^B \right)_{q,-q}^{-1} \right\}, \quad (\text{B.44})$$

where $\Omega = \int d^4x$ is an infinite volume factor. In order to calculate the second functional derivative of the effective action, we first switch to momentum space, cf. App. A, and get for the bosonic part of the effective action,

$$\Gamma_k[\phi] = \int \frac{d^4p}{(2\pi)^4} \left(\frac{1}{2} p^2 \phi(p) \phi(-p) + U_k(\phi(p) \phi(-p)) \right). \quad (\text{B.45})$$

The first functional derivative of $\Gamma_k^B[\phi]$ is then given by

$$\frac{\delta \Gamma_k[\phi]}{\delta \phi_i(q)} = q^2 \phi_i(-q) + 2U'_k(\phi^2) \phi_i(-q), \quad (\text{B.46})$$

and the second functional derivative by

$$\frac{\delta^2 \Gamma_k[\phi]}{\delta \phi_j(q') \delta \phi_i(q)} = (q^2 \delta_{ij} + 2U'_k(\phi^2) \delta_{ij} + 4U''_k(\phi^2) \phi_i(-q) \phi_j(-q')) (2\pi)^4 \delta^{(4)}(q + q'). \quad (\text{B.47})$$

We now set the fields to their expectation values, i.e. $\phi = (\sigma, 0, 0, 0)$, and get in matrix form

$$\frac{\delta^2 \Gamma_k[\phi]}{\delta \phi_j(q') \delta \phi_i(q)} = \begin{pmatrix} q^2 + 2U'_k + 4U''_k \sigma^2 & 0 & 0 & 0 \\ 0 & q^2 + 2U'_k & 0 & 0 \\ 0 & 0 & q^2 + 2U'_k & 0 \\ 0 & 0 & 0 & q^2 + 2U'_k \end{pmatrix} (2\pi)^4 \delta^{(4)}(q + q'). \quad (\text{B.48})$$

B. Derivation of Flow Equations

Inserting Eq. (B.47) into Eq. (B.44) then yields for the flow equation of the effective potential

$$\partial_k U_k = \frac{1}{2\Omega} \text{Tr} \left\{ \partial_k R_k^B \left((q^2 \delta_{ij} + 2U'_k \delta_{ij} + 4U''_k \phi_i(-q) \phi_j(q)) (2\pi)^4 \delta^{(4)}(0) + R_k^B \right)^{-1} \right\}. \quad (\text{B.49})$$

where the regulator function is given by

$$R_k^B(q, q') = (2\pi)^4 \delta^{(4)}(q + q') R_k^B(q), \quad (\text{B.50})$$

with $q' = -q$ in our case. We now want to move the Dirac delta functions from the denominator to the numerator. This is straightforward since the Dirac delta function is basically its own inverse. In order to see that, we use the following expansion of the inverse of the effective action,

$$\Gamma_k^{-1}[\phi] = \frac{1}{2} \int \frac{d^4 q}{(2\pi)^4} \int \frac{d^4 q'}{(2\pi)^4} \phi(q') \left(\Gamma^{(2)}(q, q') \right)^{-1} \phi(q) \quad (\text{B.51})$$

$$= \frac{1}{2} \int \frac{d^4 q}{(2\pi)^4} \phi(-q) \left(\Gamma^{(2)}(q) \right)^{-1} \phi(q), \quad (\text{B.52})$$

where the inverse of $\Gamma^{(2)}(q)$ is simply given by $1/\Gamma^{(2)}(q)$. We can therefore write the inverse of $\Gamma^{(2)}(q, q')$ as

$$\left(\Gamma^{(2)}(q, q') \right)^{-1} = \frac{1}{\Gamma^{(2)}(q)} (2\pi)^4 \delta^{(4)}(q + q'). \quad (\text{B.53})$$

Using Eq. (B.53) and an analogue expression for the inverse of the regulator function $R_k^B(q, q')$ allows us to move the Dirac delta functions in Eq. (B.49) from the denominator to the numerator, such that they cancel with the volume factor $\Omega = (2\pi)^4 \delta^{(4)}(0)$. The flow equation for the effective potential is then given by

$$\partial_k U_k = \frac{1}{2} \int \frac{d^4 q}{(2\pi)^4} \partial_k R_k^B(q) \left(\frac{1}{q^2 + 4U''_k \sigma^2 + 2U'_k + R_k^B(q)} + \frac{3}{q^2 + 2U'_k + R_k^B(q)} \right). \quad (\text{B.54})$$

We now introduce a finite temperature T by employing the Matsubara formalism, see e.g. [30, 71]. The bosonic fields then satisfy periodic boundary conditions in the Euclidean time direction and the possible energies are given by the discrete Matsubara frequencies, $q_n = 2\pi nT$, where n is an integer. As a consequence, the integration over energy is replaced by a summation over Matsubara modes,

$$\int \frac{d^4 q}{(2\pi)^4} \rightarrow T \sum_{n \in \mathbb{Z}} \int \frac{d^3 q}{(2\pi)^3}. \quad (\text{B.55})$$

B. Derivation of Flow Equations

In order to be able to perform the Matsubara summation explicitly, we use a three-dimensional regulator function which does not affect the frequency component of the internal 4-momentum, cf. Eq. (3.2). We then get

$$\partial_k U_k = T \sum_{n \in \mathbb{Z}} \int \frac{d^3 q}{(2\pi)^3} \left(\frac{1}{q_0^2 + E_{k,\sigma}^2} + \frac{3}{q_0^2 + E_{k,\pi}^2} \right) \theta(k^2 - \vec{q}^2), \quad (\text{B.56})$$

where we introduced the notation

$$E_{k,\sigma}^2 = k^2 + 4U_k'' \sigma^2 + 2U_k', \quad (\text{B.57})$$

$$E_{k,\pi}^2 = k^2 + 2U_k'. \quad (\text{B.58})$$

The integration over the internal 3-momentum as well as the summation over the Matsubara modes can now be performed analytically, which yields for the bosonic part of the flow equation for the effective potential,

$$\partial_k U_k = \frac{k^4}{12\pi^2} \left(\frac{1}{E_{k,\sigma}} \coth \left(\frac{E_{k,\sigma}}{2T} \right) + \frac{3}{E_{k,\pi}} \coth \left(\frac{E_{k,\pi}}{2T} \right) \right). \quad (\text{B.59})$$

B.2.2. Fermionic contribution

In order to derive the fermionic contribution to the flow equation for the effective potential, we also start by inserting Eq. (B.43) into the left-hand side of Eq. (B.42) and get

$$\partial_k U_k(\phi^2) = -\frac{1}{\Omega} \text{Tr} \left\{ \partial_k R_k^F \left(\frac{\delta^2 \Gamma_k[\phi, \psi, \bar{\psi}]}{\delta\psi\delta\bar{\psi}} + R_k^F \right)_{q,-q}^{-1} \right\}. \quad (\text{B.60})$$

In momentum space, the fermionic part of the effective action can be expressed as

$$\Gamma_k^F[\phi, \psi, \bar{\psi}] = \int \frac{d^4 p}{(2\pi)^4} \bar{\psi}(-p) (i\not{p} + h(\sigma + i\vec{\tau}\vec{\pi}\gamma^5) - \mu\gamma_0) \psi(p), \quad (\text{B.61})$$

where we used the notation $\not{p} = \gamma_\mu p^\mu$. The second functional derivative of $\Gamma_k^F[\phi, \psi, \bar{\psi}]$ with respect to the Dirac spinors is then given by

$$\frac{\delta^2 \Gamma_k^F[\phi, \psi, \bar{\psi}]}{\delta\psi(q')\delta\bar{\psi}(q)} = (i\not{p} + h(\sigma + i\vec{\tau}\vec{\pi}\gamma^5) - \mu\gamma_0) (2\pi)^4 \delta^{(4)}(q + q'). \quad (\text{B.62})$$

Inserting Eq. (B.62) into Eq. (B.60) and setting the bosonic fields to their expectation values yields

$$\partial_k U_k(\phi^2) = -\frac{1}{\Omega} \text{Tr} \left\{ \partial_k R_k^F \left((i\not{p} + h\sigma - \mu\gamma_0) (2\pi)^4 \delta^{(4)}(0) + R_k^F \right)^{-1} \right\}, \quad (\text{B.63})$$

B. Derivation of Flow Equations

where the regulator function is given by

$$R_k^F(q, q') = (2\pi)^4 \delta^{(4)}(q + q') R_k^F(q), \quad (\text{B.64})$$

with $q' = -q$. As in the bosonic case, the Dirac delta functions cancel with the volume factor Ω in Eq. (B.63). We now insert the explicit expression for the fermionic regulator function $R_k^F(q)$, as given by Eq. (3.2), and get

$$\partial_k U_k(\phi^2) = -N_c N_f \int \frac{d^4 q}{(2\pi)^4} \frac{4}{k^2 + (q_0 + i\mu)^2 + h^2 \sigma^2} \theta(k^2 - \vec{q}^2), \quad (\text{B.65})$$

where we evaluated the traces over Dirac, color and flavor space. Temperature is again introduced via the Matsubara formalism, where the fermionic fields now satisfy antiperiodic boundary conditions in the Euclidean time direction. Consequently, the discrete Matsubara frequencies are given by $q_n = (2n + 1)\pi T$ and the integration over energy is replaced by a summation over Matsubara modes,

$$\int \frac{d^4 q}{(2\pi)^4} \rightarrow -T \sum_{n \in \mathbb{Z}} \int \frac{d^3 q}{(2\pi)^3}. \quad (\text{B.66})$$

The Matsubara summation as well as the integration over the spatial loop momentum can be carried out analytically, which gives the following expression for the fermionic contribution to the flow equation of the effective potential,

$$\partial_k U_k(\phi^2) = \frac{k^4}{12\pi^2} \left\{ -\frac{2N_c N_f}{E_{q,k}} \left(\tanh\left(\frac{E_{\psi,k} - \mu}{2T}\right) + \tanh\left(\frac{E_{\psi,k} + \mu}{2T}\right) \right) \right\}, \quad (\text{B.67})$$

where we used the notation

$$E_{\psi,k}^2 = k^2 + h^2 \sigma^2. \quad (\text{B.68})$$

By combining the result for the bosonic part, Eq. (B.59), and the fermionic part, Eq. (B.67), we arrive at the full flow equation for the effective potential, as given by Eq. (3.9).



Threshold Functions

In this section, we provide explicit expressions for the threshold or loop functions $I_{k,\alpha}$, which appear in the flow equations for the effective potential, Eq. (3.13), and $J_{k,\alpha\beta}(p)$, which appear in the flow equations for the mesonic two-point functions, cf. Eqs. (3.23)-(3.24), cf. also Eqs. (3.25)-(3.26) for their definitions. Moreover, explicit expressions for the mesonic vertex functions, defined by Eqs. (3.21)-(3.22), are listed. Wherever necessary, the three-dimensional regulator functions given by Eqs. (3.2)-(3.3) are used.

The bosonic threshold functions $I_{k,\alpha}^{(1)}(E_{k,\alpha})$ and $I_{k,\alpha}^{(2)}(E_{k,\alpha})$ are given by

$$I_{k,\alpha}^{(1)}(E_{k,\alpha}) = \frac{k^4}{6\pi^2} \frac{1 + 2n_B(E_{k,\alpha})}{E_{k,\alpha}}, \quad (\text{C.1})$$

$$I_{k,\alpha}^{(2)}(E_{k,\alpha}) = \frac{k^4}{6\pi^2} \left(\frac{1 + 2n_B(E_{k,\alpha})}{2E_{k,\alpha}^3} - \frac{n'_B(E_{k,\alpha})}{E_{k,\alpha}^2} \right), \quad (\text{C.2})$$

with $\alpha \in \{\pi, \sigma\}$, while the fermionic threshold function $I_{k,\psi}^{(1)}(E_{k,\psi})$ can be written as

$$I_{k,\psi}^{(1)}(E_{k,\psi}) = \frac{k^4}{3\pi^2} \frac{1 - n_F(E_{k,\psi} - \mu) - n_F(E_{k,\psi} + \mu)}{E_{k,\psi}}, \quad (\text{C.3})$$

where the bosonic and fermionic occupation numbers are given by

$$n_B(E) \equiv \frac{1}{e^{E/T} - 1}, \quad n_F(E) \equiv \frac{1}{e^{E/T} + 1}. \quad (\text{C.4})$$

The effective quasi-particle energies read

$$E_{k,\alpha} \equiv \sqrt{k^2 + m_{k,\alpha}^2}, \quad \alpha \in \{\pi, \sigma, \psi\}, \quad (\text{C.5})$$

C. Threshold Functions

where the effective meson masses and the quark mass are given by

$$m_{k,\pi}^2 = 2U'_k, \quad m_{k,\sigma}^2 = 2U'_k + 4U''_k \phi^2, \quad m_\psi^2 = h^2 \phi^2, \quad (\text{C.6})$$

with primes denoting derivatives with respect to ϕ^2 . We note that the terms “effective energy” and “effective mass” have to be treated with care. Since the flow equation of the effective potential is solved on a grid in field space, see also Sec. 6.1, the field variable ϕ^2 can take on different values. The (scale-dependent) effective particle masses are then only given by Eq. (C.6), when ϕ refers to the position of the global minimum of the effective potential.

The mesonic vertex functions, which are defined by Eqs. (3.21)-(3.22), read explicitly

$$\Gamma_{k,\sigma\sigma\sigma}^{(3)} = 12U''_k \phi + 8U_k^{(3)} \phi^3, \quad (\text{C.7})$$

$$\Gamma_{k,\sigma\pi\pi}^{(3)} = 4U''_k \phi, \quad (\text{C.8})$$

$$\Gamma_{k,\sigma\sigma\sigma\sigma}^{(4)} = 12U''_k + 48U_k^{(3)} \phi^2 + 16U_k^{(4)} \phi^4, \quad (\text{C.9})$$

$$\Gamma_{k,\pi\pi\tilde{\pi}\tilde{\pi}}^{(4)} = 4U''_k, \quad (\text{C.10})$$

$$\Gamma_{k,\pi\pi\pi\pi}^{(4)} = 12U''_k, \quad (\text{C.11})$$

$$\Gamma_{k,\sigma\sigma\pi\pi}^{(4)} = 4U''_k + 8U_k^{(3)} \phi^2, \quad (\text{C.12})$$

with $\pi, \tilde{\pi} \in \{\pi_1, \pi_2, \pi_3\}$ and $\pi \neq \tilde{\pi}$.

We now turn to the bosonic and fermionic loop functions, $J_{k,\alpha\beta}(p)$ and $J_{k,\bar{\psi}\psi}^{(\alpha)}(p)$, as defined by Eqs. (3.25)-(3.26). Due to the appearance of the three-dimensional regulator functions in these equations, we have to deal with theta functions of the form

$$\theta(k^2 - (\vec{q} + \vec{p})^2) = \begin{cases} 1, & |\vec{q} + \vec{p}| \leq k \\ 0, & |\vec{q} + \vec{p}| > k \end{cases}, \quad (\text{C.13})$$

and

$$\theta(k^2 - \vec{q}^2) = \begin{cases} 1, & |\vec{q}| \leq k \\ 0, & |\vec{q}| > k \end{cases}, \quad (\text{C.14})$$

where \vec{q} is the internal loop momentum and \vec{p} the external momentum. Since the external momentum is always routed through the legs of the loops which contain the regulator insertion $\partial_k R_k$, cf. Fig. 3.3 and the discussion in Sec. 3.3, the theta function given by Eq. (C.13) always appears in the “upper” legs of the loops, while the theta function given by Eq. (C.14) always appears in the “lower” legs.

As a consequence of the theta function that appears in the regulator insertion $\partial_k R_k$, the integration over the internal loop momentum, cf. Sec. 3.3, is modified in the following way,

$$\int_{-\infty}^{\infty} d^3q \theta(k^2 - (\vec{q} + \vec{p})^2) \rightarrow \int_{-k-|\vec{p}|}^{k-|\vec{p}|} dq_{\parallel} \int_0^{\sqrt{k^2 - (q_{\parallel} + |\vec{p}|)^2}} d^2q_{\perp}, \quad (\text{C.15})$$

C. Threshold Functions

where q_{\parallel} is chosen to be parallel to \vec{p} , while the perpendicular components are denoted by q_{\perp} . The integration regime of the internal loop momentum is therefore given by a sphere with radius k whose center has been shifted by $-|\vec{p}|$, cf. Fig. C.1. The left circle in Fig. C.1 then represents the integration regime given by Eq. (C.15), where within the lighter shaded area we have $|\vec{q}| > k$ and within the darker shaded area the internal loop momentum is smaller than the RG scale, i.e. $|\vec{q}| \leq k$.

We conclude that the theta function given by Eq. (C.13), which is connected to the upper legs of the loops, is always non-vanishing since we always have $|\vec{q} + \vec{p}| \leq k$ within the integration regime of the internal momentum, cf. Fig. C.1. The theta function given by Eq. (C.14) can, on the other hand, assume both possible values. We will therefore evaluate the loop functions once for a momentum configurations with $|\vec{q}| \leq k$ and once for $|\vec{q}| > k$.

For momentum configurations with $|\vec{q}| \leq k$, the bosonic loop functions, $J_{k,\alpha\beta}(p)$, are given by Eq. (C.22), where we note that the RG-scale index k of the energies $E_{k,\alpha}$ has been omitted in Eqs. (C.21)-(C.26) for simplicity and that p_0 has to be replaced by $-i(\omega + i\epsilon)$ in order to obtain the retarded expressions, cf. Eq. (4.13). Moreover, the index $\alpha \in \{\sigma, \pi\}$ always represents the particle associated with the upper leg of the loops, i.e. the one with the regulator insertion, and $\beta \in \{\sigma, \pi\}$ always represents the particle associated with the lower leg of the loops, i.e. the one without regulator insertion.

For momentum configurations with $|\vec{q}| > k$, the bosonic loop functions are denoted by $\tilde{J}_{k,\alpha\beta}(p)$ and are obtained by carrying out the following substitution in Eq. (C.22),

$$\tilde{J}_{k,\alpha\beta} \equiv J_{k,\alpha\beta} \left(E_{\beta} \rightarrow \tilde{E}_{\beta} \equiv \sqrt{E_{\beta}^2 - k^2 + \vec{q}^2} \right). \quad (\text{C.16})$$

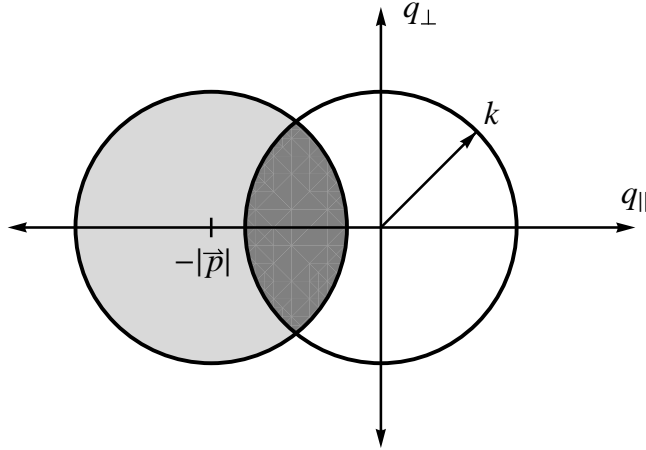


Figure C.1.: The integration regime of the internal loop momentum \vec{q} is represented by the left circle which has been shifted by $-|\vec{p}|$, cf. Eq. (C.15). The lighter shaded area refers to the case $|\vec{q}| > k$, while within the darker shaded area we have $|\vec{q}| \leq k$.

C. Threshold Functions

Similarly, the fermionic loop function for the pion two-point function, $J_{k,\bar{\psi}\psi}^{(\pi)}(p)$, is, for momentum configurations with $|\vec{q}| \leq k$, given by Eq. (C.23), where

$$\cos \varphi \equiv \frac{\vec{q} \cdot (\vec{q} + \vec{p})}{|\vec{q}||\vec{q} + \vec{p}|}. \quad (\text{C.17})$$

The corresponding expression for the sigma two-point function can be written as

$$J_{k,\bar{\psi}\psi}^{(\sigma)}(p) \equiv J_{k,\bar{\psi}\psi}^{(\pi)}(p) + \Delta J_{k,\bar{\psi}\psi}(p), \quad (\text{C.18})$$

where $\Delta J_{k,\bar{\psi}\psi}(p)$ is given by Eq. (C.24).

For momentum configurations with $|\vec{q}| > k$, the fermionic loop function for the pion two-point function, $\tilde{J}_{k,\bar{\psi}\psi}^{(\pi)}(p)$, is given by Eq. (C.25). The corresponding expression for the sigma two-point function can be obtained as

$$\tilde{J}_{k,\bar{\psi}\psi}^{(\sigma)}(p) \equiv \tilde{J}_{k,\bar{\psi}\psi}^{(\pi)}(p) + \Delta \tilde{J}_{k,\bar{\psi}\psi}(p), \quad (\text{C.19})$$

where $\Delta \tilde{J}_{k,\bar{\psi}\psi}(p)$ is given by Eq. (C.26) with

$$\tilde{E}_\psi \equiv \sqrt{E_\psi^2 - k^2 + \vec{q}^2}. \quad (\text{C.20})$$

We note that the different contributions to the bosonic and fermionic loop functions can be interpreted in terms of particle creation and annihilation processes. As a simple example we discuss the bosonic loop function $J_{k,\pi\pi}(p)$ which contributes to the sigma two-point function. The explicit expression of $J_{k,\pi\pi}(p)$ can be worked out by using Eq. (C.22) and is given by Eq. (C.21).

Therein, the term $(1 + n_B(E_\pi))(1 + n_B(E_\pi))$ represents the statistical weight factor for the direct process $\sigma^* \rightarrow \pi + \pi$, whereas the term $n_B(E_\pi)n_B(E_\pi)$ represents the statistical weight factor for the inverse process $\pi + \pi \rightarrow \sigma^*$, which is only possible at finite temperature since real particles from the heat bath are needed. Similarly, the term $n_B(E_\pi)(1 + n_B(E_\pi))$ represents the weight factor for the processes $\sigma^* + \pi \rightarrow \pi$ and $\pi \rightarrow \sigma^* + \pi$ which are both only possible at finite temperature. We note that, when calculating the imaginary part of the loop functions explicitly and taking the limit $\epsilon \rightarrow 0$, the fractional expressions collapse to Dirac delta-functions like $\delta(\omega - 2E_\pi)$, see e.g. [31] for a more detailed discussion.

For the fermionic loop functions the statistical factors have the form $(1 - n_F(E_\psi))$, representing the fact that there are real fermions in the heat bath, which gives rise to Pauli blocking and to a suppression of the available density of states for the decay products.

C. Threshold Functions

$$\begin{aligned}
J_{k,\pi\pi}(p) = \frac{k}{2} & \left(((1 + n_B(E_\pi))(1 + n_B(E_\pi)) - n_B(E_\pi)n_B(E_\pi)) \frac{12E_\pi^2 + p_0^2}{E_\pi^3(4E_\pi^2 + p_0^2)^2} \right. \\
& + n_B(E_\pi)(1 + n_B(E_\pi)) \frac{1}{E_\pi^2(E_\pi^2 - (E_\pi - ip_0)^2)T} \\
& \left. + n_B(E_\pi)(1 + n_B(E_\pi)) \frac{1}{E_\pi^2(E_\pi^2 - (E_\pi + ip_0)^2)T} \right) \quad (C.21)
\end{aligned}$$

$$\begin{aligned}
J_{k,\alpha\beta}(p) = \frac{k}{2} & \left((1 + n_B(E_\alpha)) \frac{E_\alpha^2 + E_\beta^2 - (2E_\alpha + ip_0)^2}{E_\alpha^3(E_\beta^2 - (E_\alpha + ip_0)^2)^2} + n_B(E_\alpha) \frac{E_\alpha^2 + E_\beta^2 - (2E_\alpha - ip_0)^2}{E_\alpha^3(E_\beta^2 - (E_\alpha - ip_0)^2)^2} \right. \\
& + (1 + n_B(E_\beta)) \frac{2}{E_\beta(E_\alpha^2 - (E_\beta - ip_0)^2)^2} + n_B(E_\beta) \frac{2}{E_\beta(E_\alpha^2 - (E_\beta + ip_0)^2)^2} \\
& + n_B(E_\alpha)(1 + n_B(E_\alpha)) \frac{1}{E_\alpha^2(E_\beta^2 - (E_\alpha - ip_0)^2)T} \\
& \left. + n_B(E_\alpha)(1 + n_B(E_\alpha)) \frac{1}{E_\alpha^2(E_\beta^2 - (E_\alpha + ip_0)^2)T} \right) \quad (C.22)
\end{aligned}$$

$$\begin{aligned}
J_{k,\bar{\psi}\psi}^{(\pi)}(p) = -2h^2k & \left((1 - n_F(E_\psi - \mu)) \frac{16E_\psi^4 - 2E_\psi^2(4E_\psi^2 + p_0^2) \cos \varphi - k^2(12E_\psi^2 + p_0^2)(1 - \cos \varphi)}{E_\psi^3(4E_\psi^2 + p_0^2)^2} \right. \\
& - n_F(E_\psi + \mu) \frac{8E_\psi^4(2 - \cos \varphi) + 2E_\psi^2((6k^2 - p_0^2) \cos \varphi - 6k^2) - k^2p_0^2(1 - \cos \varphi)}{E_\psi^3(4E_\psi^2 + p_0^2)^2} \\
& - n_F(E_\psi - \mu)(1 - n_F(E_\psi - \mu)) \frac{k^2(1 - \cos \varphi) + ip_0E_\psi}{ip_0E_\psi^2(2E_\psi + ip_0)T} \\
& \left. + n_F(E_\psi + \mu)(1 - n_F(E_\psi + \mu)) \frac{k^2(1 - \cos \varphi) - ip_0E_\psi}{ip_0E_\psi^2(2E_\psi - ip_0)T} \right) \quad (C.23)
\end{aligned}$$

$$\begin{aligned}
\Delta J_{k,\bar{\psi}\psi}(p) = 4m_\psi^2 h^2 k & \left((1 - n_F(E_\psi - \mu)) \frac{12E_\psi^2 + p_0^2}{E_\psi^3(4E_\psi^2 + p_0^2)^2} - n_F(E_\psi + \mu) \frac{12E_\psi^2 + p_0^2}{E_\psi^3(4E_\psi^2 + p_0^2)^2} \right. \\
& + n_F(E_\psi - \mu)(1 - n_F(E_\psi - \mu)) \frac{1}{ip_0E_\psi^2(2E_\psi + ip_0)T} \\
& \left. - n_F(E_\psi + \mu)(1 - n_F(E_\psi + \mu)) \frac{1}{ip_0E_\psi^2(2E_\psi - ip_0)T} \right) \quad (C.24)
\end{aligned}$$

C. Threshold Functions

$$\begin{aligned}
\tilde{J}_{k,\tilde{\psi}\psi}^{(\pi)}(p) = & -2h^2k \left[(1 - n_F(E_\psi - \mu)) \left(\frac{2ip_0 E_\psi^3 (|\tilde{q}| \cos \varphi - k) + 4ip_0 E_\psi k^2 (k - |\tilde{q}| \cos \varphi)}{E_\psi^3 k (E_\psi^2 - k^2 - (E_\psi + ip_0)^2 + \tilde{q}^2)^2} \right. \right. \\
& - \frac{k^2 (p_0^2 - k^2 + \tilde{q}^2) (k - |\tilde{q}| \cos \varphi) + E_\psi^2 |\tilde{q}| ((k^2 + p_0^2 + \tilde{q}^2) \cos \varphi - 2k|\tilde{q}|)}{E_\psi^3 k (E_\psi^2 - k^2 - (E_\psi + ip_0)^2 + \tilde{q}^2)^2} \left. \right) \\
& + n_F(E_\psi + \mu) \left(\frac{2ip_0 E_\psi^3 (|\tilde{q}| \cos \varphi - k) + 4ip_0 E_\psi k^2 (k - |\tilde{q}| \cos \varphi)}{E_\psi^3 k (E_\psi^2 - k^2 - (E_\psi - ip_0)^2 + \tilde{q}^2)^2} \right. \\
& + \frac{k^2 (p_0^2 - k^2 + \tilde{q}^2) (k - |\tilde{q}| \cos \varphi) + E_\psi^2 |\tilde{q}| ((k^2 + p_0^2 + \tilde{q}^2) \cos \varphi - 2k|\tilde{q}|)}{E_\psi^3 k (E_\psi^2 - k^2 - (E_\psi - ip_0)^2 + \tilde{q}^2)^2} \left. \right) \\
& + n_F(E_\psi - \mu) (1 - n_F(E_\psi - \mu)) \frac{k(k - |\tilde{q}| \cos \varphi) + ip_0 E_\psi}{E_\psi^2 (E_\psi^2 - k^2 - (E_\psi + ip_0)^2 + \tilde{q}^2) T} \\
& + n_F(E_\psi + \mu) (1 - n_F(E_\psi + \mu)) \frac{k(k - |\tilde{q}| \cos \varphi) - ip_0 E_\psi}{E_\psi^2 (E_\psi^2 - k^2 - (E_\psi - ip_0)^2 + \tilde{q}^2) T} \\
& + (1 - n_F(\tilde{E}_\psi - \mu)) \frac{|\tilde{q}| \cos \varphi (k^2 - p_0^2 + \tilde{q}^2 - 2ip_0 \tilde{E}_\psi) - 2k(\tilde{q}^2 - ip_0 \tilde{E}_\psi)}{k \tilde{E}_\psi (E_\psi^2 - (\tilde{E}_\psi - ip_0)^2)^2} \\
& \left. - n_F(\tilde{E}_\psi + \mu) \frac{|\tilde{q}| \cos \varphi (k^2 - p_0^2 + \tilde{q}^2 + 2ip_0 \tilde{E}_\psi) - 2k(\tilde{q}^2 + ip_0 \tilde{E}_\psi)}{k \tilde{E}_\psi (E_\psi^2 - (\tilde{E}_\psi + ip_0)^2)^2} \right] \tag{C.25}
\end{aligned}$$

$$\begin{aligned}
\Delta \tilde{J}_{k,\tilde{\psi}\psi}(p) = & 4m_\psi^2 h^2 k \left((1 - n_F(E_\psi - \mu)) \frac{(2E_\psi - ip_0)^2 - 6E_\psi^2 - k^2 + 2p_0^2 + \tilde{q}^2}{E_\psi^3 (E_\psi^2 - k^2 - (E_\psi + ip_0)^2 + \tilde{q}^2)^2} \right. \\
& - n_F(E_\psi + \mu) \frac{(2E_\psi + ip_0)^2 - 6E_\psi^2 - k^2 + 2p_0^2 + \tilde{q}^2}{E_\psi^3 (E_\psi^2 - k^2 - (E_\psi - ip_0)^2 + \tilde{q}^2)^2} \\
& - n_F(E_\psi - \mu) (1 - n_F(E_\psi - \mu)) \frac{1}{E_\psi^2 (E_\psi^2 - k^2 - (E_\psi + ip_0)^2 + \tilde{q}^2) T} \\
& - n_F(E_\psi + \mu) (1 - n_F(E_\psi + \mu)) \frac{1}{E_\psi^2 (E_\psi^2 - k^2 - (E_\psi - ip_0)^2 + \tilde{q}^2) T} \\
& + (1 - n_F(\tilde{E}_\psi - \mu)) \frac{2}{\tilde{E}_\psi (E_\psi^2 - (\tilde{E}_\psi - ip_0)^2)^2} \\
& \left. - n_F(\tilde{E}_\psi + \mu) \frac{2}{\tilde{E}_\psi (E_\psi^2 - (\tilde{E}_\psi + ip_0)^2)^2} \right) \tag{C.26}
\end{aligned}$$

D

Derivation of the Green-Kubo Formula for the Shear Viscosity

In the following, we present a simple derivation of the Green-Kubo formula for the shear viscosity within the linear response framework, based on [79]. For a more rigorous discussion we refer to [99, 100].

We start by considering a system that is described by a time-independent Hamiltonian \hat{H}_0 , to which we add a small perturbation $\hat{V}(t)$, with $\hat{V}(t) = 0$ for $t \leq 0$, see also [30]. The variation of the mean value of an operator $\hat{O}(t)$ in the Schrödinger picture due to the perturbation $\hat{V}(t)$ is then, to linear order, given by

$$\delta\langle\hat{O}(t)\rangle \equiv \langle\Psi(t)|\hat{O}(t)|\Psi(t)\rangle - \langle\Psi^{(0)}(t)|\hat{O}(t)|\Psi^{(0)}(t)\rangle \quad (\text{D.1})$$

$$= -i \int_0^\infty dt' \langle\Psi^{(0)}(0)|\theta(t-t')[\hat{O}_H(t), \hat{V}_H(t')]|\Psi^{(0)}(0)\rangle, \quad (\text{D.2})$$

where $|\Psi^{(0)}(0)\rangle$ denotes the state of the system at $t = 0$, $|\Psi^{(0)}(t)\rangle \equiv e^{-i\hat{H}_0 t}|\Psi^{(0)}(0)\rangle$, $|\Psi(t)\rangle \equiv e^{-i\hat{H}t}|\Psi^{(0)}(0)\rangle$, and $\hat{O}_H(t) \equiv e^{i\hat{H}_0 t}\hat{O}(t)e^{-i\hat{H}_0 t}$. This result is also valid if we consider thermal averages $\langle\cdot\rangle_T$. In general, we can write, omitting the hats,

$$\delta\langle O(x)\rangle = -i \int d^4x' \theta(t-t') \langle [O(x), V(x')] \rangle. \quad (\text{D.3})$$

In order to obtain the desired Green-Kubo formula for the shear viscosity, we have to find an appropriate expression for the perturbation $V(x)$. Since the shear viscosity of a fluid expresses its resistance to shearing flows, where adjacent layers of the fluid move at different velocities, we write the fluid velocity around some point x_0 as

$$U^i(x) = x^j \partial_j U^i(x_0), \quad (\text{D.4})$$

D. Derivation of the Green-Kubo Formula for the Shear Viscosity

where we use a global reference frame that is at rest with the fluid. The change in energy density is then given by $\delta H = -U_i p^i$, where p^i is the density of momentum of the fluid. This leads to the following expression for the perturbation $V(x)$ in terms of the energy-momentum tensor,

$$V(x) = -T^{0i} x^j \partial_j U_i, \quad (\text{D.5})$$

where T^{0i} represents the momentum density, see also Ch. 5 and, e.g., [77] for an introduction to relativistic hydrodynamics.

Since we are interested in an expression for the shear viscosity in terms of correlations of the energy-momentum tensor, we use Eq. (D.3) to obtain the following expression for the variation in the expectation value of the energy-momentum tensor,

$$\delta \langle T^{ij} \rangle = i \int d^4 x' \theta(t - t') \left\langle \left[T^{ij}(x), T^{0l}(x') x'^k \partial_k U_l \right] \right\rangle. \quad (\text{D.6})$$

Integrating by parts yields

$$\delta \langle T^{ij} \rangle = -i \int d^4 x' t' \theta(t - t') \left\langle \left[T^{ij}(x), \partial_{t'} T^{0l}(x') x'^k \partial_k U_l \right] \right\rangle. \quad (\text{D.7})$$

We now use $\partial_{t'} T^{0l} = \partial_m T^{ml}$ which follows from $\partial_\mu T^{\mu\nu} = 0$ and get

$$\delta \langle T^{ij} \rangle = -i \int d^4 x' t' \theta(t - t') \left\langle \left[T^{ij}(x), \partial_m T^{ml}(x') x'^k \partial_k U_l \right] \right\rangle. \quad (\text{D.8})$$

Integrating by parts again, i.e. using

$$\int d^3 x' \partial_m T^{ml}(x') x'^k = - \int d^3 x' T^{kl}(x') \partial_m x'^m = - \int d^3 x' T^{kl}(x'), \quad (\text{D.9})$$

gives for the variation in the expectation value of the energy-momentum tensor,

$$\delta \langle T^{ij} \rangle = i \int d^4 x' t' \theta(t - t') \left\langle \left[T^{ij}(x), T^{kl}(x') \right] \right\rangle \partial_k U_l. \quad (\text{D.10})$$

In order to extract an expression for the shear viscosity, we use the following linear expansion of the energy momentum tensor which can be obtained from relativistic viscous hydrodynamics, cf. for example [79, 77],

$$T_{ij} = P \delta_{ij} + \eta \left(\partial_i U_j + \partial_j U_i + \frac{2}{3} \partial_{ij} \partial_k U^k \right) - \zeta \partial_{ij} \partial_k U^k, \quad (\text{D.11})$$

where η is the shear viscosity and ζ the bulk viscosity, see also Eq. (5.12). We now particularize to the case $\partial_k U^k = 0$ and extract the shear viscosity coefficient by comparing Eq. (D.10) and Eq. (D.11). For example, when considering an off-diagonal term like T_{12}

D. Derivation of the Green-Kubo Formula for the Shear Viscosity

one gets

$$\delta \langle T^{12} \rangle = i \int d^4 x' t' \theta(t - t') \left(\begin{aligned} & \langle [T^{12}(x), T^{11}(x')] \rangle \partial_1 U_1 + \langle [T^{12}(x), T^{12}(x')] \rangle \partial_1 U_2 + \langle [T^{12}(x), T^{13}(x')] \rangle \partial_1 U_3 \\ & + \langle [T^{12}(x), T^{21}(x')] \rangle \partial_2 U_1 + \langle [T^{12}(x), T^{22}(x')] \rangle \partial_2 U_2 + \langle [T^{12}(x), T^{23}(x')] \rangle \partial_2 U_3 \\ & + \langle [T^{12}(x), T^{31}(x')] \rangle \partial_3 U_1 + \langle [T^{12}(x), T^{32}(x')] \rangle \partial_3 U_2 + \langle [T^{12}(x), T^{33}(x')] \rangle \partial_3 U_3 \end{aligned} \right), \quad (\text{D.12})$$

from Eq. (D.10) while Eq. (D.11) yields

$$T_{12} = \eta (\partial_1 U_2 + \partial_2 U_1). \quad (\text{D.13})$$

If we treat all terms $\partial_i U_j$ in Eq. (D.10) that do not appear in the corresponding expansion of T_{ij} , given by Eq. (D.11), as higher order perturbations and use¹

$$\langle [T^{ij}(x), T^{ij}(x')] \rangle = \langle [T^{ij}(x), T^{ji}(x')] \rangle, \quad (\text{D.14})$$

we get for the shear viscosity

$$\eta = i \int d^4 x' t' \theta(t - t') \langle [T^{12}(x), T^{12}(x')] \rangle. \quad (\text{D.15})$$

If we do the same for a diagonal term like T_{11} we get

$$\eta = \frac{i}{2} \int d^4 x' t' \theta(t - t') \langle [T^{11}(x), T^{11}(x')] \rangle. \quad (\text{D.16})$$

We conclude that a diagonal correlator is given by two times an off diagonal correlator,

$$\langle [T^{ii}(x), T^{ii}(x')] \rangle = 2 \langle [T^{ij}(x), T^{ij}(x')] \rangle, \quad (\text{D.17})$$

with $i \neq j$. Therefore, the shear viscosity can be written in terms of a summation over all correlators,

$$\eta = \frac{i}{12} \int d^4 x t \theta(t) \langle [T_{ij}(x), T^{ij}(0)] \rangle, \quad (\text{D.18})$$

where we chose $t = 0$ and renamed $t' \rightarrow t$. We now evaluate the theta function using symmetry arguments,

$$\int d^4 x \theta(t) = \int dt \int d^3 x \theta(t) = \int_0^\infty dt \int d^3 x = \frac{1}{2} \int d^4 x, \quad (\text{D.19})$$

¹We note that there is no summation included in expressions like $x_i x_i$ or $x^i x^i$, cf. App. A.

D. Derivation of the Green-Kubo Formula for the Shear Viscosity

and get

$$\eta = \frac{i}{24} \int d^4x t \langle [T_{ij}(x), T^{ij}(0)] \rangle. \quad (\text{D.20})$$

In order to transform this expression to momentum space we use $t \rightarrow -i\partial_\omega$ and get

$$\eta = \frac{1}{24} \lim_{\omega \rightarrow 0^+} \lim_{|\vec{p}| \rightarrow 0^+} \frac{1}{\omega} \int d^4x e^{ipx} \langle [T_{ij}(x), T^{ij}(0)] \rangle. \quad (\text{D.21})$$

We now want to express the shear viscosity in terms of the traceless energy momentum tensor, i.e. the shear-stress tensor, which is given by

$$\pi_{ij} \equiv T_{ij} - g_{ij} T^k_k / 3. \quad (\text{D.22})$$

In order to do that, we use the following relation between the correlation functions of the energy-momentum tensor and the shear-stress tensor,

$$\langle [T_{ij}(x), T^{ij}(0)] \rangle = \frac{6}{5} \langle [\pi_{ij}(x), \pi^{ij}(0)] \rangle. \quad (\text{D.23})$$

This equation can be derived by using

$$\langle [\pi_{ii}(x), \pi_{ii}(0)] \rangle = \frac{4}{3} \langle [\pi_{ij}(x), \pi_{ij}(0)] \rangle, \quad (\text{D.24})$$

which connects the correlator of an off diagonal element of the traceless energy momentum tensor to a diagonal element. This relation can in turn be shown by writing the correlation function of the traceless shear-stress tensor as

$$\langle [\pi^{im}(x), \pi^{jn}(0)] \rangle = A(x) \delta^{im} \delta^{jn} + B(x) (\delta^{ij} \delta^{mn} + \delta^{in} \delta^{mj}), \quad (\text{D.25})$$

see also [100]. This correlator has to be traceless with respect to (im) , which means that $3A + 2B = 0$, and therefore

$$\langle [\pi^{im}(x), \pi^{jn}(0)] \rangle = B(x) \left(-\frac{2}{3} \delta^{im} \delta^{jn} + \delta^{ij} \delta^{mn} + \delta^{in} \delta^{mj} \right). \quad (\text{D.26})$$

By evaluating this expression for $i = j$ and $m = n$, once for $i = m$ and once for $i \neq m$, one finds Eq. (D.24).

In order to derive Eq. (D.23) we now use $\pi_{ij}(x) = T_{ij}(x)$ for $i \neq j$ and express the sum of the correlators of the energy-momentum tensor in terms of an off-diagonal element of the shear-stress tensor,

$$\begin{aligned} \langle [T_{ij}(x), T^{ij}(0)] \rangle &= 3 \langle [T_{ii}(x), T_{ii}(0)] \rangle + 6 \langle [T_{ij}(x), T_{ij}(0)] \rangle \\ &= 6 \langle [T_{ij}(x), T_{ij}(0)] \rangle + 6 \langle [\pi_{ij}(x), \pi_{ij}(0)] \rangle \\ &= 12 \langle [\pi_{ij}(x), \pi_{ij}(0)] \rangle. \end{aligned} \quad (\text{D.27})$$

D. Derivation of the Green-Kubo Formula for the Shear Viscosity

Analogously, the sum of the correlators of the shear-stress tensor is given by

$$\begin{aligned}
\langle [\pi_{ij}(x), \pi^{ij}(0)] \rangle &= 3\langle [\pi_{ii}(x), \pi_{ii}(0)] \rangle + 6\langle [\pi_{ij}(x), \pi_{ij}(0)] \rangle \\
&= 3\frac{4}{3}\langle [\pi_{ij}(x), \pi_{ij}(0)] \rangle + 6\langle [\pi_{ij}(x), \pi_{ij}(0)] \rangle \\
&= 10\langle [\pi_{ij}(x), \pi_{ij}(0)] \rangle,
\end{aligned} \tag{D.28}$$

where we used Eq. (D.24), cf. [101]. By combining Eq. (D.27) and Eq. (D.28), one finds Eq. (D.23),

$$\langle [T_{ij}(x), T^{ij}(0)] \rangle = \frac{12}{10}\langle [\pi_{ij}(x), \pi^{ij}(0)] \rangle = \frac{6}{5}\langle [\pi_{ij}(x), \pi^{ij}(0)] \rangle. \tag{D.29}$$

The shear viscosity can now be expressed in terms of the correlation functions of the shear-stress tensor by inserting Eq. (D.23) into Eq. (D.21),

$$\eta = \frac{1}{20} \lim_{\omega \rightarrow 0^+} \lim_{|\vec{p}| \rightarrow 0^+} \frac{1}{\omega} \int d^4x e^{ipx} \langle [\pi_{ij}(x), \pi^{ij}(0)] \rangle. \tag{D.30}$$

This equation is often referred to as the Green-Kubo formula for the shear viscosity. It can also be expressed in terms of a single off-diagonal component of the energy-momentum tensor. Using Eq. (D.28) and Eq. (D.19) we get for the static shear viscosity

$$\eta = \lim_{\omega \rightarrow 0^+} \lim_{|\vec{p}| \rightarrow 0^+} \frac{i}{\omega} \Pi^R(\omega, |\vec{p}|) \tag{D.31}$$

$$= - \lim_{\omega \rightarrow 0^+} \lim_{|\vec{p}| \rightarrow 0^+} \frac{1}{\omega} \text{Im} \Pi^R(\omega, |\vec{p}|), \tag{D.32}$$

where $\Pi^R(\omega, |\vec{p}|)$ is the retarded correlation function of the shear-stress tensor,

$$\Pi^R(\omega, |\vec{p}|) = -i \int d^4x e^{ipx} \theta(t) \langle [T_{ij}(x), T_{ij}(0)] \rangle. \tag{D.33}$$



Lorentz invariance and parameter dependence of spectral functions

E.1 Lorentz invariance

In this section, which is based on [68], we study the extent of the breaking of Lorentz or $O(4)$ invariance induced by the use of dimensionally reduced regulator functions, cf. Eqs. (3.2)-(3.3). Such three-dimensional regulator functions only regulate the spatial momentum but allow for arbitrarily large energy transfers which may give rise to a violation of Lorentz invariance, cf. also [17]. In order to study only the effect due to the three-dimensional regulator functions and not from, e.g. the heat bath, we will focus on $T = 0$ and $\mu = 0$ in the following.

In Fig. E.1, the sigma spectral function is shown for different external spatial momenta. We note that, when plotted as a function of external energy, the threshold for the two-pion decay channel, cf. Eq. (8.2), is boosted to higher energies. From Lorentz invariance we would expect the shift in energy to be

$$\Delta\omega = \sqrt{\omega_0^2 + \vec{p}^2} - \omega_0, \quad (\text{E.1})$$

where ω_0 denotes the location of the peak or threshold at $\vec{p} = 0$. Using $\omega_0 \approx 270$ MeV, we find the expected boost to be $\Delta\omega \approx 480$ MeV for a momentum of $|\vec{p}| = 700$ MeV, which agrees with the shift observed in Fig. E.1.

However, although the extent of the Lorentz boost is found to be correct, the shape of the sigma spectral function does change slightly when increasing the spatial momentum, i.e. it develops a peak near the two-pion threshold. This effect has been found to be due to a (ω -independent) shift of the real part of the two-point function to higher values, causing its zero crossing to be shifted to smaller energies. This effect is also found for the

E. Lorentz invariance and parameter dependence of spectral functions

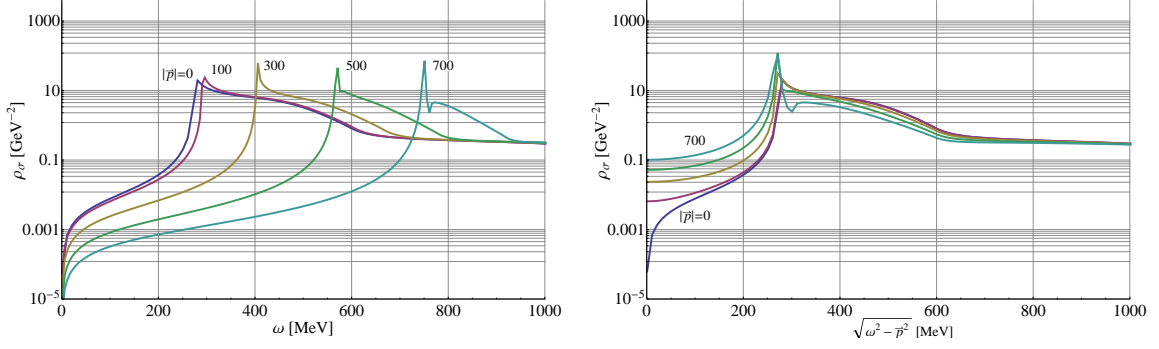


Figure E.1.: The sigma spectral function $\rho_\sigma(\omega, \vec{p})$ is shown as a function of external energy ω (left) and as a function of the invariant $\sqrt{\omega^2 - \vec{p}^2}$ (right) at $T = 0$ MeV and $\mu = 0$ MeV for different external momenta $|\vec{p}|$, as indicated by inset labels: 0 MeV (blue), 100 MeV (magenta), 300 MeV (ochre), 500 MeV (green), 700 MeV (turquoise). Taken from [68].

pion spectral function and can be corrected for by shifting the real part of the two-point function back to its original value by hand, in order to recover Lorentz invariance. This procedure has been used for the 3D plots of the momentum dependence of the spectral functions, see App. F, which serve as input for the calculation of the shear viscosity, cf. Ch. 5.

When plotting the sigma spectral function as a function of the invariant $\sqrt{\omega^2 - \vec{p}^2}$, as done on the right-hand side of Fig. E.1, one would expect, given Lorentz invariance, that all curves lie on top of each other. With increasing spatial momentum we do, however, observe some deviations from the curve corresponding to $\vec{p} = 0$. Apart from the already discussed formation of a peak, we observe that the spectral function exhibits larger values in the low-energy regime with increasing spatial momenta. This is due to the employed UV shape of the two-point functions, cf. Eqs. (6.7)-(6.8), which is clearly not Lorentz-invariant for $\epsilon > 0$, cf. also [17]. In fact, this effect is expected to disappear in the limit $\epsilon \rightarrow 0$, cf. App. E.2.

We conclude that the extent of the breaking of Lorentz symmetry induced by the use of three-dimensional regulator functions is small and that its effects are well understood, allowing for a robust study of the momentum dependence of spectral functions.

E.2 Dependence on the epsilon parameter

Now we turn to a discussion of the dependence of our results on the parameter ϵ , as introduced in the definition for the retarded two-point function, cf. Eq. (4.13), which is reproduced here for convenience,

$$\Gamma^{(2),R}(\omega, \vec{p}) = - \lim_{\epsilon \rightarrow 0} \Gamma^{(2),E}(p_0 = -i(\omega + i\epsilon), \vec{p}). \quad (\text{E.2})$$

E. Lorentz invariance and parameter dependence of spectral functions

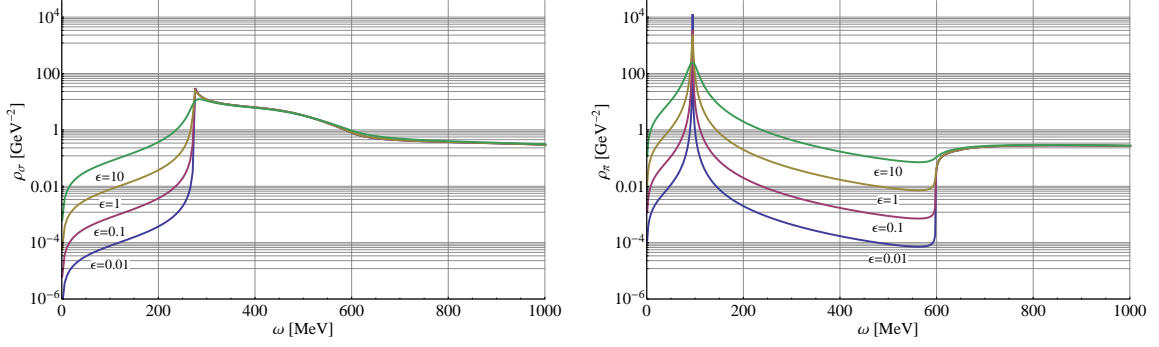


Figure E.2.: The sigma (left) and pion (right) spectral function, $\rho_\sigma(\omega, \vec{p})$ and $\rho_\pi(\omega, \vec{p})$, are shown versus external energy ω at $T = 0$ MeV and $\mu = 0$ MeV for different values of the parameter ϵ , as indicated by inset labels: 0.01 MeV (blue), 0.1 MeV (magenta), 1 MeV (ochre) and 10 MeV (green). Taken from [68].

We note that this section is also based on [68].

In principle, the retarded two-point functions are only obtained in the limit $\epsilon \rightarrow 0$, which is, however, not possible to perform exactly in our numerical calculation. Moreover, the imaginary part of the two-point functions vanishes for $\epsilon = 0$, cf. Eqs. (C.21)-(C.26) with $p_0 = -i\omega$, and therefore also the spectral functions will be zero, cf. Eq. (4.34). We do, however, find, that our results depend on a clear way on ϵ , as described in the following, and that our results are indeed meaningful, even for a finite value of ϵ .

The sigma and pion spectral function are shown in Fig. E.2 for vacuum conditions and different values of ϵ . We note that, at energies for which no decay channels are available, the value of the spectral functions in general decreases with smaller ϵ and is expected to vanish in the limit $\epsilon \rightarrow 0$. When the spectral function exhibits a peak that is to be associated with a stable particle, this peak is expected to turn into a Dirac delta function in the limit $\epsilon \rightarrow 0$. Such a behavior is indeed observed for the pion spectral function in Fig. E.2.

On the other hand, at energies that allow for quasi-particle processes to take place, cf. Eqs. (8.1)-(8.9), we observe that the spectral functions do not depend on ϵ , cf. Fig. E.2. Our results are therefore expected to reproduce the correct retarded result whenever there are quasi-particle processes available, while for energy regimes where there are no processes possible, the spectral functions will be either zero or reduce to a delta function in the limit $\epsilon \rightarrow 0$.

As described in Sec. 9.2, we utilize this finding by employing a larger value for ϵ to calculate the sigma spectral function near the critical endpoint at certain energies, in order to circumvent numerical problems that arise for smaller ϵ .

E.3 Dependence on the UV cutoff and normalization

In this section, we discuss the normalization of the obtained spectral functions and their dependence on the UV cutoff Λ . We begin by studying the cutoff dependence of the spectral functions, using the pion spectral function at $T = 0$, $\mu = 0$ and $\vec{p} = 0$ as a representative example, cf. Fig. E.3. Therein, we show the pion spectral function as obtained from the parameter given by Tab. 6.1, i.e. with a cutoff of $\Lambda = 1000$ MeV, and for a cutoff of $\Lambda = 800$ MeV, where we adjusted the UV parameters of the effective potential such as to reproduce the same IR values for the screening masses. We then find that the spectral function is almost independent of the UV cutoff, cf. Fig. E.3.

We now study whether our spectral functions are correctly normalized, as required by the sum rule given by Eq. (4.40), which can also be expressed as

$$\int_0^\infty d\omega^2 \rho(\omega^2) = 1. \quad (\text{E.3})$$

In order to evaluate this integral correctly in the case of the pion spectral function given by Fig. E.3, we have to perform the limit $\epsilon \rightarrow 0$, which will result in a Dirac delta peak at $\omega^2 = m_\pi^2$. We can then write the spectral function as

$$\rho(\omega^2) = Z^{-1} \text{sgn}(\omega) \delta(\omega^2 - m_\pi^2), \quad (\text{E.4})$$

where we neglect contributions from the decay channels at higher energies, see also [72]. The prefactor Z^{-1} can be determined by using the following Källén-Lehmann spectral representation for the retarded propagator, cf. also Eq. (4.22),

$$D^R(\omega^2) = - \int_0^\infty \frac{\rho(\omega'^2)}{\omega'^2 - (\omega + i\epsilon)^2} d\omega'^2, \quad (\text{E.5})$$

which gives

$$D^R(\omega^2) = \frac{Z^{-1}}{\omega^2 - m_\pi^2}, \quad (\text{E.6})$$

in the limit $\epsilon \rightarrow 0$. The retarded two-point function is then given by the inverse of this expression, i.e.

$$\Gamma^{(2),R}(\omega^2) = \frac{\omega^2 - m_\pi^2}{Z^{-1}}, \quad (\text{E.7})$$

which allows us to obtain Z from the derivative of the retarded two-point function with respect to ω^2 evaluated at $\omega^2 = m_\pi^2$, i.e.

$$Z = \left. \frac{\partial \Gamma^{(2),R}(\omega^2)}{\partial \omega^2} \right|_{\omega^2 = m_\pi^2}. \quad (\text{E.8})$$

In the case of the pion spectral function in the vacuum, cf. Fig. E.3, we obtain the

E. Lorentz invariance and parameter dependence of spectral functions

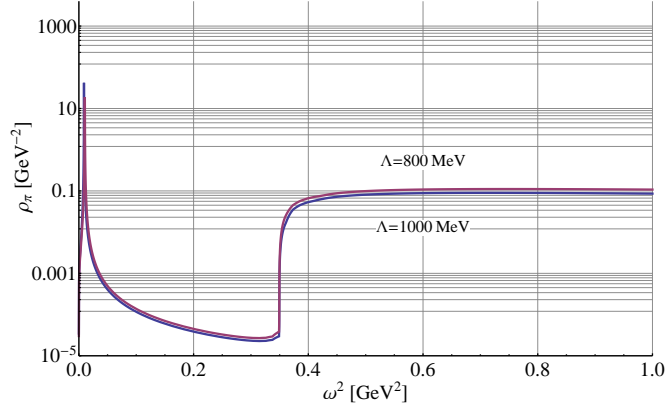


Figure E.3.: The pion spectral function ρ_π as obtained from two different UV cutoffs is shown vs. the square of the energy ω^2 in the vacuum and for vanishing external spatial momentum. The blue curve was obtained for $\Lambda = 1000$ MeV, while the magenta curve was obtained for $\Lambda = 800$ MeV. In both cases a value of $\epsilon = 0.01$ was used.

following values for the two different cutoffs

$$Z_{\Lambda=800}^{-1} = 0.55, \quad (\text{E.9})$$

$$Z_{\Lambda=1000}^{-1} = 0.48. \quad (\text{E.10})$$

We therefore note that the contribution of the pion peak to the total value of the integral given by Eq. (E.3) is smaller for the larger cutoff. This behaviour can be explained as follows. At the UV scale, we always have $Z = 1$, cf. Eq. (6.8), and all the spectral weight is concentrated in the delta peak and the sum rule, Eq. (E.5), is fulfilled. At lower scales, when fluctuations are taken into account, there will be some contribution from decay channels at higher energies, hence the contribution from the peak has to decrease.

In any case, the sum rule should always be fulfilled. However, we can not prove this exactly since we would have to integrate the spectral function up to infinitely large energies, cf. Eq. (E.5). When, for example, calculating the contribution from the decay channels up to $\omega = 1$ GeV for the two different cutoffs in Fig. E.3, we get

$$A_{\Lambda=0.8}(\omega^2 \in [0.35, 1]) = 0.065, \quad (\text{E.11})$$

$$A_{\Lambda=1}(\omega^2 \in [0.35, 1]) = 0.053. \quad (\text{E.12})$$

In order to estimate the contribution from higher energies, we use an extrapolation of the spectral function, see Fig. E.4. We note that the spectral function decreases with higher energies, approximately like $1/\omega^2$. When for example integrating up to $\omega^2 = 10$ GeV² we get for the standard cutoff $\Lambda = 1$ GeV

$$A_{\Lambda=1}(\omega^2 \in [0, 10]) = 0.33. \quad (\text{E.13})$$

E. Lorentz invariance and parameter dependence of spectral functions

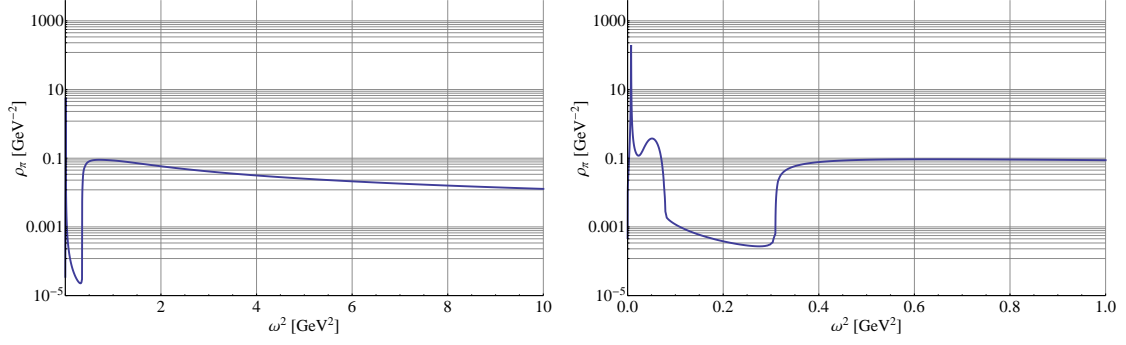


Figure E.4.: The pion spectral function ρ_π is shown vs. the square of the energy ω^2 at $T = 0$ (left) and at $T = 100$ MeV (right). On the left-hand side an extrapolation was used for the spectral function at $\omega^2 > 1$ GeV².

Together with the contribution from the delta peak, cf. Eq. (E.9), this is still not enough to satisfy the sum rule. Nevertheless, we expect that the spectral functions should be correctly normalized when all the contributions from higher energies could be taken into account correctly.

As a last example we study the normalization of the pion spectral function at $T = 100$ MeV, as shown on the right-hand side of Fig. E.4. In this case, the thermal process given by Eq. (8.5) leads to a pion peak with finite height and width. The integration of the spectral width is therefore straightforward and yields

$$A(\omega^2 \in [0, 0.023]) = 0.45, \quad (\text{E.14})$$

$$A(\omega^2 \in [0.023, 0.35]) = 0.014, \quad (\text{E.15})$$

$$A(\omega^2 \in [0.35, 1]) = 0.058, \quad (\text{E.16})$$

where we split the ω^2 integration into three parts, i.e. $A(\omega^2 \in [0, 0.023])$, which corresponds to the contribution from the pion peak, $A(\omega^2 \in [0.023, 0.35])$, which corresponds to the contribution from the thermal process $\pi^* + \pi \rightarrow \sigma$, cf. Eq. (8.5), and $A(\omega^2 \in [0.35, 1])$, which corresponds to the contribution from decay channels at higher energies up to $\omega^2 = 1$ GeV². We note that the spectral weight of the pion peak is slightly smaller than that of the delta peak at $T = 0$, cf. Eq. (E.9). This is compensated by the additional spectral weight from the thermal process $\pi^* + \pi \rightarrow \sigma$, and a slight increase in the spectral weight from processes in the range $\omega^2 \in [0.35, 1]$ GeV². Also at finite temperature, we expect the spectral functions to satisfy the sum rule, if all contributions up to arbitrarily large energies are taken into account.

F

3D plots of the momentum dependence of spectral functions

In the following, we summarize 3D plots of the momentum dependence of the sigma and the pion spectral function, $\rho_\sigma(\omega, \vec{p})$ and $\rho_\pi(\omega, \vec{p})$, at different temperatures and chemical potentials. The data represented by these plots has been used as a basis to calculate the shear viscosity, see also Ch. 10. As described in Sec. 6.3, the numerical calculation of spectral functions at finite external spatial momenta, $|\vec{p}| > 0$, is very time-consuming. Therefore, only certain $|\vec{p}|$ -slices of the 3D plots presented in the following were actually calculated, namely $|\vec{p}| = 0, 50, 100, 200, 400, 600, 800, 1000$ MeV, where 100 points were used in ω direction. Based on this information an interpolation was performed to obtain continuous 3D plots in the $(\omega, |\vec{p}|)$ -plane. Nevertheless, a single 3D plot still takes approximately 250000 CPU core hours to calculate, see Sec. 6.3 for details on our MPI parallelization and the high performance computers that were used to carry out these computations.

In Sec. F.1 we summarize 3D plots of the momentum dependence of the pion spectral function at finite temperatures and $\mu = 0$. Therein, we also provide for a comparison between the pion spectral function calculated with $\epsilon = 0.1$ MeV and with $\epsilon = 1$ MeV, cf. Fig. F.3. In Sec. F.2 we summarize 3D plots of the momentum dependence of the sigma spectral function at finite temperatures and $\mu = 0$. Finally, 3D plots for $\rho_\pi(\omega, \vec{p})$ and $\rho_\sigma(\omega, \vec{p})$ for different chemical potentials near the CEP are provided by Sec. F.3 and Sec. F.4, respectively.

F.1 3D plots of the pion spectral function at finite T

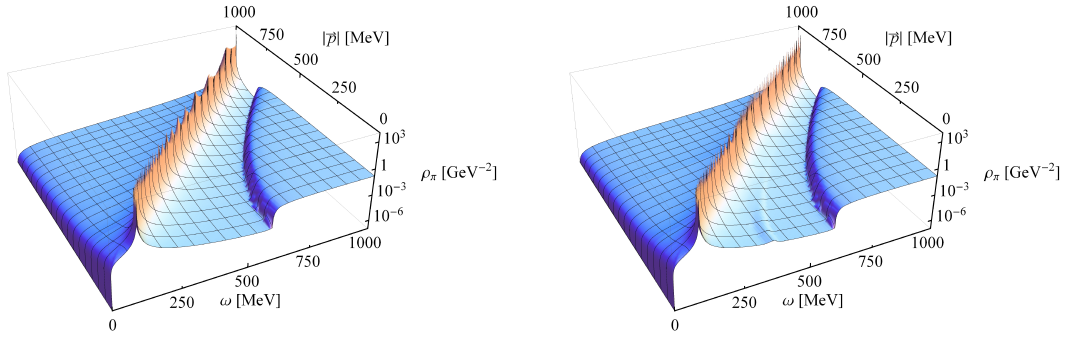


Figure F.1.: Pion spectral function at $T = 10$ MeV (left) and $T = 25$ MeV (right).

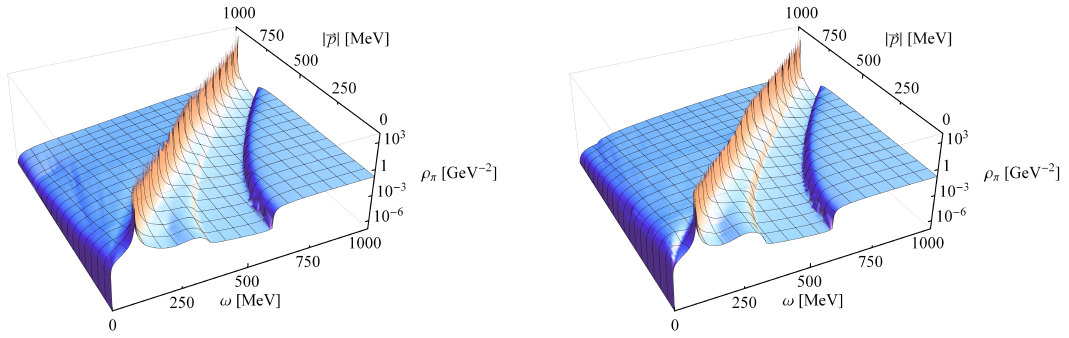


Figure F.2.: Pion spectral function at $T = 50$ MeV (left) and $T = 75$ MeV (right).

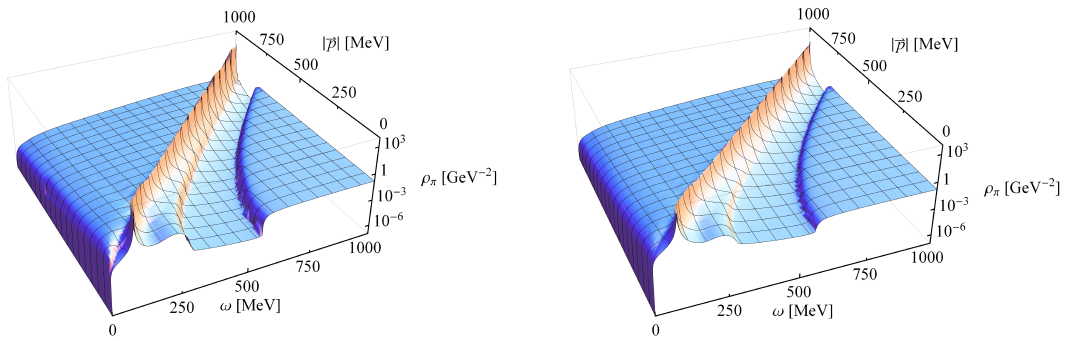


Figure F.3.: Pion spectral function at $T = 100$ MeV for $\epsilon = 0.1$ MeV (left) and $\epsilon = 1$ MeV (right).

F. 3D plots of the momentum dependence of spectral functions

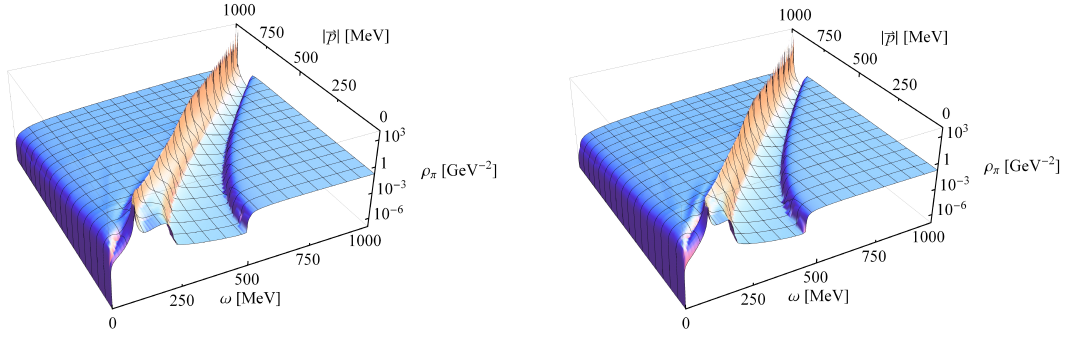


Figure F.4.: Pion spectral function at $T = 125$ MeV (left) and $T = 137.5$ MeV (right).

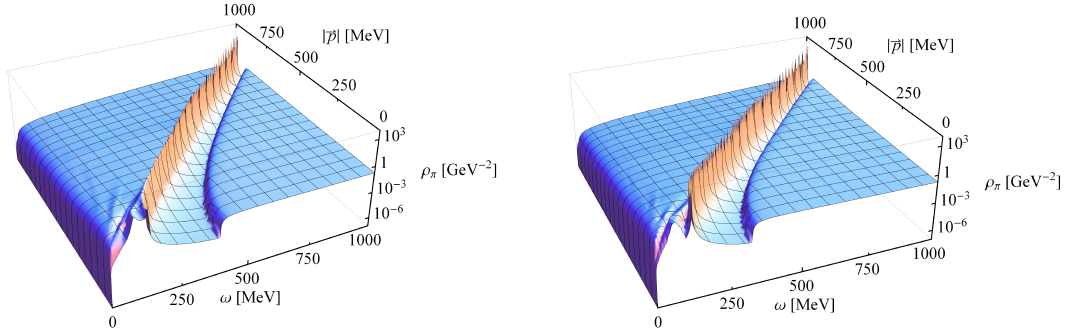


Figure F.5.: Pion spectral function at $T = 150$ MeV (left) and $T = 162.5$ MeV (right).

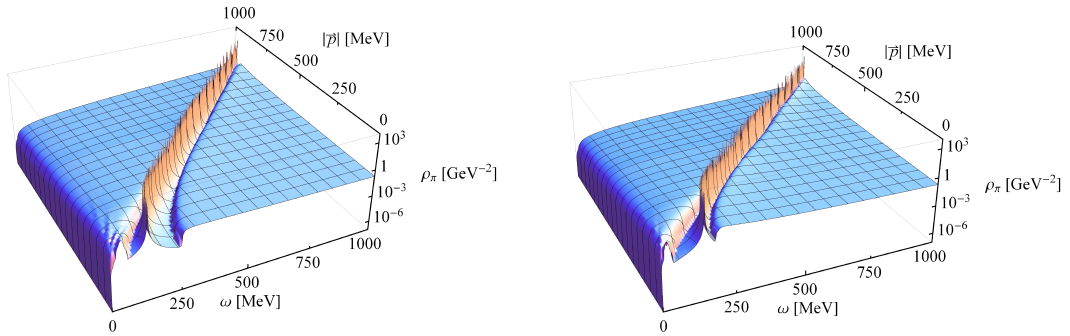


Figure F.6.: Pion spectral function at $T = 175$ MeV (left) and $T = 187.5$ MeV (right).

F. 3D plots of the momentum dependence of spectral functions

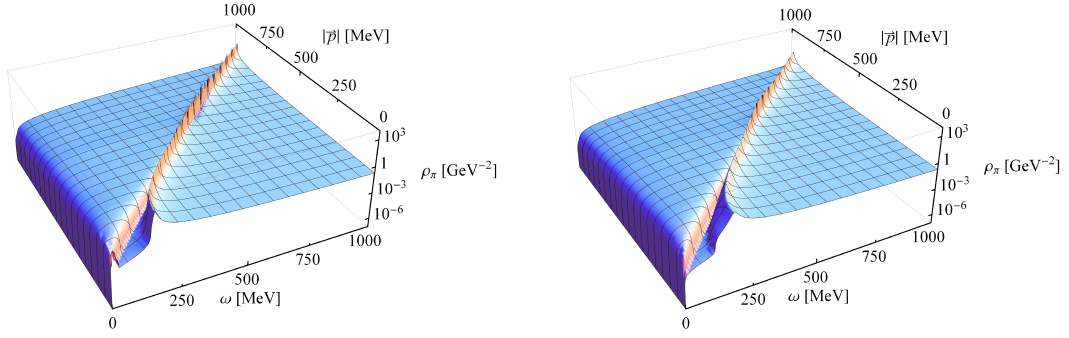


Figure F.7.: Pion spectral function at $T = 200$ MeV (left) and $T = 212.5$ MeV (right).

F.2 3D plots of the sigma spectral function at finite T

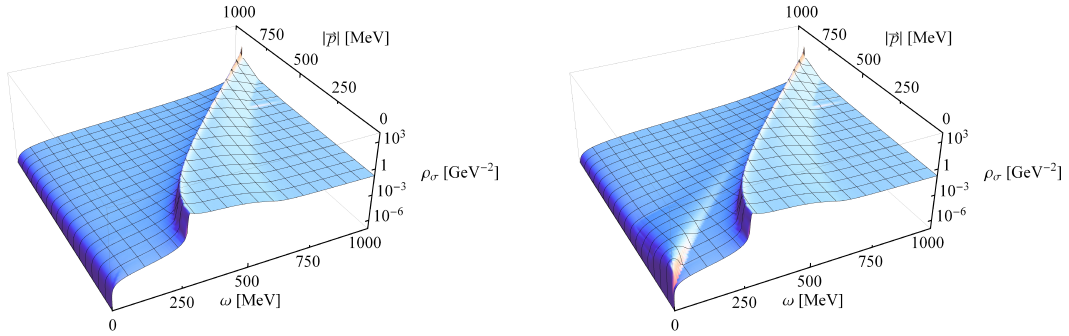


Figure F.8.: Sigma spectral function at $T = 10$ MeV (left) and $T = 25$ MeV (right).

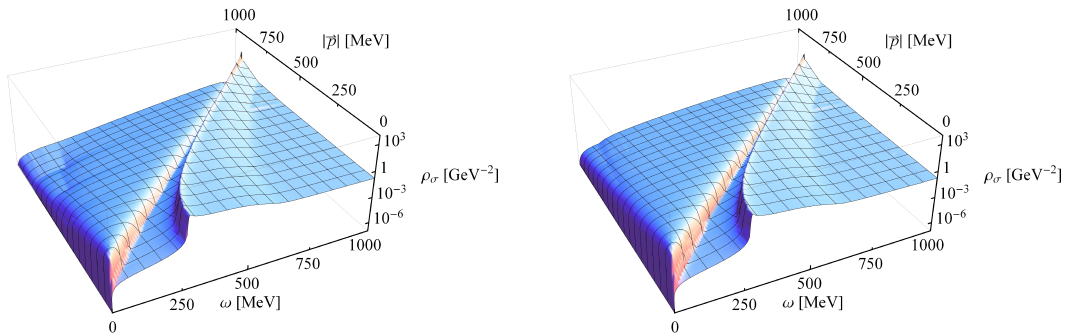


Figure F.9.: Sigma spectral function at $T = 50$ MeV (left) and $T = 75$ MeV (right).

F. 3D plots of the momentum dependence of spectral functions

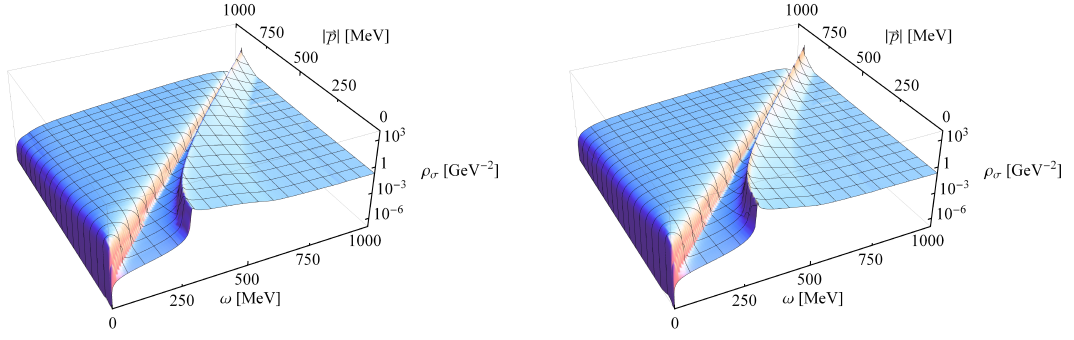


Figure F.10.: Sigma spectral function at $T = 100$ MeV (left) and $T = 125$ MeV (right).

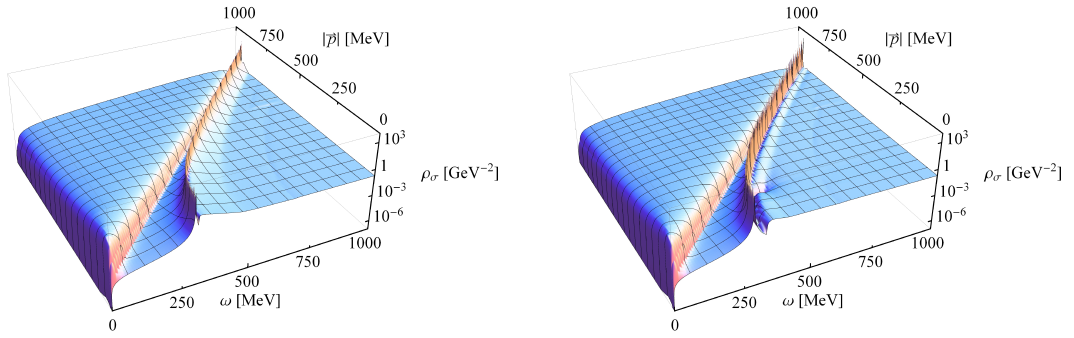


Figure F.11.: Sigma spectral function at $T = 137.5$ MeV (left) and $T = 150$ MeV (right).

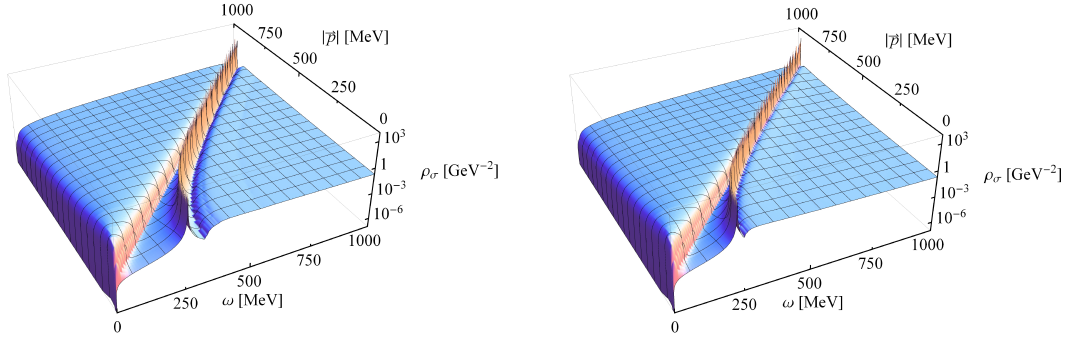


Figure F.12.: Sigma spectral function at $T = 162.5$ MeV (left) and $T = 175$ MeV (right).

F. 3D plots of the momentum dependence of spectral functions

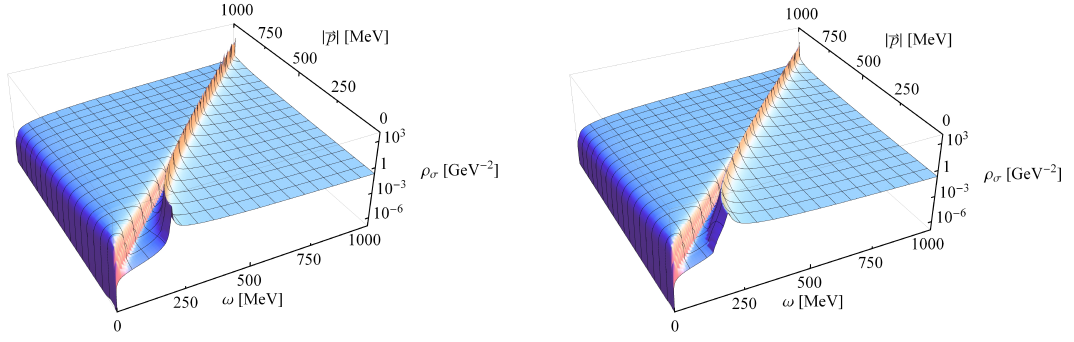


Figure F.13.: Sigma spectral function at $T = 187.5$ MeV (left) and $T = 200$ MeV (right).

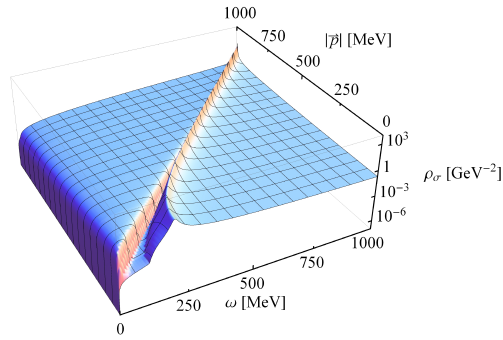


Figure F.14.: Sigma spectral function at $T = 212.5$ MeV.

F.3 3D plots of the pion spectral function near the CEP

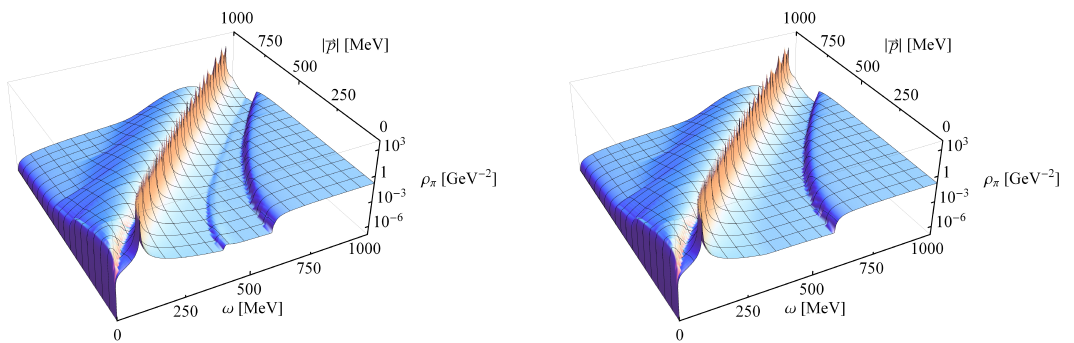


Figure F.15.: Pion spectral function at $\mu = 292$ MeV (left) and $\mu = 292.8$ MeV (right).

F. 3D plots of the momentum dependence of spectral functions

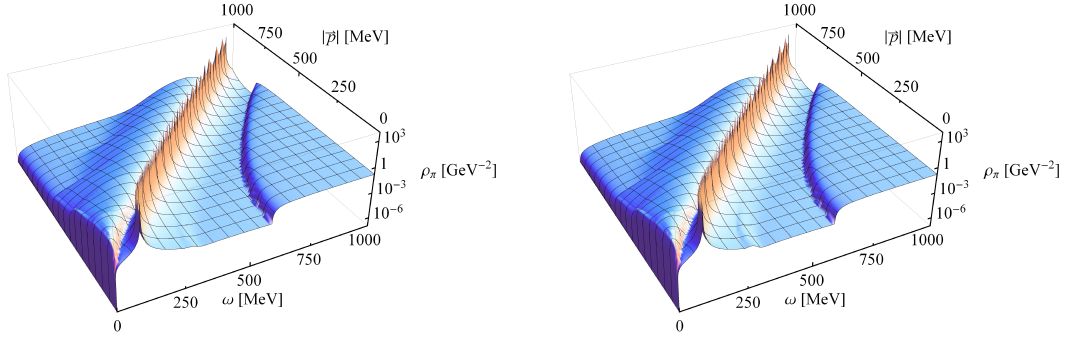


Figure F.16.: Pion spectral function at $\mu = 292.9$ MeV (left) and $\mu = 292.97$ MeV (right).

F.4 3D plots of the sigma spectral function near the CEP

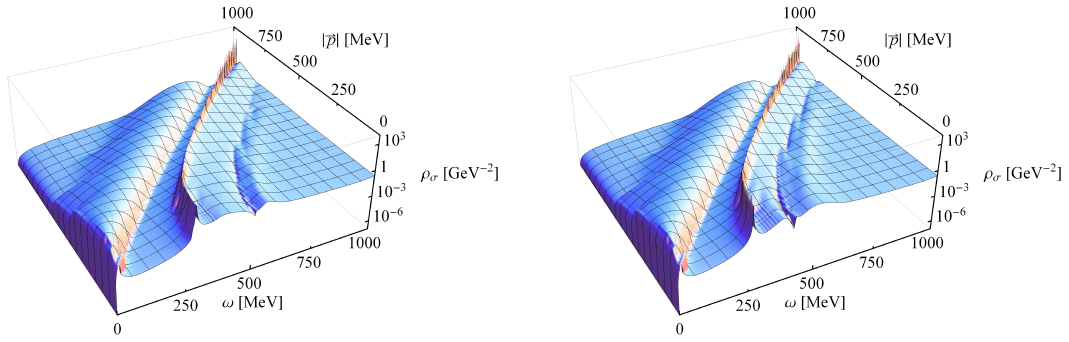


Figure F.17.: Sigma spectral function at $\mu = 292$ MeV (left) and $\mu = 292.4$ MeV (right).

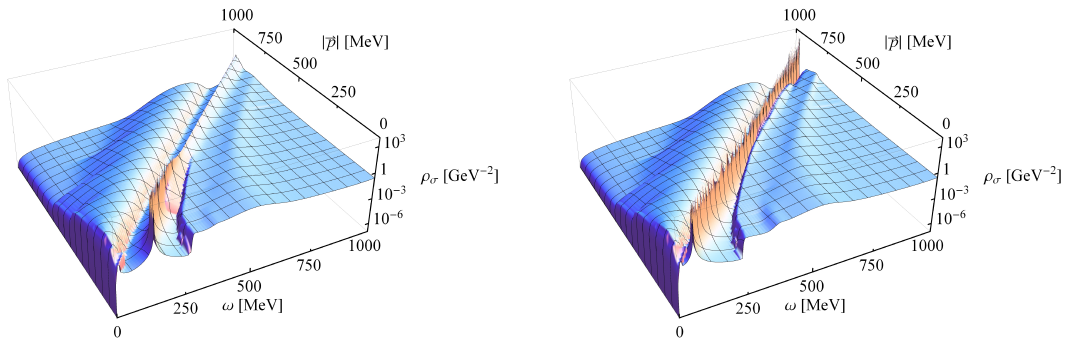


Figure F.18.: Sigma spectral function at $\mu = 292.8$ MeV (left) and $\mu = 292.9$ MeV (right).

F. 3D plots of the momentum dependence of spectral functions

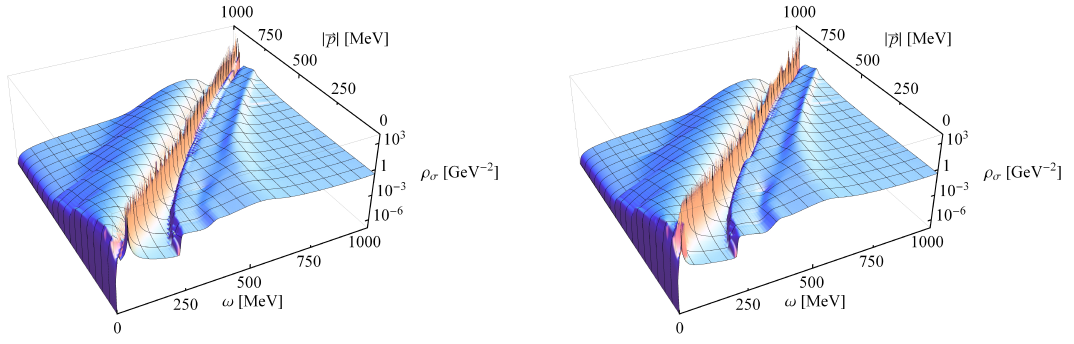


Figure F.19.: Sigma spectral function at $\mu = 292.95$ MeV (left) and $\mu = 292.97$ MeV (right).

Bibliography

- [1] Planck Collaboration, “Planck 2013 results,” *Astronomy & Astrophysics* **571** (2014) .
- [2] Y. Aoki, Z. Fodor, S. Katz, and K. Szabo, “The QCD transition temperature: Results with physical masses in the continuum limit,” *Phys.Lett.* **B643** (2006) 46–54, [arXiv:hep-lat/0609068](#) [hep-lat].
- [3] Y. Aoki, S. Borsanyi, S. Dür, Z. Fodor, S. D. Katz, *et al.*, “The QCD transition temperature: results with physical masses in the continuum limit II.,” *JHEP* **0906** (2009) 088, [arXiv:0903.4155](#) [hep-lat].
- [4] M. G. Alford, K. Rajagopal, and F. Wilczek, “Color flavor locking and chiral symmetry breaking in high density QCD,” *Nucl.Phys.* **B537** (1999) 443–458, [arXiv:hep-ph/9804403](#) [hep-ph].
- [5] GSI Helmholtzzentrum für Schwerionenforschung GmbH.
- [6] L. P. Csernai, J. Kapusta, and L. D. McLerran, “On the Strongly-Interacting Low-Viscosity Matter Created in Relativistic Nuclear Collisions,” *Phys.Rev.Lett.* **97** (2006) 152303, [arXiv:nucl-th/0604032](#) [nucl-th].
- [7] C. Gale, S. Jeon, B. Schenke, P. Tribedy, and R. Venugopalan, “Event-by-event anisotropic flow in heavy-ion collisions from combined Yang-Mills and viscous fluid dynamics,” *Phys.Rev.Lett.* **110** no. 1, (2013) 012302, [arXiv:1209.6330](#) [nucl-th].
- [8] P. Kovtun, D. Son, and A. Starinets, “Viscosity in strongly interacting quantum field theories from black hole physics,” *Phys.Rev.Lett.* **94** (2005) 111601, [arXiv:hep-th/0405231](#) [hep-th].
- [9] O. Philipsen, “Status of the QCD Phase Diagram from Lattice Calculations,” *Acta Phys.Polon.Supp.* **5** (2012) 825–835, [arXiv:1111.5370](#) [hep-ph].
- [10] G. Baym and N. D. Mermin, “Determination of thermodynamic Green’s functions,” *J. Math. Phys.* **2** (1961) 232.
- [11] N. Landsman and C. van Weert, “Real and Imaginary Time Field Theory at Finite Temperature and Density,” *Phys.Rept.* **145** (1987) 141.

Bibliography

- [12] M. Jarrell and J. Gubernatis, “Bayesian inference and the analytic continuation of imaginary-time quantum monte carlo data,” *Physics Reports* **269** no. 3, (1996) 133 – 195.
- [13] M. Asakawa, T. Hatsuda, and Y. Nakahara, “Maximum entropy analysis of the spectral functions in lattice QCD,” *Prog.Part.Nucl.Phys.* **46** (2001) 459–508, [arXiv:hep-lat/0011040](#) [[hep-lat](#)].
- [14] H. J. Vidberg and J. W. Serene, “Solving the Eliashberg equations by means of N-point Padé approximants,” *Journal of Low Temperature Physics* **29** (Nov., 1977) 179–192.
- [15] D. Dudal, O. Oliveira, and P. J. Silva, “Källén-Lehmann spectroscopy for (un)physical degrees of freedom,” [arXiv:1310.4069](#) [[hep-lat](#)].
- [16] K. Kamikado, N. Strodthoff, L. von Smekal, and J. Wambach, “Fluctuations in the quark-meson model for QCD with isospin chemical potential,” *Phys.Lett.* **B718** (2013) 1044–1053, [arXiv:1207.0400](#) [[hep-ph](#)].
- [17] K. Kamikado, N. Strodthoff, L. von Smekal, and J. Wambach, “Real-Time Correlation Functions in the O(N) Model from the Functional Renormalization Group,” *Eur.Phys.J.* **C74** (2014) 2806, [arXiv:1302.6199](#) [[hep-ph](#)].
- [18] S. Floerchinger, “Analytic Continuation of Functional Renormalization Group Equations,” *JHEP* **1205** (2012) 021, [arXiv:1112.4374](#) [[hep-th](#)].
- [19] J. Berges, N. Tetradis, and C. Wetterich, “Nonperturbative renormalization flow in quantum field theory and statistical physics,” *Phys.Rept.* **363** (2002) 223–386, [arXiv:hep-ph/0005122](#) [[hep-ph](#)].
- [20] J. M. Pawłowski, “Aspects of the functional renormalisation group,” *Annals Phys.* **322** (2007) 2831–2915, [arXiv:hep-th/0512261](#) [[hep-th](#)].
- [21] B.-J. Schaefer and J. Wambach, “Renormalization group approach towards the QCD phase diagram,” *Phys.Part.Nucl.* **39** (2008) 1025–1032, [arXiv:hep-ph/0611191](#) [[hep-ph](#)].
- [22] J. Braun, “Fermion interactions and universal behavior in strongly interacting theories,” *J.Phys.* **G39** (2012) 033001, [arXiv:1108.4449](#) [[hep-ph](#)].
- [23] B. Friman, C. Hohne, J. Knoll, S. Leupold, J. Randrup, *et al.*, “The CBM physics book: Compressed baryonic matter in laboratory experiments,” *Lect.Notes Phys.* **814** (2011) 1–980.
- [24] H. Gies, “Introduction to the functional RG and applications to gauge theories,” *Lect. Notes Phys.* **852** (2012) 287–348, [arXiv:hep-ph/0611146](#) [[hep-ph](#)].
- [25] D. Jungnickel and C. Wetterich, “Effective action for the chiral quark-meson model,” *Phys.Rev.* **D53** (1996) 5142–5175, [arXiv:hep-ph/9505267](#) [[hep-ph](#)].

Bibliography

- [26] B.-J. Schaefer and J. Wambach, “The phase diagram of the quark meson model,” *Nucl. Phys.* **A757** (2005) 479–492, [arXiv:nucl-th/0403039](#).
- [27] L. M. Haas, R. Stiele, J. Braun, J. M. Pawłowski, and J. Schaffner-Bielich, “Improved Polyakov-loop potential for effective models from functional calculations,” *Phys.Rev.* **D87** (2013) 076004, [arXiv:1302.1993 \[hep-ph\]](#).
- [28] T. K. Herbst, M. Mitter, J. M. Pawłowski, B.-J. Schaefer, and R. Stiele, “Thermodynamics of QCD at vanishing density,” [arXiv:1308.3621 \[hep-ph\]](#).
- [29] R.-A. Tripolt, N. Strodthoff, L. von Smekal, and J. Wambach, “Spectral Functions for the Quark-Meson Model Phase Diagram from the Functional Renormalization Group,” *Phys.Rev.* **D89** (2014) 034010, [arXiv:1311.0630 \[hep-ph\]](#).
- [30] M. Le Bellac, *Thermal Field Theory*. Cambridge University Press, 1996.
- [31] A. K. Das, *Finite temperature field theory*. World Scientific, 1997.
- [32] S. Strauss, C. S. Fischer, and C. Kellermann, “Analytic structure of the Landau gauge gluon propagator,” *Phys.Rev.Lett.* **109** (2012) 252001, [arXiv:1208.6239 \[hep-ph\]](#).
- [33] M. Haas, L. Fister, and J. M. Pawłowski, “Gluon spectral functions and transport coefficients in Yang–Mills theory,” [arXiv:1308.4960 \[hep-ph\]](#).
- [34] D. Nickel, “Extraction of Spectral Functions from Dyson-Schwinger Studies via the Maximum Entropy Method,” *Annals Phys.* **322** (2007) 1949–1960, [arXiv:hep-ph/0607224 \[hep-ph\]](#).
- [35] J. A. Mueller, C. S. Fischer, and D. Nickel, “Quark spectral properties above T_c from Dyson-Schwinger equations,” *Eur.Phys.J.* **C70** (2010) 1037–1049, [arXiv:1009.3762 \[hep-ph\]](#).
- [36] S.-x. Qin and D. H. Rischke, “Quark Spectral Function and Deconfinement at Nonzero Temperature,” *Phys.Rev.* **D88** (2013) 056007, [arXiv:1304.6547 \[nucl-th\]](#).
- [37] O. Greenberg, “Spin and Unitary Spin Independence in a Paraquark Model of Baryons and Mesons,” *Phys.Rev.Lett.* **13** (1964) 598–602.
- [38] G. Bali, K. Schilling, and C. Schlichter, “Observing long color flux tubes in SU(2) lattice gauge theory,” *Phys.Rev.* **D51** (1995) 5165–5198, [arXiv:hep-lat/9409005 \[hep-lat\]](#).
- [39] C. Gattringer and C. B. Lang, “Quantum chromodynamics on the lattice,” *Lect.Notes Phys.* **788** (2010) 1–343.
- [40] D. J. Gross and F. Wilczek, “Ultraviolet Behavior of Nonabelian Gauge Theories,” *Phys.Rev.Lett.* **30** (1973) 1343–1346.

Bibliography

- [41] D. Gross and F. Wilczek, “Asymptotically Free Gauge Theories. 2.,” *Phys.Rev.* **D9** (1974) 980–993.
- [42] H. D. Politzer, “Reliable Perturbative Results for Strong Interactions?,” *Phys.Rev.Lett.* **30** (1973) 1346–1349.
- [43] L. H. Ryder, *Quantum Field Theory*. Cambridge University Press, 2nd ed., 1996.
- [44] S. Weinberg, *The quantum theory of fields. Vol. 2: Modern applications*. Cambridge University Press, 1996.
- [45] **JLQCD and TWQCD** Collaboration, H. Fukaya *et al.*, “Determination of the chiral condensate from QCD Dirac spectrum on the lattice,” *Phys.Rev.* **D83** (2011) 074501, [arXiv:1012.4052 \[hep-lat\]](#).
- [46] M. Peskin and D. Schroeder, *An Introduction to Quantum Field Theory*. Westview Press, 1995.
- [47] V. Koch, “Aspects of chiral symmetry,” *Int.J.Mod.Phys.* **E6** (1997) 203–250, [arXiv:nucl-th/9706075 \[nucl-th\]](#).
- [48] M. Gell-Mann, R. Oakes, and B. Renner, “Behavior of current divergences under $SU(3) \times SU(3)$,” *Phys.Rev.* **175** (1968) 2195–2199.
- [49] R.-A. Tripolt, “The QCD phase diagram for finite volumes,” Master’s thesis, University of Graz, 2011.
- [50] Y. Nambu and G. Jona-Lasinio, “Dynamical Model of Elementary Particles based on an Analogy with Superconductivity. I.,” *Phys.Rev.* **122** (1961) 345–358.
- [51] Y. Nambu and G. Jona-Lasinio, “Dynamical Model of Elementary Particles based on an Analogy with Superconductivity. II.,” *Phys.Rev.* **124** (1961) 246–254.
- [52] C. Wetterich, “Exact evolution equation for the effective potential,” *Phys. Lett.* **B301** (1993) 90–94.
- [53] T. R. Morris, “The Exact renormalization group and approximate solutions,” *Int.J.Mod.Phys.* **A9** (1994) 2411–2450, [arXiv:hep-ph/9308265 \[hep-ph\]](#).
- [54] D. F. Litim, “Optimised renormalisation group flows,” *Phys. Rev.* **D64** (2001) 105007, [arXiv:hep-th/0103195](#).
- [55] J. Wambach, R.-A. Tripolt, N. Strodthoff, and L. von Smekal, “Spectral Functions from the Functional Renormalization Group,” [arXiv:1404.7312 \[hep-ph\]](#).
- [56] T. Appelquist and J. Carazzone, “Infrared Singularities and Massive Fields,” *Phys.Rev.* **D11** (1975) 2856.
- [57] D. F. Litim, “Derivative expansion and renormalization group flows,” *JHEP* **0111** (2001) 059, [arXiv:hep-th/0111159 \[hep-th\]](#).

Bibliography

- [58] J. Braun, “Thermodynamics of QCD low-energy models and the derivative expansion of the effective action,” *Phys. Rev.* **D81** (2010) 016008, [arXiv:0908.1543 \[hep-ph\]](#).
- [59] J. Zinn-Justin, “Quantum field theory and critical phenomena,” *Int.Ser.Monogr.Phys.* **113** (2002) 1–1054.
- [60] J. Braun and T. K. Herbst, “On the relation of the deconfinement and the chiral phase transition in gauge theories with fundamental and adjoint matter,” [arXiv:1205.0779 \[hep-ph\]](#).
- [61] J. M. Pawłowski and F. Rennecke, “Higher order quark-mesonic scattering processes and the phase structure of QCD,” *Phys.Rev.* **D90** (2014) 076002, [arXiv:1403.1179 \[hep-ph\]](#).
- [62] A. J. Helmboldt, J. M. Pawłowski, and N. Strodthoff, “Towards quantitative precision in the chiral crossover: masses and fluctuation scales,” [arXiv:1409.8414 \[hep-ph\]](#).
- [63] J. Braun, K. Schwenzer, and H.-J. Pirner, “Linking the quark meson model with QCD at high temperature,” *Phys. Rev.* **D70** (2004) 085016, [arXiv:hep-ph/0312277](#).
- [64] T. K. Herbst, J. M. Pawłowski, and B.-J. Schaefer, “The phase structure of the Polyakov–quark-meson model beyond mean field,” *Phys. Lett.* **B696** (2011) 58–67, [arXiv:1008.0081 \[hep-ph\]](#).
- [65] V. Skokov, B. Stokic, B. Friman, and K. Redlich, “Meson fluctuations and thermodynamics of the Polyakov loop extended quark-meson model,” *Phys.Rev.* **C82** (2010) 015206, [arXiv:1004.2665 \[hep-ph\]](#).
- [66] J.-P. Blaizot, R. Mendez-Galain, and N. Wschebor, “Non perturbative renormalisation group and momentum dependence of n-point functions (I),” *Phys.Rev.* **E74** (2006) 051116, [arXiv:hep-th/0512317 \[hep-th\]](#).
- [67] J.-P. Blaizot, R. Mendez-Galain, and N. Wschebor, “Non perturbative renormalization group and momentum dependence of n-point functions. II,” *Phys.Rev.* **E74** (2006) 051117, [arXiv:hep-th/0603163 \[hep-th\]](#).
- [68] R.-A. Tripolt, L. von Smekal, and J. Wambach, “Flow equations for spectral functions at finite external momenta,” *Phys.Rev.* **D90** no. 7, (2014) 074031, [arXiv:1408.3512 \[hep-ph\]](#).
- [69] N. Strodthoff, B.-J. Schaefer, and L. von Smekal, “Quark-meson-diquark model for two-color QCD,” *Phys.Rev.* **D85** (2012) 074007, [arXiv:1112.5401 \[hep-ph\]](#).
- [70] H.-T. Ding, A. Francis, O. Kaczmarek, F. Karsch, H. Satz, *et al.*, “Charmonium properties in hot quenched lattice QCD,” *Phys.Rev.* **D86** (2012) 014509, [arXiv:1204.4945 \[hep-lat\]](#).

Bibliography

- [71] J. Kapusta and C. Gale, *Finite-Temperature Field Theory: Principles and Applications*. Cambridge Monographs on Mathematical Physics. Cambridge University Press, 2006.
- [72] R. Alkofer and L. von Smekal, “The Infrared behavior of QCD Green’s functions: Confinement dynamical symmetry breaking, and hadrons as relativistic bound states,” *Phys.Rept.* **353** (2001) 281, [arXiv:hep-ph/0007355](#) [[hep-ph](#)].
- [73] J. A. Müller, *Dyson-Schwinger Approach to Finite Temperature QCD*. PhD thesis, TU Darmstadt, 2010.
- [74] S. R. de Groot, W. A. van Leeuwen and Ch. G. van Weert, *Relativistic kinetic theory*. North-Holland, 1980.
- [75] L. D. Landau and E. Lifshitz, *Fluid Mechanics, Second Edition: Volume 6 (Course of Theoretical Physics)*. Butterworth-Heinemann, 1987.
- [76] J.-Y. Ollitrault, “Relativistic hydrodynamics for heavy-ion collisions,” *Eur.J.Phys.* **29** (2008) 275–302, [arXiv:0708.2433](#) [[nucl-th](#)].
- [77] P. Romatschke, “New Developments in Relativistic Viscous Hydrodynamics,” *Int.J.Mod.Phys.* **E19** (2010) 1–53, [arXiv:0902.3663](#) [[hep-ph](#)].
- [78] K. Heckmann, *Transport coefficients of strongly interacting matter*. PhD thesis, TU Darmstadt, 2011.
- [79] D. Fernandez-Fraile and A. Gomez Nicola, “Transport coefficients and resonances for a meson gas in Chiral Perturbation Theory,” *Eur.Phys.J.* **C62** (2009) 37–54, [arXiv:0902.4829](#) [[hep-ph](#)].
- [80] M. S. Green, “Markoff random processes and the statistical mechanics of time-dependent phenomena. II. Irreversible processes in fluids,” *Journal of Chemical Physics* **22** (1954) 398–413.
- [81] R. Kubo, “Statistical-Mechanical Theory of Irreversible Processes. I. General Theory and Simple Applications to Magnetic and Conduction Problems,” *Journal of the Physical Society of Japan* **12** (1957) 570–586.
- [82] R. Lang, N. Kaiser, and W. Weise, “Shear Viscosity of a Hot Pion Gas,” *Eur.Phys.J.* **A48** (2012) 109, [arXiv:1205.6648](#) [[hep-ph](#)].
- [83] L. von Smekal, P. Amundsen, and R. Alkofer, “A Covariant model for dynamical chiral symmetry breaking in QCD,” *Nucl.Phys.* **A529** (1991) 633–652.
- [84] B.-J. Schaefer and J. Wambach, “Susceptibilities near the QCD (tri)critical point,” *Phys. Rev.* **D75** (2007) 085015, [arXiv:hep-ph/0603256](#).
- [85] R.-A. Tripolt, J. Braun, B. Klein, and B.-J. Schaefer, “The Effect of Fluctuations on the QCD Critical Point in a Finite Volume,” [arXiv:1308.0164](#) [[hep-ph](#)].

Bibliography

- [86] N. Strodthoff and L. von Smekal, “Polyakov-Quark-Meson-Diquark Model for two-color QCD,” [arXiv:1306.2897 \[hep-ph\]](#).
- [87] T. D. Cohen, “Functional integrals for QCD at nonzero chemical potential and zero density,” *Phys.Rev.Lett.* **91** (2003) 222001, [arXiv:hep-ph/0307089 \[hep-ph\]](#).
- [88] E. E. Svanes and J. O. Andersen, “Functional renormalization group at finite density and Bose condensation,” *Nucl.Phys.* **A857** (2011) 16–28, [arXiv:1009.0430 \[hep-ph\]](#).
- [89] A. Dobado and F. J. Llanes-Estrada, “The Viscosity of meson matter,” *Phys.Rev.* **D69** (2004) 116004, [arXiv:hep-ph/0309324 \[hep-ph\]](#).
- [90] P. B. Arnold, G. D. Moore, and L. G. Yaffe, “Transport coefficients in high temperature gauge theories. 2. Beyond leading log,” *JHEP* **0305** (2003) 051, [arXiv:hep-ph/0302165 \[hep-ph\]](#).
- [91] J. M. Maldacena, “The Large N limit of superconformal field theories and supergravity,” *Int.J.Theor.Phys.* **38** (1999) 1113–1133, [arXiv:hep-th/9711200 \[hep-th\]](#).
- [92] T. D. Cohen, “Is there a ‘most perfect fluid’ consistent with quantum field theory?,” *Phys.Rev.Lett.* **99** (2007) 021602, [arXiv:hep-th/0702136 \[HEP-TH\]](#).
- [93] A. Rebhan and D. Steineder, “Violation of the Holographic Viscosity Bound in a Strongly Coupled Anisotropic Plasma,” *Phys.Rev.Lett.* **108** (2012) 021601, [arXiv:1110.6825 \[hep-th\]](#).
- [94] M. Brigante, H. Liu, R. C. Myers, S. Shenker, and S. Yaida, “The Viscosity Bound and Causality Violation,” *Phys.Rev.Lett.* **100** (2008) 191601, [arXiv:0802.3318 \[hep-th\]](#).
- [95] A. Adams, L. D. Carr, T. Schäfer, P. Steinberg, and J. E. Thomas, “Strongly Correlated Quantum Fluids: Ultracold Quantum Gases, Quantum Chromodynamic Plasmas, and Holographic Duality,” *New J.Phys.* **14** (2012) 115009, [arXiv:1205.5180 \[hep-th\]](#).
- [96] L. C. C. Agosta, S. Wang and H. Meyer *J. Low Temp. Phys.* **67** (1987) 237.
- [97] M. Mitter, “Comparison of renormalization group flows,” Master’s thesis, University of Graz, 2009.
- [98] U. Ellwanger and C. Wetterich, “Evolution equations for the quark - meson transition,” *Nucl.Phys.* **B423** (1994) 137–170, [arXiv:hep-ph/9402221 \[hep-ph\]](#).
- [99] D. N. Zubarev, *Nonequilibrium statistical thermodynamics*. Consultants Bureau, 1974.

Bibliography

- [100] E. A. Calzetta, *Nonequilibrium Quantum Field Theory*. Cambridge University Press, 2008.
- [101] C. Wesp, A. El, F. Reining, Z. Xu, I. Bouras, *et al.*, “Calculation of shear viscosity using Green-Kubo relations within a parton cascade,” *Phys.Rev.* **C84** (2011) 054911, [arXiv:1106.4306](#) [hep-ph].

Acknowledgements

First of all, I would like to thank my supervisor, Lorenz von Smekal, for allowing me to work on this interesting, challenging and rewarding topic. Throughout the last three and a half years I could always rely on his guidance, patience and enthusiasm when it comes to the investigation of physical problems. Without the many physical insights he shared with me in the course of countless discussions this thesis would not have been possible.

I would also like to thank my co-supervisor, Jochen Wambach, whose experience and broad knowledge was invaluable to steer this PhD project into the right direction. He always kept an eye on the larger perspective and was the first point of contact when it came to the phenomenological interpretation of my results.

As for the structured PhD education I benefited from during the last three years within the H-QM 4 group, I would like to thank the whole HGS-HIRe and H-QM team, in particular Henner Büsching and Sascha Vogel, for organizing all the lecture weeks and soft skill seminars.

Moreover, I would like to thank Jens Braun, Michael Buballa, Dirk Rischke, Jan Pawłowski and Bernd-Jochen Schaefer for many interesting and useful discussions.

Additionally, I would like to thank my present and former colleagues, in particular Markus Huber, Christian Wesp, Tina Herbst and Mario Mitter for many physics and non-physics related discussions. My special thanks in this context go to Nils Strodthoff for the fruitful collaboration and his work on spectral functions, which served as a starting point for this thesis.

Insbesondere möchte ich auch meiner Mutter danken, die mich immer auf meinem Lebensweg unterstützt, egal welche Wendungen dieser nimmt oder wie weit er wegführt.

Till sist vill jag tacka min vän, Christian, för att bringa så mycket glädje till mitt liv.

Curriculum vitae

Name: Ralf-Arno Tripolt
Date of birth: 12/06/1987
Place of birth: Graz
Marital status: single

Education and degrees:

1997-2005 Bundesrealgymnasium Carneri, Graz
2005-2006 Undergraduate studies in physics and mathematics at the university of Graz
2006-2007 Community service in lieu of military service
2007-2009 Undergraduate studies in theoretical physics at the university of Graz
03-09/2009 Erasmus exchange student at HU Berlin
2009-2010 Undergraduate studies in physics at the university of Graz
08-09/2010 Summer student at the GSI Helmholtzzentrum for heavy ion research, Darmstadt
2010-2011 Undergraduate studies in theoretical physics at the university of Graz, diploma thesis on “The QCD phase diagram for finite volumes”
2011-2015 Postgraduate studies in theoretical physics at TU Darmstadt

Erklärung

gemäß §9 Abs. 1 der Promotionsordnung.

Ich erkläre hiermit, dass ich diese Arbeit abgesehen von den in ihr ausdrücklich genannten Hilfen und Quellen selbständig verfasst habe. Des Weiteren versichere ich, dass ich bisher noch keinen Promotionsversuch unternommen habe.

Darmstadt, den 9.4.2015

Ralf-Arno Tripolt